



UNIVERSITY OF NAIROBI

**EFFECTS OF TiO_2 COMPACT LAYER ON PHOTOVOLTAIC
CHARACTERISTICS OF $\text{TiO}_2/\text{Nb}_2\text{O}_5$ DYE SENSITIZED SOLAR CELLS**

BY

OWUOR BRIAN OWINO

I56/88808/2016

**A Thesis Submitted in Fulfillment of the Requirements for the Award of the Degree of
Master of Science (MSc) in Physics of University of Nairobi**

2019

DECLARATION

Declaration by the candidate

I declare that this thesis is my original work and has not been submitted elsewhere for examination, award of a degree or publication. Where other people's work or my own work has been used, this has properly been acknowledged and referenced in accordance with the University of Nairobi's policy requirements.

Owuor Brian Owino

I56/88808/2016

Department of Physics

University of Nairobi

Signature



Date:

19/09/2019

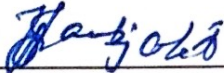
Declaration by supervisors

The following thesis: *“Effects of TiO₂ Compact Layer on Photovoltaic Characteristics of TiO₂/Nb₂O₅ Dye Sensitized Solar Cells”*, has been submitted with our consent as the University supervisors.

Prof. Francis Wanjala Nyongesa

Department of Physics

University of Nairobi

Signature  Date: 19/9/2019

Dr. Alex Awuor Ogacho

Department of Physics

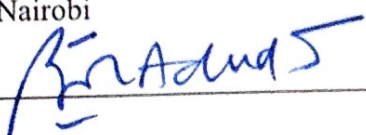
University of Nairobi

Signature  Date: 19/09/2019

Prof. Bernard O. Aduda

Department of Physics

University of Nairobi

Signature  Date: 19/09/2019

DEDICATION

This work is dedicated to my respected parents.

ACKNOWLEDGEMENT

I would like to express my heartiest gratitude and sincere appreciation to my advisors; Prof. Francis W. Nyongesa, Prof. Bernard O. Aduda and Dr. Alex A. Ogacho for their diligent effort and commitment in guiding me through this research work. I could have not made it without their good faith in my efforts, honest criticism and guidance. I am grateful to Mr. Victor Odari for his valuable suggestions and assistance during the research. I am greatly indebted to the University of Nairobi for the provision of scholarship that enabled me complete this research and to International Science Program (ISP) for the financial support they gave me. Finally, I would like to thank my family: my parents and my siblings for supporting me spiritually throughout the pursuit of my M.Sc. I am thankful to my friends who supported me as well.

ABSTRACT

Titanium dioxide has been widely used in dye sensitized solar cells as a semiconductor, however, the recombination rate of photo generated hole-electron pairs on TiO_2 is very high which reduces its electron transport efficiency. On the other hand, Niobium pentoxide is an n-type transition metal oxide semiconductor with good chemical stability and a conduction band potential that is 0.2 – 0.4 eV higher than that of TiO_2 . This potential difference can form an energy barrier at the electrode-electrolyte interface thereby reducing the rate of recombination of photo-injected electrons. Composite metal oxide semiconductor electrodes possess promising properties could enhance the conversion efficiency of dye sensitized solar cells. However, charge recombination at the interfaces still affects the performance of solar cells fabricated from composites. In this work we introduce TiO_2 blocking layer on $\text{TiO}_2/\text{Nb}_2\text{O}_5$ composite photoelectrode to assess its potential application in dye sensitized solar cells. TiO_2 compact layers were deposited on FTO glass substrate by spray pyrolysis technique which was subsequently followed by deposition of nanoporous $\text{TiO}_2/\text{Nb}_2\text{O}_5$ composite layer by screen printing technique. The structural properties of the deposited films were studied by Raman spectroscopy and X-ray diffraction. Optical properties of the films were evaluated using *UV-VIS* spectrophotometer in wavelength range of 300-1100 nm. SCOUT software was used to determine thickness and to retrieve the optical constants; refractive index n_f and extinction coefficient k_λ of TiO_2 compact layer. This was done based on the interactive curve fitting using O'Leary-Johnson-Lim (OJL) interband-transition dielectric model together with Drude model. The photovoltaic parameters of the prepared dye sensitized solar cells were evaluated using current density-voltage (*J-V*) characterization from which, the best conversion efficiency was attained with 60 nm thick TiO_2 compact layer with current density J_{sc} equal to 8.16 mAcm^{-2} , open circuit voltage V_{oc} of 0.79 V, fill factor *FF* of 0.578 and efficiency η of 3.39 %. Further, interfacial charge transfer in the cell was studied using electrochemical impedance spectroscopy. Nyquist plots of the device were measured at a DC bias of 0.6 V. For the best performing cell, recombination resistance R_{rec} was 899.36 Ohm.cm^2 , chemical capacitance $C_\mu=4.3\times 10^{-5} \text{ Fcm}^{-2}$, transport resistance R_{tr} $4.53\times 10^2 \text{ Ohm.cm}^2$, geometrical capacitance $C_g=8.82\times 10^{-6} \text{ Fcm}^{-2}$ and recombination resistance $R_s = 10 \text{ Ohm.cm}^2$. Charge carrier life time of the solar cells were also determined with the best performing solar cell having charge carrier lifetime of $3.86\times 10^{-2} \text{ s}$ while charge carrier lifetime for solar cell showing lowest efficiency to be $2.50\times 10^{-4} \text{ s}$.

Table of Contents

DECLARATION	ii
DEDICATION	iv
ACKNOWLEDGEMENT	v
ABSTRACT	vi
LIST OF TABLES	xi
LIST OF FIGURES	xii
LIST OF SYMBOLS	xiv
LIST OF ABBREVIATIONS	xvi
CHAPTER ONE: INTRODUCTION	1
1.1 Background of the Study	1
1.2 Photovoltaics (PV).....	2
1.2.1 Principles of photovoltaic conversion.....	2
1.2.2 Classification of photovoltaic solar cells	3
1.3 Statement of the Problem.....	8
1.4 Aim of Study.....	8
1.4.1 General objective	8
1.4.2 Specific objectives	9
1.5 Justification and Significance of study	9
CHAPTER TWO: LITERATURE REVIEW	11
2.1 Introduction.....	11
2.2 History of Dye Sensitized Solar Cells	11
2.2.1 Transparent conducting electrode	12
2.2.2 Dye sensitizers	13
2.2.3 Redox electrolyte	14
2.2.4 Counter electrode.....	15

2.2.5	Metal oxide semiconductors	15
2.2.6	Compact layer	18
CHAPTER THREE : THEORETICAL FRAMEWORK		21
3.1	Introduction.....	21
3.2	Optical Properties and Band gap Evaluation	21
3.2.1	Drude model.....	23
3.2.2	O’Leary-Johnson-Lim (OJL) model.....	24
3.3	Dye Sensitized Solar Cell Operation Principle.....	26
3.3.1	Short circuit photocurrent (I_{sc}).....	29
3.3.2	Open circuit potential (V_{oc}).....	29
3.3.3	Series and shunt resistance.....	30
3.3.4	Fill factor (FF).....	31
3.3.5	Power conversion efficiency (η).....	32
3.4	Electrochemical impedance spectroscopy (EIS).....	33
CHAPTER FOUR: MATERIALS AND METHODS		38
4.1	Introduction.....	38
4.2	Fabrication of the Photoanode	38
4.2.1	Spray pyrolysis.....	39
4.2.2	Compact layers with varying thickness deposited by spray pyrolysis.....	40
4.3	Preparation of Porous TiO_2/Nb_2O_5 Composite Thin Films by Screen Printing Technique	40
4.4	Thin Film Characterization	41
4.5	TiO_2/Nb_2O_5 Elemental Analysis using EDXRF Spectrometer	42
4.6	Raman Spectroscopy.....	43

4.7	Electrical Characterization.....	44
4.8	Morphological and Structural Characterization.....	46
4.9	Preparation of the Electrodes, Counter Electrodes and DSSC Assembly	46
4.9.1	Counter Electrode	47
4.9.2	Solar Cell Assembly	47
4.10	Current-Voltage (<i>I-V</i>) Characterization of the Solar Cell.....	48
4.11	Electrochemical Impedance Spectroscopy (EIS).....	48
CHAPTER FIVE: RESULTS AND DISCUSSIONS		50
5.1	Introduction.....	50
5.2	Structural Characterization of TiO ₂ Compact Layer and TiO ₂ /Nb ₂ O ₅ Composite Layer	50
5.2.1	Analysis of Raman spectra.....	50
5.3	Energy Dispersive X-ray Fluorescence of TiO ₂ /Nb ₂ O ₅ Composite Thin Films.....	55
5.4	Optical Characterization	56
5.4.1	Effects of annealing and film thickness on optical properties of TiO ₂ compact layer	57
5.5	SCOUT Modeling.....	59
5.5.1	Effects of annealing on band gap energy of TiO ₂ compact layer	60
5.5.2	Effect of film thickness on band gap energy E_g of TiO ₂ compact layer	62
5.5.3	Effects of annealing on Refractive index of TiO ₂ compact layer	63
5.6	Refractive Index n_f and Porosity P	64
5.6.1	Effects of annealing on extinction coefficient (k_λ) of TiO ₂ compact layer	65
5.6.2	Effects of film thickness on extinction coefficient k_λ of TiO ₂ compact layer.....	66
5.7	Electrical Characterization of TiO ₂ Compact Layer.....	66
5.7.1	Influence of annealing on electrical properties of TiO ₂ compact layer	66

5.7.2	Effect of film thickness on electrical properties of TiO ₂ compact layer.....	67
5.8	Optical Characterization of TiO ₂ /Nb ₂ O ₅ Composite Thin Films.....	68
5.9	Current-voltage (I-V) Characteristics	71
5.10	Electrochemical impedance spectroscopy	75
CHAPTER SIX : CONCLUSION AND RECOMMENDATIONS		81
6.1	Conclusion	81
6.2	Recommendations.....	82
References		83

LIST OF TABLES

Table 5. 1: Occurrence of TiO ₂ and Nb ₂ O ₅ in parts per million for different ratios	55
Table 5. 2: TiO ₂ compact layers deposited with varying parameters. Annealing was done at 500 °C for one hour.....	57
Table 5. 3: Influence of annealing on electrical properties of TiO ₂ compact layer.	67
Table 5. 4: Influence of film thickness on electrical properties of TiO ₂ compact layer	68
Table 5. 5: I-V characteristics for DSSC with compact layers of varying thickness.....	74
Table 5. 6: Values of recombination resistance R _{tr} , chemical capacitance C _μ , transport resistance R _{tr} , geometrical capacitance C _g , series resistance R _s and electron lifetime τ obtained from the fabricated solar cells.	78

LIST OF FIGURES

Figure 1.1: Solar radiation spectrum for direct sunlight at both the top of the earth’s atmosphere (yellow part) and at the sea level (red region)	2
Figure 1.2: Typical representation of photovoltaic effect. Electrons in the valence band (VB) get excited to conduction band (CB) of a semiconductor upon absorption of energy $h\nu$ from the sun creating holes h^+ in the valence band.....	3
Figure 1.3: Generations of Photovoltaics	4
Figure 1.4: Photovoltaic research cell record efficiency chart	6
Figure 2.1: Crystal structures for anatase, rutile and brookite phase of TiO_2	17
Figure 2.2: Dye sensitized solar cell (i) without compact layer and (ii) Unidirectional electron transfer through the blocking layer. The three pathways for back reaction of electrons in a DSSC: (a) With the oxidized dye, (b) With the electrolyte via the TiO_2 , (c) With the electrolyte via FTO substrate	19
Figure 3.1: Illustration of electron kinetics in dye sensitized solar cells	27
Figure 3.2: One- diode equivalent circuit diagram for dye sensitized solar cells.....	29
Figure 3.3: Effect of the series resistance shunt resistance R_{SH} on current-voltage characteristics.	31
Figure 3.4: I-V characteristic curve of dye sensitized solar cells.	32
Figure 3.5: Typical representation of impedance	34
Figure 3.6: Simplified transmission line equivalent circuit for a complete dye sensitized solar cell.....	36
Figure 4.1: Schematic diagram for spray pyrolysis technique.....	

Figure 4.2: Schematic diagram for deposition of TiO₂/Nb₂O₅ composite thin film by screen printing technique 41

Figure 4.3: Schematic diagram of energy dispersive x-ray fluorescence set up..... 43

Figure 4.4: Illustration of four-point probe. The inner probes for measuring voltage and the outer probes measuring current. 44

Figure 4.5: Complete assembly of dye sensitized solar cell 47

Figure 4.6: Electrochemical impedance spectroscopy measurement set up 48

LIST OF SYMBOLS

α	Absorption coefficient
λ	Wavelength
γ_V, γ_C	Damping constants of the valence and conduction bands respectively
μ	Mobility
ω	Frequency
ω_p	Plasma frequency
η	Conversion efficiency
ϵ_i	Dielectric function
ϵ_o	Permittivity of free space
ϵ_r	Relative dielectric constant
ϵ_χ	Static dielectric constant
ξ	Normalized dipole matrix element
σ	Defect density
χ	Ideality factor
ϕ	Phase shift
ρ_A	Density of material
Ω_τ	Damping constant
c_o	Speed of light
e	Charge
I, I_d, I_{\max}	External load current, current lost due to recombination, Maximum current,
I_{ph}, I_{ph}, I_{sh}	Photogenerated current, and Current through shunt resistor respectively.
I_o	Incident light intensity
I_g	Reverse saturation current
$I(t)$	sinusoidal current
J_{CV}	Joint density of states

J_{sc}	Short circuit current density
K_B	Boltzmann's constant
K_λ	Extinction coefficient
m^*	Effective mass of electrons
m_c^*, m_v^*	Conduction band and valence band density of state effective mass respectively.
n	Charge carrier density
n_f	Refractive index
N_{co}, N_{vo}	Conduction band and Valence band density of state prefactors respectively
O^{2-}	Oxygen ions
P_f	Average film density
P_m	Bulk density
P_{max}	Maximum power
r	Particle radius
r_δ	Grain size
R	Resistance
R_{rec}	Recombination resistance
R_s, R_{tr}, R_{sh}	Series resistance, transport resistance and Shunt resistance respectively
V	Potential
V_{max}	Maximum voltage
V_{oc}	Open circuit voltage
Z	Impedance

LIST OF ABBREVIATIONS

a-Si	Amorphous silicon
CB	Conduction band
CBT	Conduction band tail
CdTe	Cadmium telluride
CE	Counter electrode
CIGS	Gallium diselenide
DOS	Density of state
DSSC	Dye sensitized solar cell
eV	Electron volts
EDXRF	Energy dispersive x-ray fluorescence
EIS	Electrochemical impedance spectroscopy
FF	Fill factor
Fs	Femtoseconds
FTO	Fluorine tin oxide
FWHM	Full width at half maximum
GW	Gigawatts
ITO	Indium tin oxide
I-V	Current –voltage
JDOS	Joint density of states
ms	Milliseconds
ns	Nanoseconds
Nb ₂ O ₅	Niobium (v) oxide
OJL	O’Leary-Johnson-Lim
Ps	picoseconds
Pt	Platinum
PV	Photovoltaics
RC	Resistor-Capacitor
SEM	Scanning electron microscope
TCO	Transparent conducting oxide
TiO ₂	Titanium dioxide

TOE	Tons of oil equivalent
TW	Terawatts
UV	Ultra-violet
VB	Valence band
VBT	Valence band tail
XRD	X-ray diffraction
ZnO	Zinc oxide

CHAPTER ONE

INTRODUCTION

1.1 Background of the Study

One of the major societal challenges is related to the rise in global energy demand. International Energy Outlook (2017) projects that world energy consumption will rise by 28 % between 2015 and 2040, going from 19.2 to 24.6 Terawatts. This increase in future demand and consumption is inevitable since developing countries also strive to have the same living standard as the developed ones. Today, we primarily use fossil fuels to heat and power our homes and fuel our cars. It is convenient to use coal, oil and natural gas to meet our daily needs. However, they are exhaustible and their combustion has resulted in environmental contamination and greenhouse effect. Research and development of renewable energy resources have therefore attracted great attention worldwide to address this problem.

Hydro-power (1114 GW) has been the main major sustainable energy sources for the longest period (Kaunda *et al.*, 2012), however, other renewable sources are likewise being brought to market. These sources include: wind power (539 GW), photovoltaics (402 GW), geothermal power (12.8 GW) and ocean power (0.5 GW) (Renewable Energy Policy Network, 2018).

Of all the sustainable energy sources, solar power is the most promising, perpetual and continually abundant, quiet and versatile to wide variety of uses from several hundred megawatts outdoor power plant that produce both heat and electricity to small off grid systems that can power areas of the rural settlement and dispersed developments. More energy from sunlight strikes the earth in 1 hour than all the energy demanded globally in an entire year (Tverberg, 2012). Figure 1.1 illustrates the solar radiation spectrum for sunlight at the top of the earth's atmosphere and at the sea level.

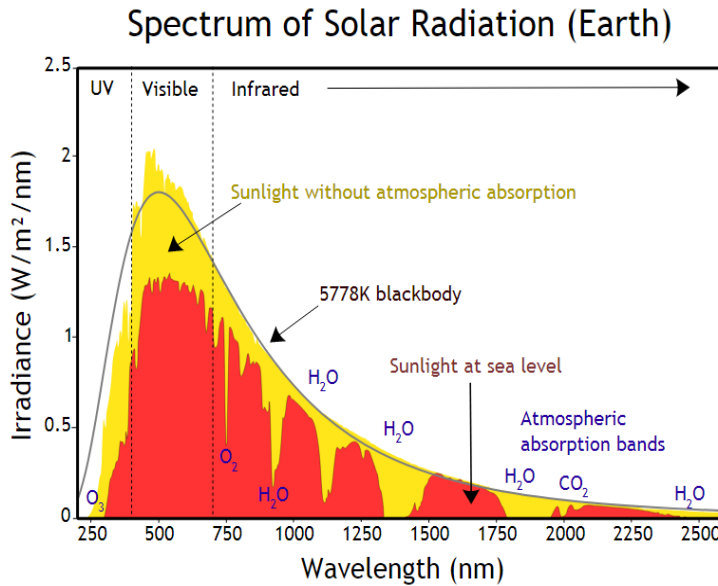


Figure 1. 1: Solar radiation spectrum for direct sunlight at both the top of the earth’s atmosphere (yellow part) and at the sea level (red region) (https://commons.wikimedia.org/wiki/File:Solar_spectrum_ita.svg, 2008)

Unfortunately, there is immense gap between abundance and exploitation of solar energy. The gap between the abundant solar radiation and its present utilization presents extraordinary challenge to research efforts to develop cost-effective solar cell technologies with ability to convert more sunlight to electricity.

1.2 Photovoltaics (PV)

Photovoltaic effect is a physical and chemical phenomenon in which light energy is converted into electrical energy. A photovoltaic cell is an electrical device that converts the energy of light directly into electricity.

1.2.1 Principles of photovoltaic conversion

All photovoltaic conversions depend on photoelectric effect in which light falling on semiconductor makes an electron-hole pair in it as demonstrated in figure 1.2. Electrons in the valence band (VB) get excited to the conduction band (CB) of the semiconductor upon

absorption of light of energy $h\nu$ thereby creating holes in the valence band. A built-in-potential barrier acts on the excited electrons making it flow through the external load thereby producing current before recombining with the holes in the valence band.

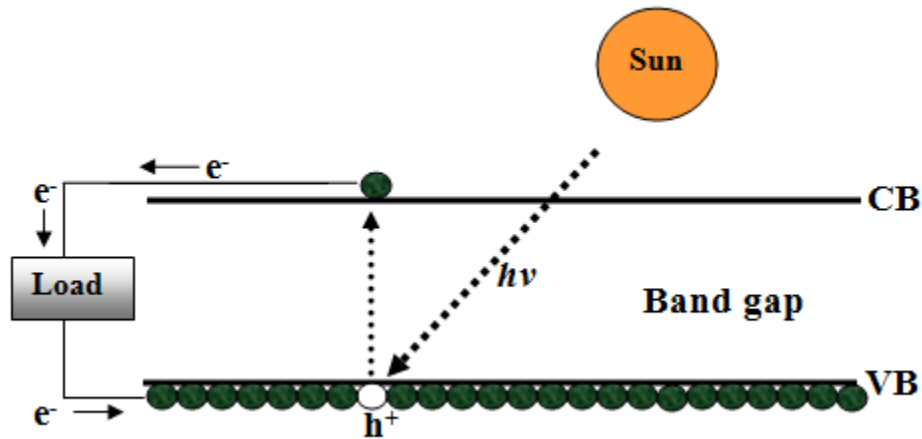


Figure 1. 2: Typical representation of photovoltaic effect. Electrons in the valence band (VB) get excited to conduction band (CB) of a semiconductor upon absorption of energy $h\nu$ from the sun creating holes h^+ in the valence band.

1.2.2 Classification of photovoltaic solar cells

Existing photovoltaic solar cells are categorized into three different groups as shown in figure 1.3. The first generation solar cells, otherwise known as conventional or silicon wafer-based cells, are made of crystalline silicon (c-Si) (Aoyama *et al.*, 2017). These types of PV cells are the commercially predominant photovoltaic technology due to their high efficiency and well-established technology.

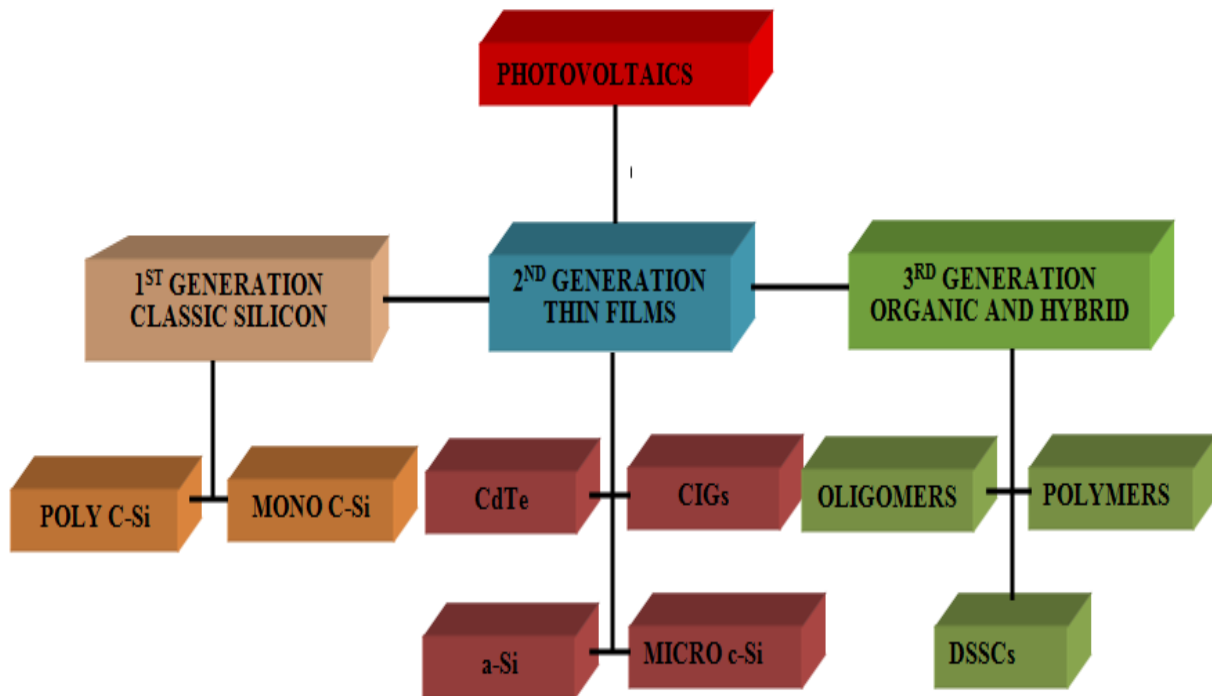


Figure 1. 3: Generations of Photovoltaics

Currently in the PV market, silicon based solar cells are the dominating technology accounting for 93 % of the total PV plant (Andreani *et al.*, 2019). However, Silicon being an indirect semiconductor with low optical absorption efficiency, therefore, Si wafers have to be as thick as over hundred microns to absorb more incident light. In addition to this, high cost of refining and crystallization process of silicon renders this technology highly expensive (Kaur and Singh, 2016). To confront this challenge, solar cells made of very thin photovoltaic materials were developed. This class of thin film solar cells forms the second generation solar cells.

Second generation solar cells also known as thin film solar cells, are made of photovoltaic material that is much thinner than c-Si solar cells. This effectively reduces their manufacturing cost allowing more straightforward production. The materials used are also widely available. They include copper indium gallium diselenide (CIGS), cadmium telluride (CdTe) (Song *et al.*,

2014) and amorphous silicon (a-Si) (Krasikov *et al.*, 2016). The toxic nature of the materials like cadmium and the scarcity of telluride and indium pose a major challenge to the development of this generation of solar cells. For this reason, this class of solar cell took off slowly even though they offered better material use and potentially faster manufacture. This made room for another generation of solar cells.

Third generation solar cells have frequently been portrayed as developing technologies. In comparison with high-cost conventional silicon solar cells, third generation solar cells are well known as a cost-effective photovoltaic devices because of inexpensive materials and simple fabrication process. They include thin film silicon solar cells (Haug and Ballif, 2015), dye sensitized solar cells (Andualem and Demiss, 2018), polymer based organic solar cells (Mayer *et al.*, 2007) and more recently, perovskite cells (Ren *et al.*, 2016). The greater part of them has not yet been popularized and is still in the development stage.

Regardless of their low efficiencies and stability issues of the absorber material, a lot of research has kept on investing into third generation solar cell technologies as they promise to be high efficiency solar cells. Figure 1.4 shows efficiencies for the different generation of solar cells. According to Green *et al* (2018) highly crystalline silicon solar cells have achieved an efficiency of 26 % which is close to the maximum theoretical efficiency limit (31 %) (Carella *et al.*, 2018).

Best Research-Cell Efficiencies

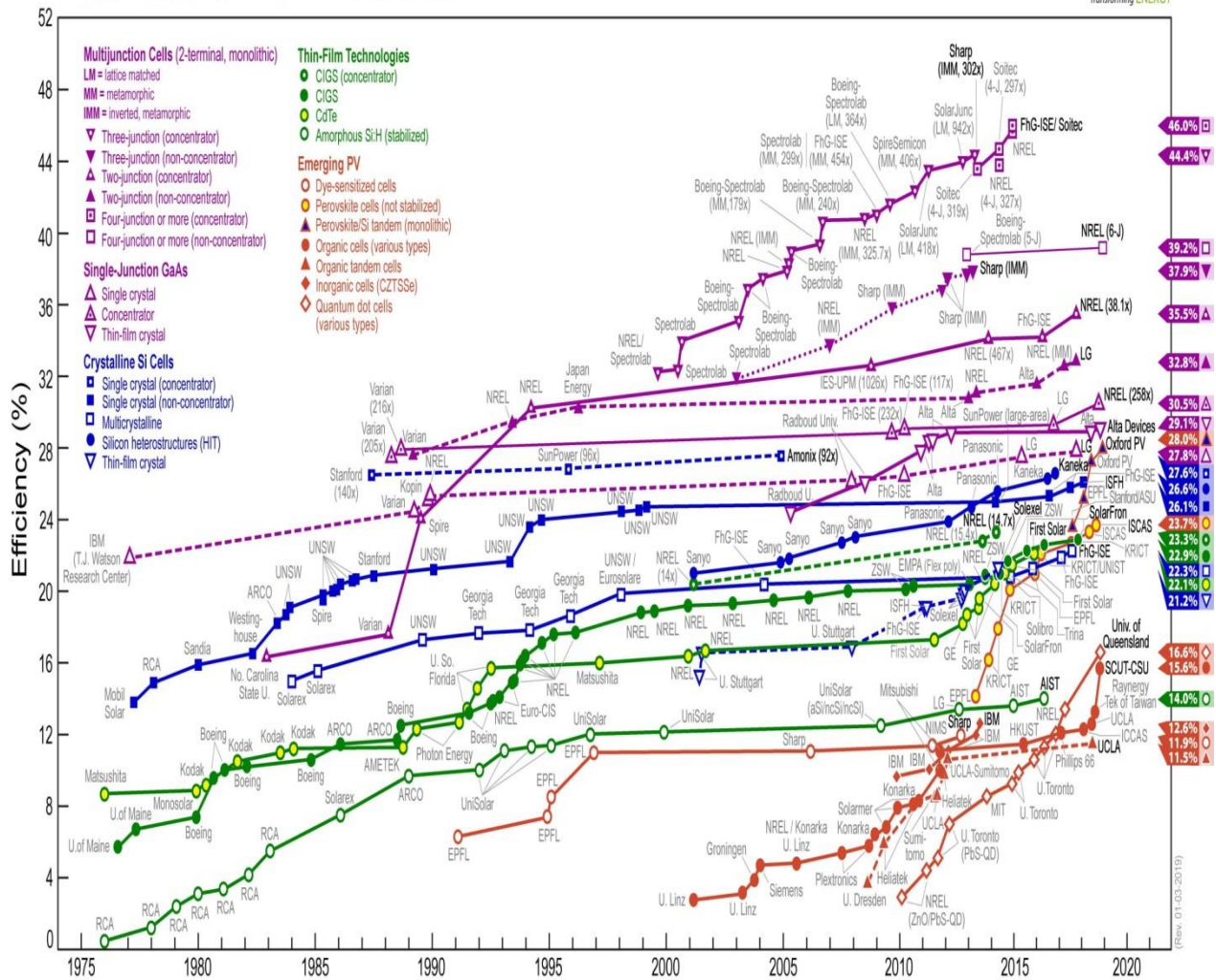


Figure 1. 4: Photovoltaic research cell record efficiency chart (National Renewable Energy Laboratory, 2018).

Among the 3rd generation photovoltaics is the dye sensitized solar cell which is based on nature’s principle of photosynthesis. The operation mechanism of dye sensitized solar cells by injection of electrons from photo excited dye molecules to the conduction band of the metal oxide semiconductor dates back to 1960s. O’Regan and Grätzel (1991) reported breakthrough in fabrication of DSSCs using titanium dioxide as the metal semiconductor. Research on these

types of solar cells has advanced at a fast rate and a considerable amount of work has been done to improve their efficiency from 7% in 1991 to 13% in 2014. However, these efficiencies are still low to enable DSSCs be introduced to the PV market. Considering the infinite variation in; material composition, synthesis, layer stacking, architecture and the substrates, DSSCs have the possibility to attain high efficiency at low cost compared to the first and second generation solar cells.

One of the very critical components contributing to this low efficiency is the composition of the metal oxide semiconductor which has not been fully explored. Nanocrystalline TiO_2 possess large surface area that is essential for adsorbing large amounts of dye except that it brings about many opportunities for recombination of photo-injected electrons which decreases the cell efficiency.

Modifications to the semiconductor composition have been performed in attempts to enhance the electron transport and minimize charge recombination. Composite metal oxide semiconductors for DSSCs have gained much interest because they seek to take advantage of the best properties of each material that makes up the composite. Wu *et al.* (2017a) reported a 2.3 % increase in efficiency of Ag- TiO_2 composite dye sensitized solar cell compared to that with pure TiO_2 photoelectrode. In their study, Nguu *et al.* (2014) obtained a conversion efficiency of 2 % for $\text{TiO}_2/\text{Nb}_2\text{O}_5$ composite DSSC. However, a number of important properties of the photoanode were not investigated in their work.

Three phase contact between transparent conducting oxide, semiconductor metal oxide and electrolyte in the dye sensitized solar cell play important role in electron transfer and recombination dynamics. It is in this regard that we sort to introduce a blocking layer so as to

minimize charge recombination taking place at the FTO/electrolyte interface and in addition, optimize the thickness of TiO₂ compact layer for DSSC application.

1.3 Statement of the Problem

Composite metal oxide semiconductor electrode has been used in DSSCs due to their promising properties which could enhance the conversion efficiency of the cells. Notably the efficiencies obtained from composite metal oxide semiconductor are still rather low with Nguu *et al.* (2014) reporting 2% conversion efficiency by using TiO₂/Nb₂O₅ composite as the photoelectrode. These low efficiencies are partly attributed to electron recombination taking place at the FTO/electrolyte interface. In view of the above, there is still a challenge of minimizing charge recombination at the FTO/electrolyte interface. Nicholas *et al.* (2018) reported an increase in efficiency from 1.31 % to 3.21 % with introduction of TiO₂ compact layer for dye sensitized solar cells made up of TiO₂ porous layer. To the best of our knowledge, TiO₂ blocking layers have not been exploited in fabrication of photoelectrodes with TiO₂/Nb₂O₅ as the porous layer for DSSC application. Therefore we seek to introduce TiO₂ compact layer and study its effect on photovoltaic characteristics of TiO₂/Nb₂O₅ composite dye sensitized solar cells.

1.4 Aim of Study

1.4.1 General objective

The main objective of this work was to study the effect of TiO₂ compact layers on the P-V characteristics of TiO₂/Nb₂O₅ composite electrode thin films deposited by spray pyrolysis technique.

1.4.2 Specific objectives

The specific objectives of this study were;

1. To deposit TiO₂ compact layer on conducting glass substrate by spray pyrolysis technique.
2. To determine the optical and electrical properties of TiO₂ compact layer.
3. To investigate the effect of TiO₂ compact layer on the overall performance of TiO₂/Nb₂O₅ dye sensitized solar cells.

1.5 Justification and Significance of study

Efforts are continually being undertaken to improve the performance of DSSCs and hence the competitiveness of this technology in the market. Performance of dye sensitized solar cells is measured by several parameters which are current density (J_{sc}), open circuit voltage (V_{oc}), fill factor (FF) and the energy conversion efficiency η . Since V_{oc} is determined by the potential difference between the redox level of the electrolyte and the flat band potential, higher open circuit voltage can be achieved by using an oxide with a higher flat band potential. Thus photoelectrochemical properties of DSSCs can be improved by tailoring the photo-electrode materials and their microstructure. The flat band potential of Nb₂O₅ lies slightly higher than that of TiO₂ with a correspondingly higher V_{oc} than that of TiO₂ electrode (Eguchi *et al.*, 2000). Nb₂O₅ has a conduction band in the range 0.2 – 0.4 eV higher than that of TiO₂ whose band gap value of 3.5 - 3.8 eV. This property makes it suitable for the formation of mixed-particle structure which could improve the electron transport and dye adsorption (Wei *et al.*, 2008). Composite metal oxides for dye sensitized solar cells have gained much interest due to the fact that they tend to take advantage of the best properties in each component that forms the composite.

Compact layers are used to suppress the electron recombination occurring at the interface between electrolyte and the transparent conducting electrode. TiO_2 compact layer has been used to improve the performance of DSSCs by minimizing charge recombination in the cell. In this work we introduce a TiO_2 compact layer on $\text{TiO}_2/\text{Nb}_2\text{O}_5$ with an aim of improving the conversion efficiency of the cell.

CHAPTER TWO

LITERATURE REVIEW

2.1 Introduction

In this chapter most of the aspects based on previous work related to the prime focus of the study are put together. It makes a point by description on every segment of DSSCs.

2.2 History of Dye Sensitized Solar Cells

The principle of solar cell operation is based on photovoltaic effect which was first observed in 1839 by Edmond Becquerel while investigating the effect of light on electrode immersed in electrolyte (Fraas, 2014). Selenium semiconductor coated with very thin layer of gold to form the junction was used to fabricate the first solar cell in 1894 by Charles Fritts. Low conversion efficiency of 1% was obtained from this solar cell (Wu *et al.*, 2017b). Successful development of selenium based solar cells was continued and the research extended into new materials for photovoltaic applications.

The idea of layered structured photovoltaic became prevalent when Bell laboratory designed the first practical cell with an efficiency of 6 % in 1954 (Rawal *et al.*, 2015). Tributsch (1971) made the first attempt to generate electricity from dye sensitized solar cell with zinc oxide as the semiconductor and chlorophyll as the sensitizer. Incorporation of dye molecules in some wide band gap semiconductor electrodes was a key factor in developing photoelectrochemical solar cells. O'Regan and Grätzel (1991) succeeded for the first time to produce dye sensitized solar cells of 7% efficiency by sensitizing a nanocrystalline TiO₂ film using novel Ru bipyridil complex.

The development of DSSC in 1990s opened up a new horizon and rapidly propelled photovoltaic technology into the era of third generation solar cells. Dye sensitized solar cells have been investigated and considered as the next generation solar cells due to their cost-effectiveness, abundance of raw materials, simple fabrication process and their general good photovoltaic performance with 13 % efficiency recorded (Shah *et al.*, 2016).

2.2.1 Transparent conducting electrode

These are electrical conductive materials with relatively high transmittance of light for effective light radiation conversion to electrical energy. The transmittance of the electrodes should ideally be 90% with sheet resistance not more than 10 ohms/square. Various transparent conducting oxides have been used for optoelectronic applications (Karsten *et al.*, 2017).

Commercially employed TCOs are n-type doped wide band gap oxide materials such as indium tin oxide ($\text{In}_2\text{O}_3:\text{Sn}$, ITO) (Ishibashi *et al.*, 1990), doped zinc oxide ($\text{ZnO}:\text{Al}$, $\text{ZnO}:\text{Ga}$, $\text{ZnO}:\text{In}$), fluorine tin oxide ($\text{SnO}_2:\text{F}$, FTO) (Widiyandari *et al.*, 2013) and amorphous indium gallium zinc oxide (InGaZnO_4 , IGZO) (Cho *et al.*, 2018). Indium tin oxide (ITO) has been greatly used due to its high transmittance and promising electrical conductivity (Wang *et al.*, 2013). However, indium which is used in the production of ITO has some disadvantages in terms of cost and production (Sharma *et al.*, 2018). This has led to exploration of other metal oxides having potentially better properties as transparent conducting electrodes that may replace ITO.

ZnO is considered the prime candidate due to its higher conductivity and low cost. It has excellent electrical, optical, mechanical and chemical properties as well as good thermal stability (Park *et al.*, 2013). Murugesan *et al.* (2018) developed Al-doped zinc oxide layer with enhanced

electrical and optical properties to substitute the ITO films. However, ZnO is more sensitive to oxygen and process control is more difficult.

Currently, fluorine tin oxide (FTO) is the most widely used TCOs as it has superior electrical and optical properties and are also of low cost. It shows high stability, high resistance to physical abrasion, especially when compared to indium tin oxide (ITO) and it is also abundant (Muthukumar *et al.*, 2013). Napi *et al.* (2016) reported improved efficiency of dye solar cells by enhancing the surface of FTO film.

2.2.2 Dye sensitizers

Efficient electron injection from the excited dye to metal oxide semiconductor plays a vital role in dye sensitized solar cells. Dye functions as electron donor upon excitation by the absorbed photons. Several materials have been studied before in attempts to come up with desirable dyes with better properties (Shiratori and Muraguchi, 2012).

Introduction of natural dyes as better replacement to organic dyes opens up a new direction of research in sensitizers. These types of dyes are cost effective, environmental friendly and biodegradable. One of the most widely available group of natural dye is the anthocyanins (Wongcharee *et al.*, 2007). They can easily bind to the surface of metal oxides semiconductors due to the presence of carbonyl and hydroxyl groups in them (Hao *et al.*, 2006). Unfortunately, the overall efficiencies of DSSCs based on natural dyes remains to be low with the best reported efficiency to be 7.6 % (Wang *et al.*, 2008).

Even though the application of organic dyes is limited by their high cost, non-availability and their complex synthesis (Qin and Peng, 2012), much attention has been put on ruthenium based complexes as photo-sensitizers due to their desirable photoelectrochemical properties and high

stability in oxidized state (Kohle *et al.*, 1997). The most commonly used ruthenium polypyridyl complex dyes for DSSCs are N3, N719, N749, and Z907. Much research is focused on improving the polypyridyl ruthenium dyes by bringing changes in their core structure (Nazeeruddin *et al.*, 2001). To further improve the conversion efficiency of Ru-based dye sensitized solar cells, much attention has been put on improving the spectral response of Ru-based dyes from near-IR to the whole range of VIS of the solar spectrum. Qin and Peng (2012) realized 11.9 % conversion efficiency of DSSCs sensitized by Ruthenium (II) based dyes with iodide based dyes absorbed on nanocrystalline TiO₂.

2.2.3 Redox electrolyte

Charge carrier transport between electrodes and dye regeneration after oxidation of its molecule is performed by the electrolyte in the cell. The electrolyte contains a redox couple in an organic matrix. In the recent years, solid electrolytes have found their application in DSSCs because of their high stability and high efficiency. Their use is however limited by some defects such as low charge transfer, high cost and complex preparation process.

Several attempts have been made to find suitable alternative to iodide/triiodide mediators. Such electrolytes are S/S^{2-} and $Co(II/III)$ (Caramori *et al.*, 2016). However, they are prepared in acetonitrile solution with low boiling point thereby limiting use of device at temperatures above the 80 °C, this also leads to instability issues such as short lifetimes and leakage in the device (Zheng *et al.*, 2017). For now, iodide/triiodide (I^-/I_3^-) is the commonly used redox electrolyte due to many advantages in high diffusion rate, low cost and ease of preparation (Tseng *et al.*, 2016).

2.2.4 Counter electrode

Counter electrode provides surface that enhances charge collection from the external circuit to the electrolyte and also acts as a catalyst that helps in regeneration of I^- from I_3^- . According to these basic functions, an effective counter electrode should have high catalytic activity, low resistivity, high surface area, chemical, electrochemical and mechanical stability and its energy level that matches the potential of the redox couple electrolyte.

Various materials have been evaluated for use as counter electrodes. The materials that have been investigated include carbon based nanomaterials such as carbon nanotubes (Murakami *et al.*, 2006), carbon soot, graphene, and graphite, inorganic semiconducting chalcogenide compounds such as NiS, CoS and CoSe and platonic composite materials (Roy-Mayhew *et al.*, 2010). These materials possess good electrical conductivity, have large surface area and are cost-effective. Their Production is cheap and they are also widely available (Yang *et al.*, 2013). However, Platinum Pt has consistently been used as a CE since it possesses high electrical conductivity, high catalytic activity and also provides stability against iodine corrosion in the electrolyte and also holds the record of highest conversion efficiency (Calogero *et al.*, 2011).

2.2.5 Metal oxide semiconductors

Metal oxide semiconductors have a major role to play in the performance of dye sensitized solar cells. Titanium dioxide (TiO_2), niobium pentoxide (Nb_2O_5) and zinc oxide (ZnO) are desirable materials exhibiting efficient electron transfer within dye sensitized solar cell depending on their electronic band structure (Kalyanasundaram, 2010).

Nb_2O_5 thin films were shown to exhibit similar properties as $TiCl_4$ post treated TiO_2 thin films (Černá *et al.*, 2011). It has also been shown that thin films of Nb_2O_5 or ZnO deposited on TiO_2

layer reduce charge recombination in DSSC (Kalyanasundaram, 2010). Nb_2O_5 dye sensitized solar cell with approximate thickness of $2.3 \mu\text{m}$ has been shown to improve conversion efficiency of the cell by 1.4 % (Kim *et al.*, 2015). It is considered as a suitable alternative to TiO_2 (Al-Juaid *et al.*, 2012). However, Nb_2O_5 is not widely available as TiO_2 because of its high demand as pigment in paints (Chen *et al.*, 2001) and *UV* absorber in the cosmetics industries (Abdul *et al.*, 2014).

Among all the wide band gap semiconductors explored as alternatives to TiO_2 as an electron conductor, ZnO presents excellent bulk electron mobility (Look *et al.*, 1998) with a band structure similar to that of TiO_2 and also has intriguing optoelectronic features. Yodyingyong *et al.* (2010) reported a conversion efficiency of 7 % for DSSC based on mesoporous ZnO sensitized with common ruthenium-based dyes prepared under different preparation conditions and electrolyte composition.

However, as a photoelectrode, ZnO has drawbacks such as chemically unstable and is easily dissolved in acidic and basic solutions and the amount of dye loadings is less than that of TiO_2 . TiO_2 is a wide band gap semiconductor existing in three main forms; anatase structure which is formed at lower temperatures and has wide band gap energy of 3.2 – 3.8 eV (Jose *et al.*, 2009a), brookite phase with band gap energy of 3.14 eV, and rutile phase with the least band gap energy 3.06 eV, possessing the highest refractive index and has the most thermodynamically stable structure. Their structure consists of a Ti atom surrounded by 6 oxygen TiO_2^{-6} in a more or less distorted configuration. Figure 2.1 shows the structures for different phases of titanium dioxide. The octahedron in anatase phase are connected by their edges forming a (001), in rutile, by vertices, forming (110) plane and in brookite by both edges and vertices (Diebold, 2003).

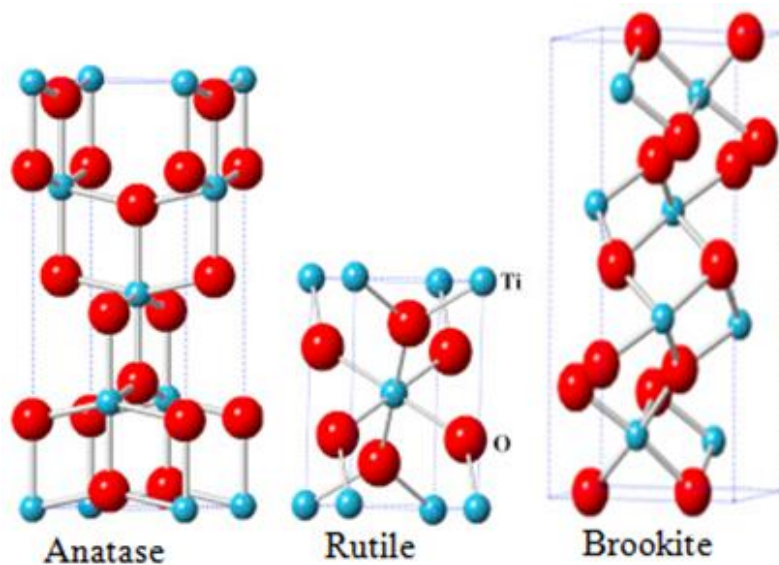


Figure 2. 1: Crystal structures for anatase, rutile and brookite phase of TiO_2 (Fujishima *et al.*, 2008).

TiO_2 has been the most successful metal oxide semiconductor used in DSSCs based on its unique properties such as its excellent band alignment with various organic and inorganic dyes, stability, non-toxic, low cost, available in abundance. It is widely used as a semiconductor in DSSCs to produce a high surface area for adsorption of a greater density of dye molecules, which produces a significant increase in the photocurrent (Meng *et al.*, 2010). However, the highly porous structure of TiO_2 layer cause recombination of the charge/electrons, which interferes with the unidirectional electron transfer that takes place at the TiO_2 layer/dye molecule and FTO/ TiO_2 layer interfaces (Kim *et al.*, 2012).

Efforts have been made to explore other materials such as composite metal oxide semiconductor in order to improve electron transport and minimized recombination in the cells. Such composites include $\text{SnO}_2/\text{TiO}_2$ (Bak *et al.*, 2011), $\text{TiO}_2/\text{ZrO}_2$ (Wang *et al.*, 2012), ZnO/ZnS (Rouhi *et al.*, 2015), MgO/TiO_2 (Wu *et al.*, 2008). Gao *et al.* (2012) used porous SnO_2 nanotube-

TiO₂ (SnO₂ NT-TiO₂) core shell structured photoanode which yielded a conversion efficiency of 5.11 % which was five times higher than that of TiO₂ nanoparticles. The conduction band of Nb₂O₅ is 100 mV negative than that of TiO₂ material. Thus Nb₂O₅ form an energy barrier to the photoelectrode and therefore confine the electrons to the core of TiO₂ particles. This electron confinement reduces the recombination thereby improving the V_{oc} . More research is still focused on TiO₂/Nb₂O₅ composite semiconductor for application in DSSCs though previous studies reported low conversion efficiencies. In this study, photoelectrodes formed by a mixed particle structure are expected to incorporate alteration in conduction band edge in the TiO₂ and Nb₂O₅ composite thereby yielding high V_{oc} .

2.2.6 Compact layer

The nanoporous electrode shows high surface area for light harvesting efficient electron injection. Unfortunately, high electron recombination occurs at the electrolyte/electrode interface for nanoporous electrode due to absence of energy barrier layer (Mebrahtu *et al.*, 2017). Charge transfer kinetics has been the focus of many researches in dye sensitized solar cells (Beek and Janssen, 2004). Effects of linear recombination kinetics that involves electron transfer in TiO₂ to redox couple in the electrolyte have been accounted for by several theoretical works (Bisquert and Mora-Seró, 2010). Recombination of photoelectrons at the interface of transparent conducting oxide/electrolyte is a disadvantageous reaction to efficient energy conversion in dye sensitized solar cells (Augustyniak, 2016).

To address this, compact layer has shown to be an effective alternative method to minimize electron recombination occurring at DSSC interfaces (Peng *et al.*, 2004). Figure 2.2 show a complete dye sensitized solar cell structure without a compact layer with possible recombination

paths and a DSSC with compact layer incorporated in its structure. Recombination of photo-injected electrons with the redox couple is prevented by the physically-blocked FTO/electrolyte interface.

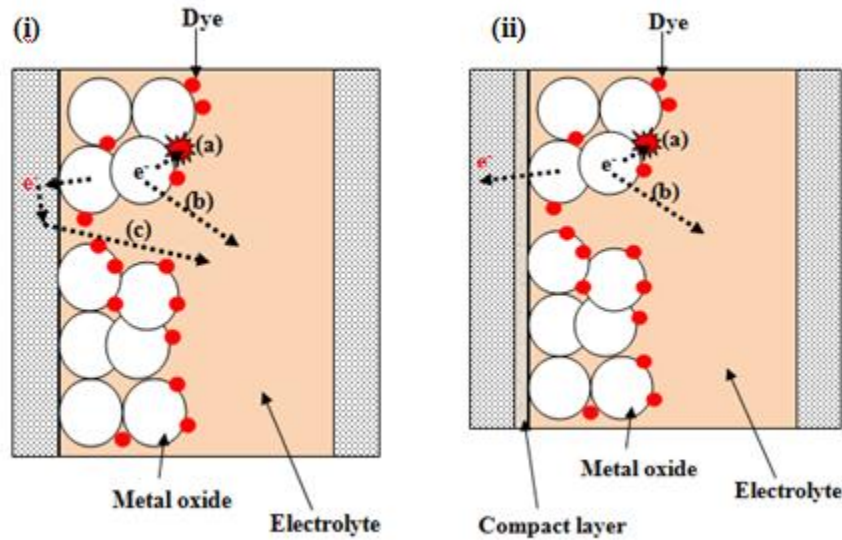


Figure 2. 2: Dye sensitized solar cell (i) without compact layer and (ii) Unidirectional electron transfer through the blocking layer. The three pathways for back reaction of electrons in a DSSC: (a) With the oxidized dye, (b) With the electrolyte via the TiO_2 , (c) With the electrolyte via FTO substrate

Additionally, compact layer improves the adhesion of porous layer to the conducting glass substrate contact area (Choi *et al.*, 2012). Semiconductors such as TiO_2 , Nb_2O_5 (Xia *et al.*, 2007) and ZnO (Roh *et al.*, 2006) have been used as blocking layers in DSSCs which, compared to the unblocked case had a higher photo-voltage and efficiency. Among them, TiO_2 is the most suitable candidate material as blocking layer.

Sputtering technique (Waita *et al.*, 2009; Xia *et al.*, 2006) and dip coating methods (Hong *et al.*, 2015) have been employed for the deposition of compact layer. However these techniques are expensive and deposition takes longer time. In this study, we seek to use spray pyrolysis method

to prepare blocking TiO_2 layer to maximize conversion efficiency of DSSC. This method is of low cost and faster compared to the other techniques.

CHAPTER THREE

THEORETICAL FRAMEWORK

3.1 Introduction

This chapter explains the theoretical aspect of optical properties of thin films and the operation principle of dye sensitized solar cells. Different models in SCOUT software used for determination of the optical constant are also discussed and also given are the fundamental theories on electrochemical impedance spectroscopy.

3.2 Optical Properties and Band gap Evaluation

The theoretical and experimental study of optical behavior of materials is used to obtain the optical constants such as refractive index n_f and extinction coefficient k_λ (Bhattacharyya *et al.*, 2009). The intensity of transmitted light through thin film depends on the incident photon wavelength and the material thickness. Taking reflectance of light on the film to be minimal, the intensity of transmitted light is evaluated as follows (Bouabellou, 2013);

$$I = I_o e^{-\alpha d} \quad (3.1a)$$

$$\alpha d = \ln\left(\frac{I_o}{I}\right) \quad (3.1b)$$

where, I is the transmitted light intensity, I_o is incident light intensity, α is absorption coefficient and d is the film thickness. Absorption of radiation that leads to electronic transitions between the valence and conduction band is split into direct and indirect transition. Near the absorption edge, the absorption coefficient is expressed as

$$\alpha \approx (h\nu - E_g)^\gamma \quad (3.2)$$

where $h\nu$ is the photon energy, E_g is band gap energy and γ is transition type equals to $\frac{1}{2}$ and 2 for direct and indirect transitions respectively (Hao *et al.*, 2018) . The optical band gap can be determined by Tauc's empirical model and using his equation, the relationship between absorption coefficient α and photon energy $h\nu$ can be established from the equation below (Ting *et al.*, 2000);

$$(\alpha h\nu)^{\frac{1}{\gamma}} = \beta(h\nu - E_g) \quad (3.3)$$

where β is a constant that depends on the properties of the material. When $(\alpha h\nu)^{\frac{1}{\gamma}}$ is plotted against $h\nu$, the tangent intercept gives E_g (Nikolay *et al.*, 2011). The energy by which photon strikes the film surface is given by;

$$\begin{aligned} E &= h\nu, \text{ but } \nu = \frac{c_o}{\lambda} \\ E &= \frac{hc_o}{\lambda} \\ E &= \frac{1240 \text{ eV}\cdot\text{nm}}{\lambda(\text{nm})} \end{aligned} \quad (3.4)$$

Where ν is the frequency, h is the Plank constant (6.63×10^{-34} J.s), c_o speed of light (3.00×10^8 ms^{-1}) and λ is the wavelength in nanometers. Theoretically obtained direct band gap values of titanium dioxide (TiO_2), $E_g = 3.2 - 3.9$ eV (Oommen *et al.*, 2013) and $E_g = 3.9$ eV for niobium pentoxide (Nb_2O_5) (Jose *et al.*, 2009a).

Theoretical analysis of experimental optical data was used to determine the optical constants of different thin films using various dielectric models. SCOUT software was used for the thin film

analysis by spectrum simulation of reflectance, transmittance, absorbance, ellipsometry, photoluminance and electroluminance. It can also be used to estimate thickness of the films (Theiss, 2000).

3.2.1 Drude model

Drude model (1900) is a classical model that assumes both electrons and ions as solid spheres. It is based on the kinetic theory of electrons in a material where assumed that the material has motionless positive ions and non-interacting electron gas (Ortega *et al.*, 2018; Barchiesi and Grosjes, 2014). This model links optical and electrical properties of a material with the behavior of its electrons or holes. The model well describes the electronic transition of free charge carriers.

The model has been shown to provide a fair explanation on cases where electrons are considered to have an appreciable interaction with each other and can be used to evaluate the optical properties at energies below the band gap accounting for interband transition of the conduction electrons. The model assumes that an incoming electromagnetic wave of frequency ω forces damped oscillation of the essential free electron in the semiconductor with damping constant Ω_τ . It involves a typical frequency (plasma frequency ω_p) above which the semiconductor reflectivity decreases. The plasma frequency is given as (Mendoza *et al.*, 2014);

$$\omega_p = \frac{1}{2\pi c_o} \left(\frac{4\pi n e^2}{m^*} \right)^{\frac{1}{2}} \quad (3.5)$$

where n is the charge carrier density, m^* is effective mass of electrons and c_o is the speed of light.

3.2.2 O’Leary-Johnson-Lim (OJL) model

The O’Leary-Johnson-Lim (OJL) model is used to describe the inter-band transition in semiconductor materials. The interband transitions are depicted by the model that assumes the parabolic shape of the density of state (DOS) function for the valence and the conduction bands with tail states exponentially decaying into the band gap. The shape of the conduction and valence band DOS are mathematically defined as a function of energy, predominantly by the parameters E_o (defining the gap between the band edges), mass (a scaling factor determining the shape of the DOS) and gamma (reflecting the width of the exponential band tails) (Solieman *et al.*, 2014). The fit parameters of the OJL interband transition model are the gap energy, E_V and E_C , (the gap between the band edges), the “damping constants” of the valence and conduction bands, γ_V and γ_C (gives the band tail width), the mass of the transition m (related to the strength of transition) and the decay factor f which drags down the imaginary part to zero at high frequencies (El-Amin and Solieman, 2015). In the OJL model, the refractive index n_f as a function of energy is determined mainly by the parameter ‘mass’, which determines the shape of the conduction and valence band DOS. The empirical equations of DOS functions were adapted to include the transition in each of the DOS functions between the band region and the tail region. That is;

Density of state function for the valence band edge;

$$f_v(E) = \frac{\sqrt{2}m_v^{*2}}{\pi^2\hbar^3} \begin{cases} \sqrt{E_v - E} & E \leq E_v - \frac{1}{2}\gamma_v \\ \sqrt{\frac{1}{2} - \gamma_v} \exp\left(-\frac{1}{2}\right) \exp\left(\frac{E_v - E}{\gamma_v}\right) & E > E_v - \frac{1}{2}\gamma_v \end{cases} \quad (3.6)$$

and density of states for the conduction band edge;

$$f_c(E) = \frac{\sqrt{2}m_c^{*\frac{1}{2}}}{\pi^2\hbar^3} \begin{cases} \sqrt{E-E_c} & E \geq E_c + \frac{1}{2}\gamma_c \\ \sqrt{\frac{1}{2}\gamma_c} \exp\left(-\frac{1}{2}\right) \exp\left(\frac{E-E_c}{\gamma_c}\right) & E < E_c + \frac{1}{2}\gamma_c \end{cases} \quad (3.7)$$

$f_v(E)$ and $f_c(E)$ are the density of states at the valence and conduction band respectively m_c^* and m_v^* are the effective masses of density of states at the conduction and valence band respectively. E_c and E_v denotes the sharp edges of conduction and valence bands, and γ_v and γ_c are the broadening spreads of valence band tail (VBT) and conduction band tail (CBT) states, respectively (Solieman and Abu-sehly, 2011).

The joint density of states (JDOS) $J_{cv}(\hbar\omega)$, associated with its broadened conduction and valence band is described by the following general equation (Saleh *et al.*, 2014)

$$J_{cv}(\hbar\omega) = \int_{-\infty}^{\infty} f_v(E) f_c(E + \hbar\omega) dE \quad (3.8)$$

The product of joint density of state and the oscillator strength yields the imaginary part of the dielectric function as described in the following equation

$$\varepsilon_i(\hbar\omega) = (\pi e)^2 \left(\frac{4}{3\rho_A} \right) \xi^2(\hbar\omega) J_{cv}(\hbar\omega) \quad (3.9)$$

Where $\xi^2(\hbar\omega)$ is the normalized dipole matrix element and ρ_A the atomic density of material.

The absorption coefficient can be determined by the product of JDOS and the normalized dipole matrix element squared as shown

$$\alpha(\hbar\omega) = \xi^2(\hbar\omega) J_{cv}(\hbar\omega) \quad (3.10)$$

3.3 Dye Sensitized Solar Cell Operation Principle

Upon irradiation with monochromatic light, the dye molecule on metal oxide semiconductor absorbs the light and gets excited from the ground state (D) at high occupied molecular orbital (HOMO) to the excited state (D*) at the lowest unoccupied molecular orbital (LUMO), thus emitting photogenerated electrons (Su'ait *et al.*, 2015).



Electron injection into conduction band of large band gap metal oxide semiconductor is caused by dye excitation upon which the dye molecule gets oxidized (D⁺).



The oxidized dye is regenerated by receiving electron from I⁻ redox mediator which is in turn oxidized I₃⁻ at the counter electrode with electrons flowing through the external load.

Conversion of light into electricity is the overall outcome of the whole process

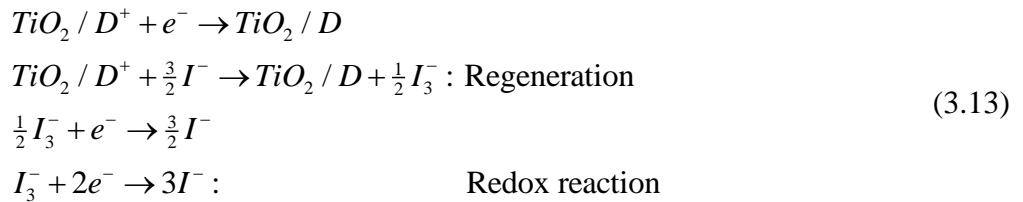


Figure 3.1 illustrates the electron kinetics in the dye sensitized solar cells.

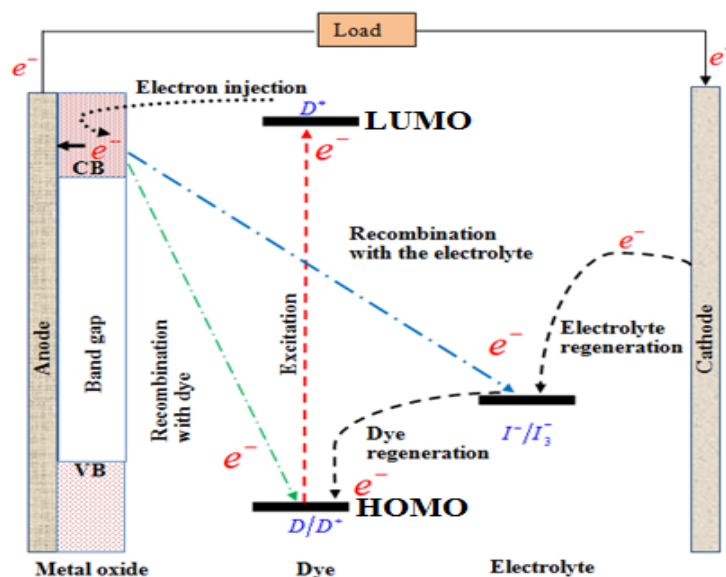


Figure 3. 1: Illustration of electron kinetics in dye sensitized solar cells

The arrows indicate dye excitation from the highest occupied molecular orbital (HOMO) level to lowest unoccupied molecular orbital level, excited state relaxation (60 ns), injection of electrons from lowest unoccupied molecular orbital (LUMO) level of the dye to conduction band of the semiconductor which is approximately 50 fs-1.7 ps, electron recombination with the hole in highest occupied molecular level of dye (ns-ms), charge recombination in conduction band of semiconductor with hole I_3^- in the electrolyte (10 ms) and oxidized dye regeneration by ions (Hara and Arakawa, 2005).

Electron injection kinetics to the conduction band of semiconductor after excitation from photosensitizers has been studied using time-resolved laser spectroscopy (Gan *et al.*, 2007). Efficiency of charge transfer to the semiconductor is greatly affected by photosensitizer configuration and energy separation between conduction band of semiconductor and lowest unoccupied molecular orbital (LUMO) level of the photosensitizer.

Photoelectric conversion processes in DSSCs can be understood through equivalent circuit which provides means to analyze cell devices and improve cell performance. The diode-like behavior in dye sensitized solar cells is as a result of charge transport at the metal oxide semiconductor/dye/electrolyte interface (Han *et al.*, 2004). Series and shunt resistance are included in the circuit to account for various losses mechanism in the device. Figure 3.2 shows one-diode model equivalent circuit for dye sensitized solar cells. The external load current is given as (Zaidi *et al.*, 2018);

$$I = I_{ph} - I_d - I_{sh} \quad (3.14)$$

where I_{ph} is the photogenerated current, I_d is the voltage dependent current lost to recombination and I_{sh} is the current lost due to shunt resistance. The diode current is modeled using Shockley equation for an ideal diode as;

$$I_d = I_g \left(\exp \left(\frac{-e(V-IR_s)}{\chi K_B T} - 1 \right) \right) \quad (3.15)$$

I_g is the diode reverse current, χ the ideality factor, R_s the series resistance, K_B Boltzmann's constant (1.38×10^{-23} J/K), e the elementary charge, T absolute temperature and V the potential.

The shunt current is given as;

$$I_{sh} = \frac{V + IR_s}{R_{sh}} \quad (3.16)$$

R_{sh} is the shunt resistance. The external load current is therefore expressed as;

$$I = I_{ph} - I_d \left(\exp \frac{-e(V-IR_s)}{\chi K_B T} - 1 \right) + \frac{(V - IR_s)}{R_{sh}} \quad (3.17)$$

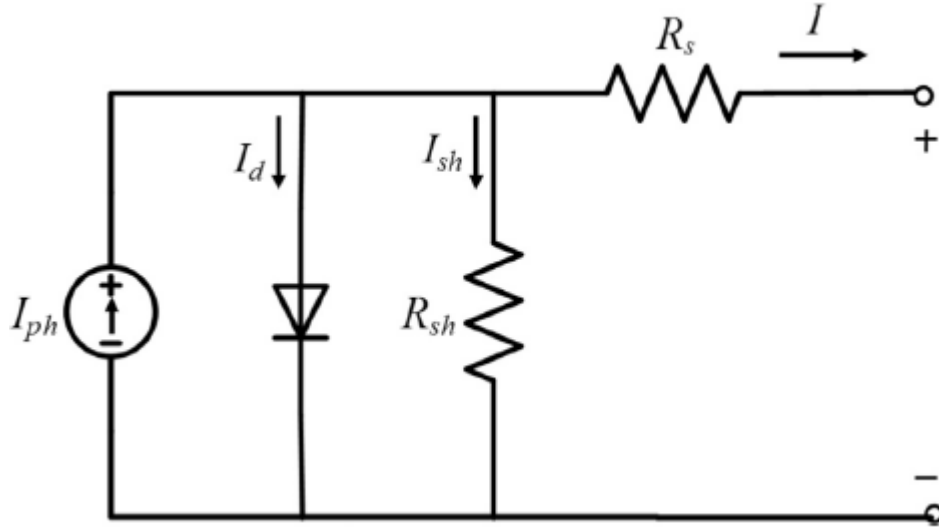


Figure 3. 2: One- diode equivalent circuit diagram for dye sensitized solar cells (Ghani and Duke, 2011)

3.3.1 Short circuit photocurrent (I_{sc})

Short circuit current is described as the current that flows between two photoelectrodes and is obtained from solar cell when load resistance is zero and mainly depends on photo-generated electrons and recombination of holes and electrons at the interfaces.

3.3.2 Open circuit potential (V_{oc})

This is the highest voltage achievable from solar cell at a given light intensity. It is the potential at which the current density through the cell is zero ($J_{sc} = 0$). It can also be expressed as the voltage difference between quasi-Fermi potential of electrons $\frac{E_{CB}}{e}$ in the conduction band and

redox potential of electrolyte $\frac{E_{redox}}{e}$ (Marinado *et al.*, 2010)

$$V_{oc} = \frac{E_{CB}}{e} + \beta_{\gamma} \frac{K_B T}{e} \ln \left(\frac{n}{N_{CB}} \right) - \frac{E_{redox}}{e} \quad (3.18)$$

where E_{CB} is the conduction band edge energy level, N_{CB} is the total number of conduction band states in the semiconductor, n is the number of electrons in semiconductor, and e is the elementary charge of the electrons. For the ideal case (i.e., a defect-free semiconductor material), $\beta_{\gamma} = 1$. Porous TiO_2 used in DSSCs often shows a non-ideal relation, $\beta_{\gamma} \neq 1$, where the origin might be additional electronic states referred to as trap states.

3.3.3 Series and shunt resistance

Series resistance (R_s) and Shunt resistance (R_{sh}) in solar cells are major factors affecting the conversion efficiency of the cell. High values of (R_s) and low (R_{sh}) lead to decrease in short-circuit current (I_{sc}) and open-circuit voltage (V_{oc}) respectively (Singh and Ravindra, 2012). Shunt resistance is caused by leakage current through the cell due to imperfections on the device surface (McIntosh and Honsberg, 2000). Shunt resistance can be obtained by inverse slope near the short circuit current I_{sc} . Low R_{sh} results in decrease in short circuit current of the cell thereby affecting maximum power output fill factor and the efficiency. Figure 3.3 shows the effect of shunt resistance and series resistance on the I - V curve. Shunt resistance is not affected by the intensity of illumination (Siddique *et al.*, 2013). Series resistance affects the energy output and fill factor of the cell (Cabestany and Castañer, 1983). Decrease in series resistance lead to improved open circuit voltage of the cells.

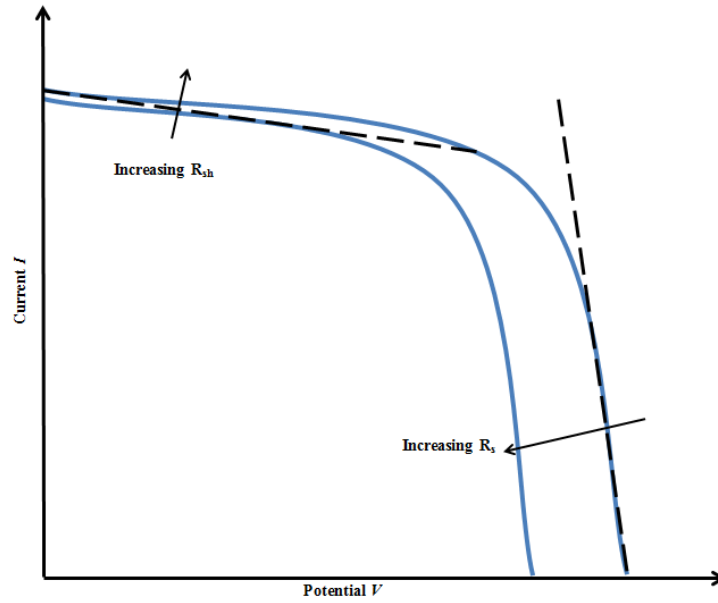


Figure 3.3: Effect of the series resistance shunt resistance R_{SH} on current-voltage characteristics.

3.3.4 Fill factor (FF)

This is ratio of maximum generated power to the product of open circuit voltage V_{oc} and short circuit current I_{sc} of a solar cell. For dye sensitized solar cells, it is a parameter used to specify the quality of solar cell by checking the extent of electrical and electrochemical losses in the cells. It is a function of series and shunt resistances of the cell. Shunt resistance should be increased while minimizing series resistance so as to obtain high fill factor of the device.

$$FF = \frac{I_{\max} V_{\max}}{I_{sc} V_{oc}} = \frac{P_{\max}}{I_{sc} V_{oc}} \quad (3.19)$$

where P_{\max} is the maximum power generated by the solar cell at voltage V_{\max} and current I_{\max} , I_{sc} is the short circuit current and V_{oc} is the open circuit voltage of the cell.

3.3.5 Power conversion efficiency (η)

This is the ratio of energy output P_{\max} from solar cell to energy input P_{in} at the surface of solar cell and it is generally expressed as a percentage.

$$\eta(\%) = \frac{P_{\max}}{P_{in}} = \frac{V_{\max} I_{\max} FF}{P_{in}} \times 100\% \quad (3.20)$$

where P_{\max} is maximum power output, P_{in} is incident radiation power, FF is fill factor, V_{\max} maximum voltage and I_{\max} maximum current at maximum power output. Figure 3.5 shows the $I-V$ characteristic curve for dye sensitized solar cell.

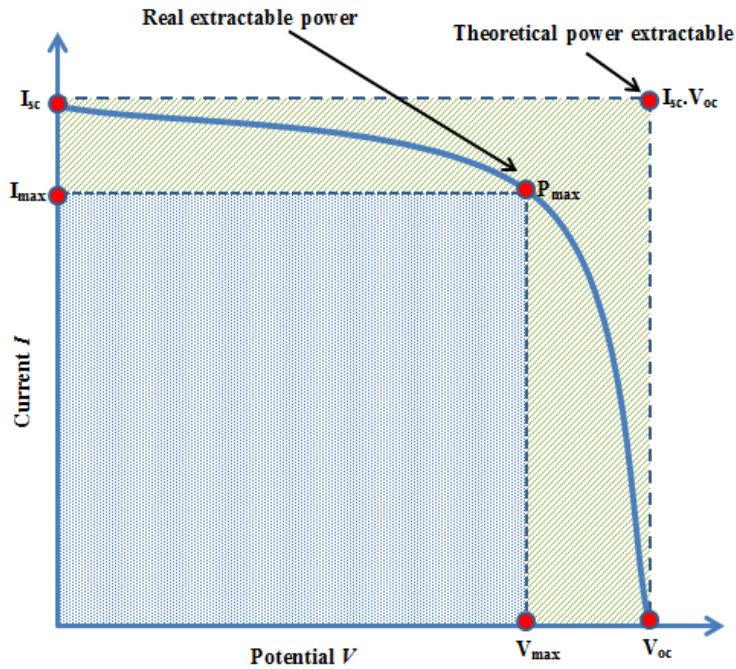


Figure 3. 4: I-V characteristic curve of dye sensitized solar cells.

3.4 Electrochemical impedance spectroscopy (EIS)

This is a widely used technique for characterization of the electrical properties and operation mechanism of solar cells (Sarker *et al.*, 2014). Impedance is the response of a cell to an applied potential whose frequency reveals the underlying chemical processes (Wang *et al.*, 2006). This technique involves determination of response of an electrode to sinusoidal potential modulation at different frequencies. EIS has been extensively used for determination of charge carrier lifetime under a range of operating biases and illumination intensities.

The main interest is the system response to the application of sinusoidal signal. The measurement is performed under sinusoidal potential modulation with amplitude 0.005 - 0.01 V. Sinusoidal perturbation of potential $E(t)$ induces a sinusoidal current $I(t)$ of the same frequency (ω) superimposed onto the steady state current with phase shift ϕ with respect to the potential. As for physical electric circuits, the electrochemical impedance of the electrode reaction (Z) is defined analogous to Ohms' law as (Lasia, 1999).

$$Z(\omega) = \frac{E(t)}{I(t)} = \frac{|E_o| \sin(\omega t)}{|I_o| \sin(\omega t - \phi)} = Z_o \frac{\sin(\omega t)}{\sin(\omega t - \phi)} \quad (3.21)$$

Here, E_o and I_o is the amplitude of the potential and current respectively, $\omega = 2\pi f$ is the radial frequency in rads/s.

With the mathematical identity;

$$\exp(jx) = \cos x + j \sin x \quad (3.22)$$

It is obtained that

$$E(t) = |E_o| \exp(j\omega t) \text{ and } I(t) = |I_o| \exp(j\omega t - j\phi) \quad (3.23)$$

From equation (3.15), impedance can also be expressed as the sum of real (Z_{re}) and imaginary (Z_{im}) parts at a given frequency ω as given in equation (3.17).

$$Z(\omega) = |Z_o| \exp(j\phi) = |Z_o| (\cos \phi + j \sin \phi) = |Z_o| \cos \phi + |Z_o| j \sin \phi = Z_{Re} + iZ_{Im} \quad (3.24)$$

Nyquist plot with the impedance can be represented by a vector (arrow) of length $|Z|$. The angle between this vector and the x-axis, commonly called the phase angle is ϕ ($=\arg Z$) as shown in figure 3.5.

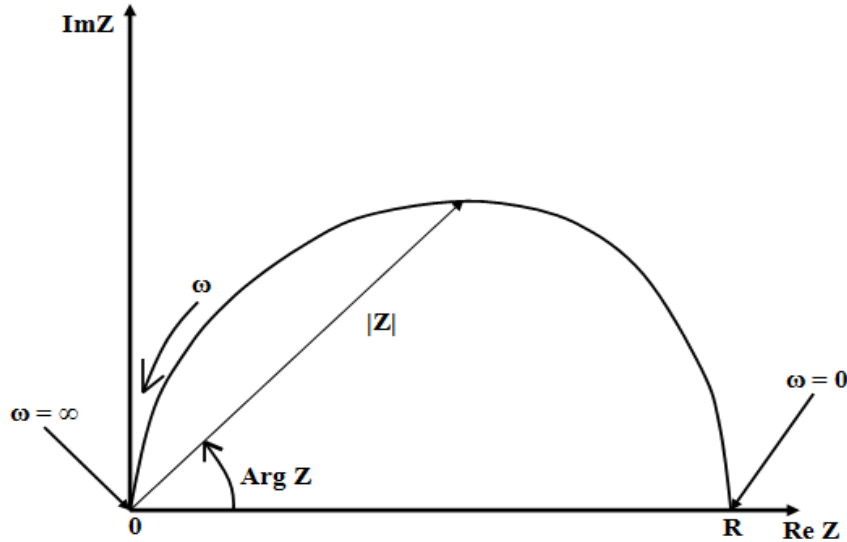


Figure 3. 5: Typical representation of impedance

A sinusoidal voltage applied to an ohmic resistance induces an alternating current that is in phase with applied voltage and the impedance of the ohmic circuit element is therefore equal to its resistance R:

$$Z_r = \frac{E(t)}{I(t)} = \frac{|E_o| \sin(\omega t)}{|I_o| \sin(\omega t)} = R \quad (3.25)$$

The impedance of the resistor is independent of frequency and has no imaginary component. The impedance of a capacitor can be calculated based on relation

$$I(t) = C \frac{dE(t)}{dt} \quad (3.26)$$

That yields the expression of capacitance impedance, its modulus and phase shift.

$$Z_c = -\frac{j}{\omega C}, \quad |Z_c| = \frac{1}{\omega C} \quad \text{and} \quad \phi = -\frac{\pi}{2} \quad (3.27)$$

The real and the imaginary parts of the impedance are related to phase angle θ as

$$\theta = \tan^{-1} \left(\frac{Z''}{Z'} \right) \quad (3.28)$$

And magnitude $|Z|$ as

$$|Z| = \sqrt{Z'^2 + Z''^2} \quad (3.29)$$

The operation of solar cell is governed by two competing processes. On one hand, photo-excitation and electron injection into the conduction band of the large band gap semiconductor which leads to creation of current that flows towards the external load. The other process involves recombination of the injected electrons thereby internally annihilating the moving carriers (Bisquert *et al.*, 2009).

Due to the complex nature of real devices, equivalent circuits are used to simulate the impedance behavior of such devices. These equivalent circuits ought to be complex enough to show approximately the same impedance characteristics as the real devices and at the same time simple for easy analysis (Krogmeier, 2016). The roles of internal cell surfaces as well as device

components have been studied by equivalent circuit element. Figure 3.6 shows a typical representation of an equivalent circuit dye sensitized solar cell.

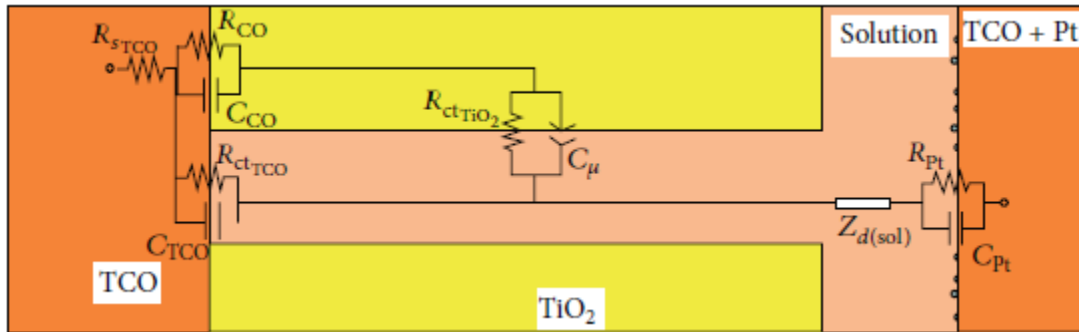


Figure 3. 6: Simplified transmission line equivalent circuit for a complete dye sensitized solar cell (Gu *et al.*, 2017)

$R_{ct_{TCO}}$ is a charge-transfer resistance for electron recombination from the uncovered layer of the TCO to the electrolyte, C_{TCO} double layer capacitance at exposed transparent conducting oxide (TCO)/electrolyte interface; $Z_{d(sol)}$ is the Nernst diffusion of I_3^- in the electrolyte, R_{pt} is the charge-transfer resistance at the counter electrode/electrolyte interface and C_{pt} is the double layer capacitance at the counter electrode/electrolyte interface. R_{CO} and C_{CO} are the resistance and the capacitance at TCO/TiO₂ contact, C_{μ} is the chemical capacitance of the TiO₂ film, $R_{ct_{TiO_2}}$ is the transport resistance of electrons in TiO₂ film and $R_{s_{TCO}}$ is the series resistance in the transparent conducting electrode.

Chemical capacitance is the measure of readiness for stoichiometric changes and it describes the electro-neutral chemical storage of charges. It is described as (Leever *et al.*, 2012);

$$C_{\mu} = e^2 \frac{\partial N}{\partial E_{fn}} = e^2 \frac{N}{k_B T} \quad (3.30)$$

C_{μ} is the chemical capacitance per unit volume, e is the elementary charge, N is the electron contribution and E_{fn} is the quasi-Fermi level generated by excess electrons in the acceptor.

Recombination resistance R_{rec} is introduced as part of the equivalent circuit. It is related to the recombination current density J_{rec} following the expression (Garcia-Belmonte *et al.*, 2010);

$$R_{rec} = \frac{1}{A} \left(\frac{dJ_{rec}}{dV_{oc}} \right)^{-1} \quad (3.31)$$

where A is the device area.

CHAPTER FOUR

MATERIALS AND METHODS

4.1 Introduction

In this chapter, appropriate experimental details of preparation of the dye sensitized solar cell, $\text{TiO}_2/\text{Nb}_2\text{O}_5$ composite thin film characterization and analysis employed in this work are described. The chapter details the techniques by which TiO_2 compact layer and $\text{TiO}_2/\text{Nb}_2\text{O}_5$ composite thin films were prepared.

4.2 Fabrication of the Photoanode

Prior to deposition of TiO_2 compact layer, the FTO substrates were cleaned in steps as outlined below. A gross cleaning process was performed to get rid of large amounts of contaminant off the surface of the substrates. This was achieved by scrubbing the surface of the substrates using a cotton bud dipped in a solution containing a mixture of sodium hydroxide, detergent and deionized water. To further remove specific contaminants such as oils or organic residue off the surface of the substrates, solvents were used. Unfortunately, solvents themselves (acetone) leave their own residue on the surface of the substrates. This is why three solvents were used. For vigorous cleaning, the substrates were agitated in ultrasonic bath for fifteen minutes at each step to ensure that every spot on the surface of the substrate was cleaned. The substrates soaked in acetone were agitated in ultrasonic bath after which they were soaked in ethanol and agitated once more and finally the substrates were soaked in deionized water before drying. The cleaned substrates were then left to dry in open air for 30 minutes before being used for deposition of the thin films.

4.2.1 Spray pyrolysis

500 μl of commercial titanium (IV) isopropoxide ($\text{TiCl}_3\text{H}_2\text{O}_4$) (99.7% pure, Aldrich) and 100 ml 2-propanol ($\text{C}_2\text{H}_8\text{O}$) (99.5%, Aldrich) were mixed in a 500 ml beaker. To maintain a homogenous mixture, magnetic stirrer was used to mix the content at a constant temperature of 35 °C for about 45 minutes. This solution formed the precursor which was atomized by the spray system using compressed air as the carrier gas (Holmarc, Optomechatronics PVT. Ltd). The set up used is shown in Figure 4.1

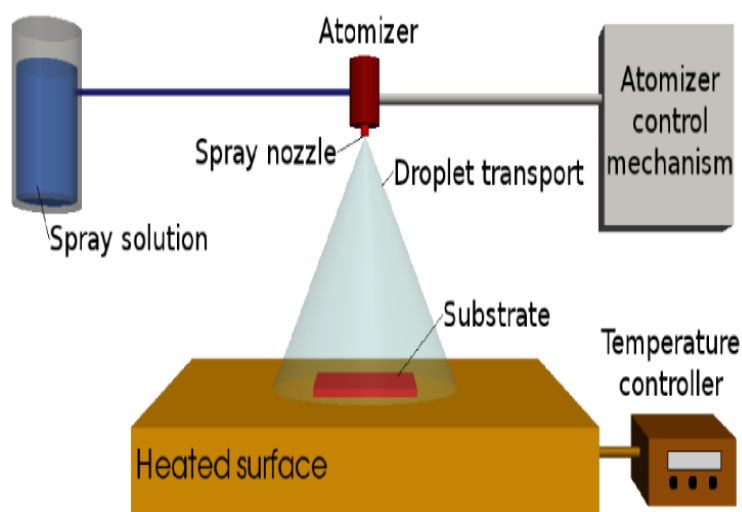
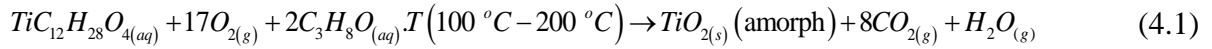


Figure 4.1: Schematic diagram for spray pyrolysis technique

FTO glass substrates (20 mm x 20 mm x 1mm) were mounted on the heating plate and preheated to 200 °C before deposition. Preheating the substrates enables every droplet to undergo pyrolytic (endothermic) decomposition and form single crystal or a cluster of crystallites as a product. The hot substrate surface provides thermal energy for thermal decomposition and subsequent recombination of the constituent species resulting to formation of film. The distance between the substrate and the spraying nozzle was set at 100 mm followed by 150 mm. Spraying was done in pulses, each pulse consisting of 5 seconds of spraying and 30 seconds of pause, at a precursor

flow rate of 2.0 ml/min. The chemical reaction resulting in the formation of amorphous TiO₂ thin film was as follows:



The deposited TiO₂ thin layers were then annealed in an open air furnace (Jlabtech) step wise at 500 °C for one hour to ensure complete crystallization of the film.

4.2.2 Compact layers with varying thickness deposited by spray pyrolysis

In order to deposit compact layer with different thickness, substrate-nozzle distance was set at 100 mm and 150 mm and deposition time also varied from 60 seconds to 120 seconds for each deposition distance. The substrate temperature was kept constant at 200 °C. The deposited films were then annealed and subjected to optical characterization where transmittance was measured using *UV- VIS* spectrophotometer (Perkin Elmer Lambda 25) in the wavelength range 200 < λ < 1100 nm. Thickness of the films was determined using Scout software.

4.3 Preparation of Porous TiO₂/Nb₂O₅ Composite Thin Films by Screen Printing Technique

Optimization of the mixing ratios of TiO₂ and Nb₂O₅ powders used in the formation of TiO₂/Nb₂O₅ composite is described in this section. Commercially acquired TiO₂ powder (CAS NO: 13463-67-7, Aldrich) and (Nb₂O₅) nanopowder (CAS NO: 1313-96-8, Acros Organics BCBA, Belgium) were used for the formation of porous TiO₂/Nb₂O₅ composite thin films. Varying ratios of the two powders were mixed with 2 ml of 2-propanol (IPA: isopropyl alcohol, Scharlan Chamia) and 2 ml of deionized water. Nano-particles of the two powders were mixed by increasing the proportion by mass of Nb₂O₅ from (0.1 to 0.9 g) while decreasing the proportion of TiO₂ (from 0.9 to 0.1 g).

Thin $\text{TiO}_2/\text{Nb}_2\text{O}_5$ composite layers with were coated on FTO glass substrate using screen printing mesh (63T, silk screen printing services LTD, USA). The films were then dried in air at ambient temperature for 10 minutes, transferred to a hot plate at 120 °C for five minutes and allowed to cool to room temperature before sintering stepwise at 500 °C for one hour in a tube furnace. Figure 4.2 shows the deposition of $\text{TiO}_2/\text{Nb}_2\text{O}_5$ composite thin film by screen printing technique.

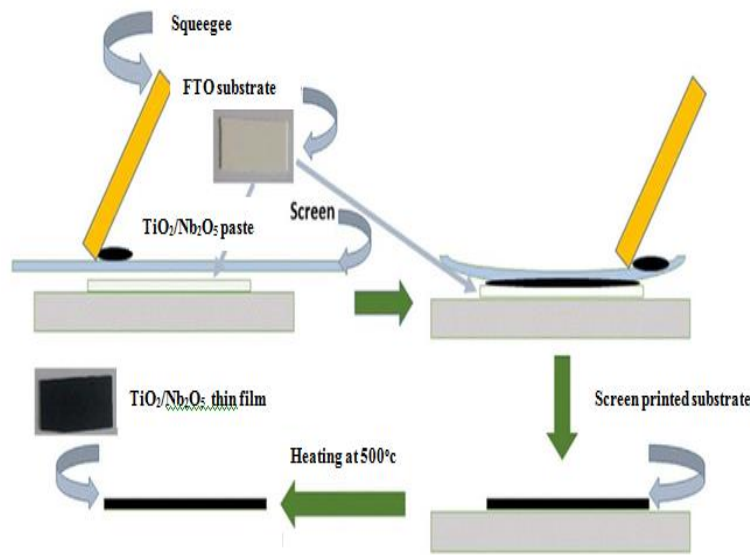


Figure 4.2: Schematic diagram for deposition of $\text{TiO}_2/\text{Nb}_2\text{O}_5$ composite thin film by screen printing technique

4.4 Thin Film Characterization

To compare the optical characteristics of the deposited TiO_2 compact layers, both the optical transmittance (T) and absorption (A) were measured in the wavelength range 300 -1100 nm ($UV-VIS$ range) on a computerized double beam spectrophotometer (Perkin Elmer Lambda 25). Using the experimentally obtained optical transmittance data in SCOUT 4.06 software, optical constants such refractive index n_f and extinction coefficient k_α and thickness of the samples

were obtained. Drude and OJL dielectric function models were used to give best fitting results for the optical spectra of semiconductor and metal oxide structure (El-Amin and Solieman, 2015). These functions were used to describe the fit parameters for the optical data of TiO₂ compact layer and TiO₂/Nb₂O₅ porous layers. In order to determine the optical band gap of the films, the absorption coefficient α obtained from the simulated data in SCOUT software was plotted in Tauc plot as discussed in section 3.2 of chapter 3, where the direct band gap was determined by extrapolating the linear section of the curve to zero. Electrical properties of the films were evaluated using Drude's parameters; plasma frequency Ω_p and damping constant Ω_γ .

4.5 TiO₂/Nb₂O₅ Elemental Analysis using EDXRF Spectrometer

In this study, energy dispersive X-ray fluorescence spectrometer Shimadzu series EDX-800HS, model CE (212-23701-36), was used to determine the amounts of Ti and Nb composition in the samples. The spectrometer consisted of the following;

- i. X-ray generator unit consists of an air cooled of X-ray tube with Rh target operated at 5-50 kV, tube current 0.001-1 mA; primary X-ray filters, automatically switched with an exposure area of 10mm in diameter – four settings 1, 3, 5 and 10 diameters are available for automatic switching.
- ii. Semi-conductor Si (Li) detector 10 mm² mounted at 45 ° take-off angle geometry with respect to the sample. It is cooled by liquid nitrogen only during measurement with approximate consumption of 1 liter per day. The detector is biased with a high voltage supply at 50 kV and is connected to a pre-amplifier. The detector measured resolution of about 140 eV for Mn $K\alpha$ at 5.9 KeV.

To determine the elemental composition of the samples, screen-printed $\text{TiO}_2/\text{Nb}_2\text{O}_5$ composite thin films were analyzed for 50 sec and 100 sec. The elements of interest, Ti and Nb were analyzed following sample irradiation with Rh-tube source. The characteristic fluorescence irradiation of the elements was detected with Si (Li) detector. Figure 4.3 shows the energy dispersive X-ray fluorescence set up used for the analysis of the prepared thin films.

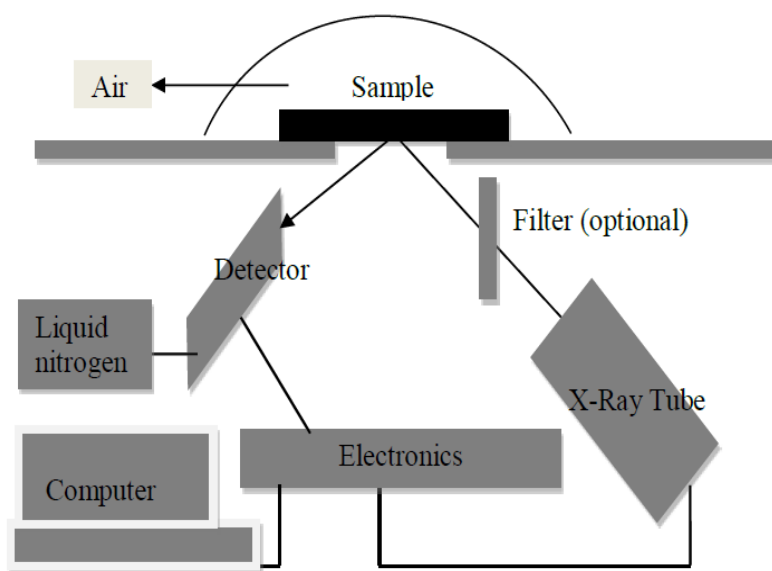


Figure 4.3: Schematic diagram of energy dispersive x-ray fluorescence set up

4.6 Raman Spectroscopy

Raman spectra are extremely helpful for phase identification with TiO_2 . Both anatase and rutile are composed of octahedral molecular geometry with the same $(\text{TiO}_2)^{8-}$. However, the arrangement and distribution are not the same because the connection of their two octahedral structures is different. So, they belong to two different space groups. As such, they have their own characteristic peaks in Raman spectrum (Ohsaka *et al.*, 1978).

Raman spectroscopy was performed to determine the phases of TiO_2 present in the films. The Raman spectra were recorded in a back-scattering geometry using a Raman spectrometer (STR Raman, CORNES Technologies Ltd, Tokyo). During acquisition of Raman spectra, an exposure time of 10 seconds was used as per the optimized conditions. A confocal microscope with 100 \times objective eye piece lens with laser power of 8.52 mW for 785 nm laser was used for measurement. Different films were characterized by taking several Raman spectra at random positions on each film with an area of 0.56 cm^2 .

4.7 Electrical Characterization

The sheet resistivity of the films was determined using four point probe (JANDEL) interfaced with Keithley 2400 source meter. In a four point probe, all the four probes are in a straight line as shown in figure 4.4. A calibrated constant current of source 4.53 mA was passed through the outer probes. Measurements were taken by pressing the four-point probe to the surface of the films. A source current was then activated and the sheet resistance values displayed by the Keithley meter.

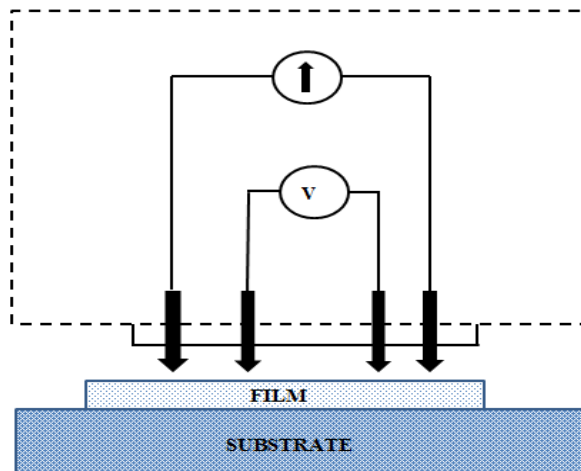


Figure 4.4: Illustration of four-point probe. The inner probes for measuring voltage and the outer probes measuring current.

SCOUT software was also used to validate the measurements obtained from four point probe. Electrical properties were analyzed by use of the Drude model based on transmittance data obtained from the *UV-VIS* spectrophotometer. The response of free carriers to the oscillating electric field was described, to a good approximation, by the Drude model. It is a free electron contribution model which describes the intraband contributions to the optical properties. The model has two adjustable parameters; plasma frequency ω_p and damping constant Ω_τ .

The parameters of the model relate the concentration of the charge carriers and their mobility to properties of the dielectric function. After a model parameter fit of the simulated spectrum and measured data, the carrier concentration and resistivity was computed. The Drude model relates the macroscopic susceptibility to microscopic quantities carrier concentration n , mobility μ and resistivity ρ by the following expressions (Maghanga and Mwamburi, 2018; Jayasinghe *et al.*, 2012).

$$n = \frac{4\pi^2 c \epsilon_o m^*}{e^2} \omega_p^2 = 3.35 \times 10^{14} \text{ cm}^{-1} \omega_p^2 \quad (4.2)$$

$$\mu = \frac{e}{m^*} \frac{1}{c_o \Omega_\tau} = 1.96 \times 10^3 \frac{1}{\Omega_\tau} \quad (4.3)$$

$$\rho = \frac{\Omega_\tau}{2\pi c_o \epsilon_o \omega_p^2} = 6.0 \times 10^1 \Omega \frac{\Omega_\tau}{\omega_p^2} \quad (4.4)$$

In the above equations, e is the elementary charge (1.6×10^{-12} C), c_o is the speed of light in vacuum, ϵ_o is permittivity of free space (8.854×10^{-12} As/Vm) and m^* is the effective mass of charge carriers ($m = 0.3m_o$), m_o is the mass of an electron, Ω_τ is the damping constant and ω_p is

the plasma frequency. Sheet resistance R_{Ω} of the films was obtained by using the following equation;

$$R_{\Omega} = \frac{\rho}{d} \quad (4.5)$$

Where ρ is the resistivity and d is the film thickness.

4.8 Morphological and Structural Characterization

Scanning electron microscope (SEM) (ZEISS ULTRA PLUS FEG SEM-Microscopes) was used to study the surface morphologies of the deposited thin films. The films were characterized without any further treatment before the scanning was performed. Micrograph images were taken at a constant acceleration potential of 5 kV.

X-ray diffraction (XRD) was performed to identify the crystal structure and the preferred orientation growth of the thin films. This was carried out on Bruker D2 PHASER diffractometer with CuK_{α} X-ray radiation (1.5418 Å) and readings were taken over the $10^{\circ} < 2\theta < 80^{\circ}$ range at a scan speed of 0.6 °/s and steps of 0.01 °.

4.9 Preparation of the Electrodes, Counter Electrodes and DSSC Assembly

Subsequent to the formation of the dense and the porous layers of the anode, the thin films were chemisorbed with the dye and used to assemble the DSSC. Preparation of the dye, electrolyte and the counter-electrode was as follows: A synthetic ruthenium-dye (N-719) solution of 0.5 mM was prepared by dissolving 6 mg of Ru-719 in 10 ml of ethanol and sonicated for thorough mixing. The formed thin films were preheated to 200 °C for 15 minutes to get rid of adsorbed water. This was then followed by scrapping some parts to form an active area of 0.56 cm².

The films were immersed into the dye solution immediately after heating to prevent re-adsorption of water. The films were soaked for 24 hours to enable proper dye chemisorption. The photoelectrodes were thereafter rinsed with ethanol to detach the excess/unabsorbed dye molecules after which they were immediately used as the photoanode.

4.9.1 Counter Electrode

Pre-drilled FTO glass substrates were cleaned following the procedure outlined in section 4.2. The glass substrates were then dried in open air and platinum (Platisol T/SP Solaronix SA, Switzerland) was coated on the pre-drilled FTO glass substrate and heated in tube furnace at 450 °C for 45 minutes. The counter electrodes were then cooled in dry air before use.

4.9.2 Solar Cell Assembly

The photoanode was prepared as follows: $\text{TiO}_2/\text{Nb}_2\text{O}_5$ composite coated on TiO_2 compact layer were sintered at 200 °C to eliminate absorbed water then the films let to cool to 80 °C. The films were immediately dipped in ruthenium dye complex (N719) that was at room temperature for 24 hours. The dye sensitized films were subsequently rinsed in ethanol to eliminate any excess dye and dried on a hot plate for 10 minutes at 70 °C. Figure 4.4 shows the assembled dye sensitized solar cell.

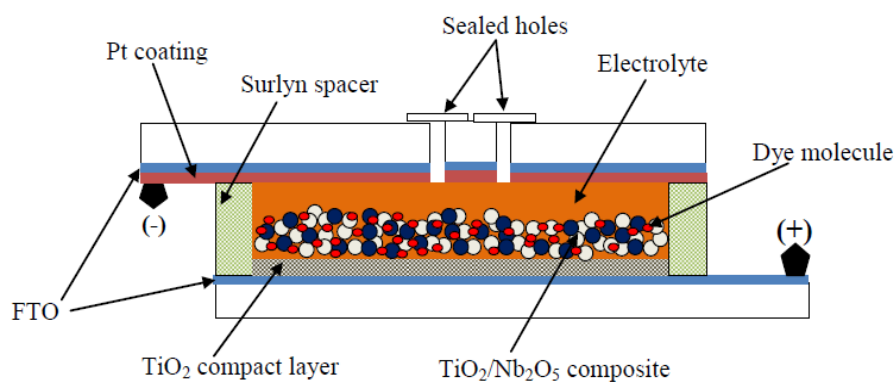


Figure 4.5: Complete assembly of dye sensitized solar cell

The photoelectrodes were then fused together with the counter electrode in sandwich manner with 60 μm thick thermoplastic sealing film made of surlyn (Solaronix, Switzerland) applying mechanical pressure at a temperature of 100 $^{\circ}\text{C}$. Iodide/tri-iodide electrolyte was dropped onto the hole in the counter electrode and injected into the cell by vac ‘n’ fill syringe.

4.10 Current-Voltage (*I-V*) Characterization of the Solar Cell

Current-voltage (*I-V*) characteristic were obtained using a set-up consisting of a 500 W xenon lamp, a solar simulator model SS (Science Tech, Canada) equipped with a 1.5 AM filter interphased with a Keithley 2400 (Keithley Inc, USA) source meter controlled by a computer. The measurements were carried out under the intensity of 1000 Wm^{-2} (AM 1.5) at the surface of the solar cell. The solar cells had active area of 0.56 cm^2 .

4.11 Electrochemical Impedance Spectroscopy (EIS)

Figure 4.5 shows the setup for electrochemical impedance spectroscopy measurement of the DSSCs. The measurement was performed using potentiostat (AUTOLAB, PGSTAT 204). The cells were illuminated with red light ($\lambda = 627 \text{ nm}$) and spectra obtained under 0.1 sun illumination with varying bias voltage between 0.5 – 0.70 V.

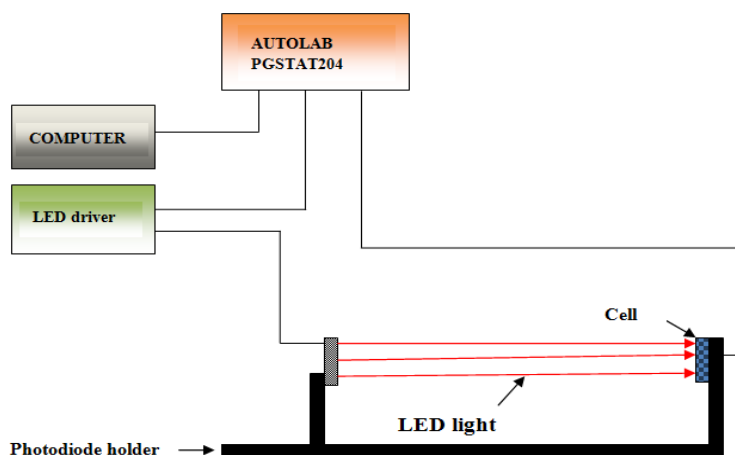


Figure 4.6: Electrochemical impedance spectroscopy measurement set up

In this study, the impedance was measured at frequency range of 100 kHz – 0.1 Hz. The impedance data obtained from the potentiostat was then analyzed in *Matlab* software. The function *ZfitGUI* obtained from (Dellis, 2018) was used to plot and fit the data. Equivalent circuit was as well defined in the *Matlab* software.

The starting parameters were picked for the fitting process. The value of recombination resistance was estimated by taking the diameter of Nyquist plot semicircles. The starting value for chemical capacitance was set to 10^{-8} Fcm⁻² while the geometrical capacitance was set to a constant value calculated from the cell thickness using equation (Govindasamy *et al.*, 2016).

$$C_g = \frac{\epsilon_o \epsilon_r A}{d} \quad (4.6)$$

where ϵ_o is the dielectric constant of vacuum, ϵ_r is the relative dielectric constant, A is the area of the cell and d is the thickness of the cell.

CHAPTER FIVE

RESULTS AND DISCUSSIONS

5.1 Introduction

In this Chapter, the results obtained from TiO₂ compact layer and TiO₂/Nb₂O₅ composite thin film and solar cells fabricated from these films are presented. Optical, electrical and structural properties of TiO₂/Nb₂O₅ composite are discussed. Current-voltage characteristics of solar cells fabricated with and without blocking layers are also presented.

5.2 Structural Characterization of TiO₂ Compact Layer and TiO₂/Nb₂O₅ Composite Layer

5.2.1 Analysis of Raman spectra

Raman spectra of TiO₂ films deposited by spray pyrolysis technique with the substrate temperature at 200 °C and annealed at 500 °C for one hour is shown in figure 5.1. The spectra in the range of 50 -700 cm⁻¹ show five allowed bands at 143 cm⁻¹ (*E_{og}*), 196 cm⁻¹ (*E_{og}*), 396 cm⁻¹ (*B_{1g}*), 504 cm⁻¹ (*B_{1g}*) and 637 cm⁻¹ (*E_{og}*) respectively for annealed films. These peaks are identical with the features of anatase phase as also reported by Kamran (2014). The peaks were similar for the annealed films regardless of the thickness. The observed Raman peaks are as a result of molecular bond vibrations, that is, vibration mode *E_{og}* and *B_{1g}* peaks which are related to different crystal planes. These observed peaks confirm the presence of anatase phase of TiO₂ thin films (León *et al.*, 2017). All the samples showed a low frequency peak at 143 cm⁻¹ which is a typical O-Ti-O bending and is a characteristic feature of the anatase phase (Raut *et al.*, 2009). It can therefore be deduced that phase transition from amorphous to crystalline occurred during the deposition.

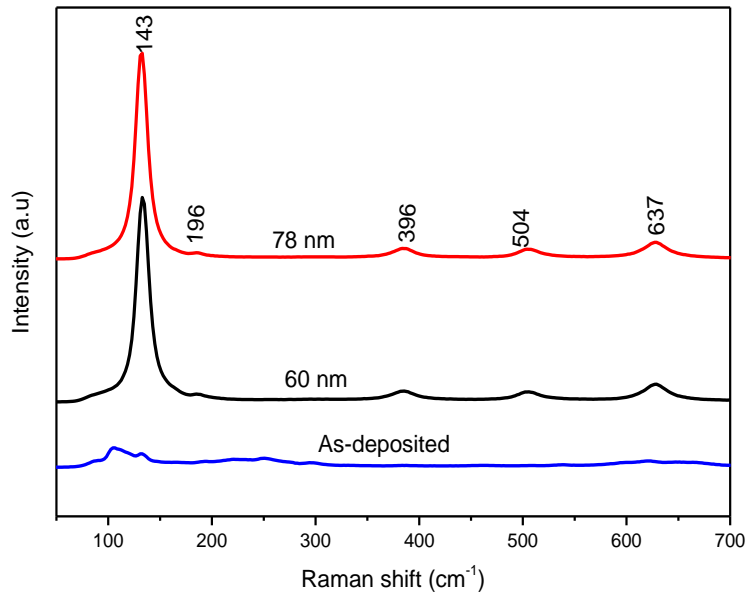


Figure 5. 1: Raman spectra of as-deposited and annealed TiO₂ compact layer of thickness of 60 nm and 78 nm.

These vibrations are as a result of the presence of anatase phase. In this study, it was observed that the peak position of the TiO₂ anatase Raman bands located at around 196 cm⁻¹ at the high frequency side of the E_{og} mode which can also be assigned as the E_{og} mode of anatase phase. Similar observations were reported by León *et al* (2017).

Figure 5.2 shows X-ray diffraction (XRD) pattern of as-deposited and annealed TiO₂ compact layers deposited on FTO substrate at substrate temperature of 200 °C. Peak assignment of the TiO₂ films was done using international center for diffraction data card number 74-1940 (JCPDS). Distinct peaks were observed in all the samples pointing to the nature of crystallinity of the films. The peaks at 27 ° (101), 38 ° (112) and 62 ° (204) obtained in both samples are characteristic crystallographic planes of anatase phase of TiO₂ (Ayieko *et al.*, 2012). As observed, annealed thin films exhibited intense peaks suggesting better crystalline nature and more anatase content in the sample compared to as-deposited thin films.

The spectra for all the samples showed good crystallinity with changes in film thickness showing very little effect on crystallinity. The as-deposited samples also showed good crystallinity with no significance difference with the annealed samples. It can therefore be said that crystallization occurred during the deposition process.

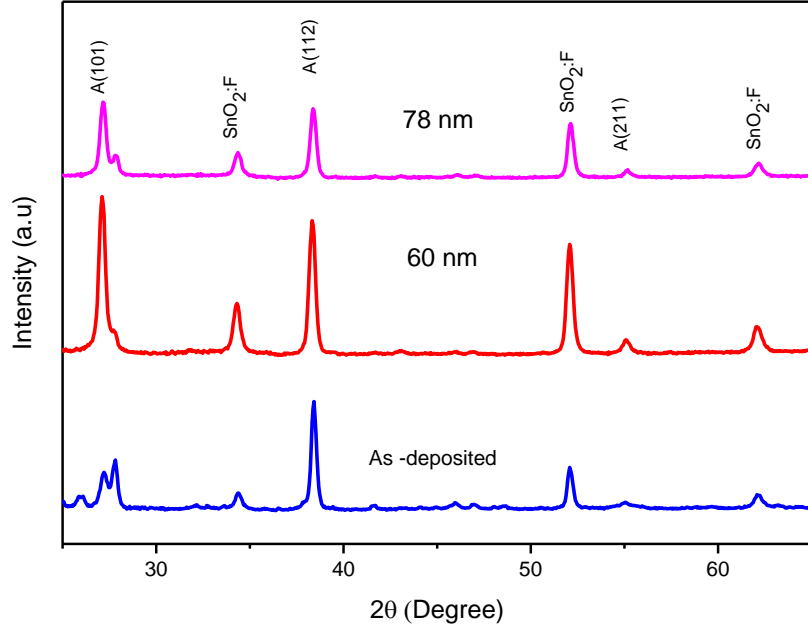


Figure 5. 2: XRD spectra for as-deposited and annealed spray pyrolysis coated TiO₂ layer. The peaks are designated with the reflections of the anatase (A) phase; also indicated are the peaks SnO₂:F substrate.

The grain size, r_{δ} , of TiO₂ thin films was determined using Debye-Scherrer's formula from the full width at half maximum (FWHM) of the diffraction peaks expressed in radians as follows (Arunachalam *et al.*, 2015).

$$r_{\delta} = \frac{k_{sch} \lambda}{\beta \cos \theta} \quad (5.1)$$

where $\lambda = 0.154$ nm is the wavelength of X-ray radiation used, k_{sch} is the Scherrer's constant (shape factor) ranging from 0.9 to 1.0, θ is Bragg diffraction angle of XRD peak and β is the

FWHM measured from the major (101) crystalline plane. Figure 5.3 shows the Gaussian fit for the major (101) peaks performed using Origin software.

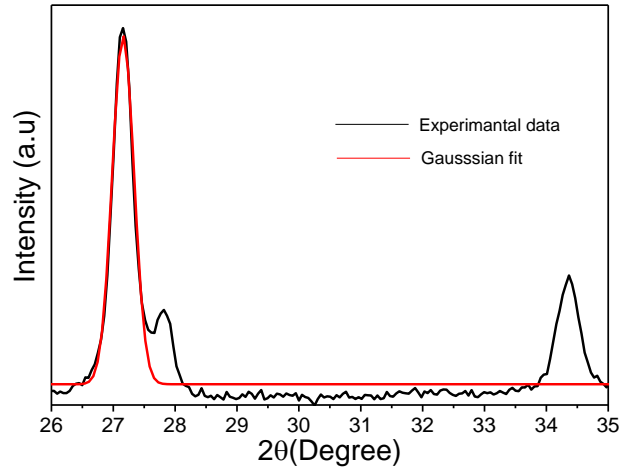


Figure 5. 3: Gaussian fit for (101) peaks used for the determination of full width at half maximum (FWHM).

The grain size obtained was 18.59 nm and 19.76 nm for as-deposited and annealed thin films respectively. Increase in crystal size was observed for annealed thin films. Annealing results into reduction of surface energy which is a driving force for grain boundary enlargement and consequently leading to increase in particle size. It also facilitates the movement of atoms or molecules through the mechanism of mass transport that may be lattice diffusion or surface diffusion resulting into grain growth (Sönmezoğlu *et al.*, 2012).

Additionally, to get more information about the amount of defects in the films, the defects related to grain boundary density was determined using equation (5.2). Defect density σ in the films is given as the reciprocal of the square of grain size and it is estimated from the following relation using simple approach of (Williamson and Smallman, 1956).

$$\sigma = \frac{1}{r_{\delta}^2} \quad (5.2)$$

The defect density obtained was $2.89 \times 10^{-2} \text{ \AA}^{-2}$ and $2.56 \times 10^{-2} \text{ \AA}^{-2}$ for as-deposited TiO_2 compact layer and annealed TiO_2 compact layer respectively. It is seen that the defect density of TiO_2 compact layer decrease with annealing thereby improving the crystallinity of the film (Kose *et al.*, 2009).

Figure 5.4 shows the XRD patterns for $\text{TiO}_2/\text{Nb}_2\text{O}_5$ composite film and TiO_2 porous layer deposited on FTO glass substrate by screen-printing technique. Niobium peaks observed in the diffractograms was assigned using JCPDS card number 28-0317. Crystalline phases of both TiO_2 and Nb_2O_5 corresponding to diffraction peaks 27.33° (101), 38.53° (112) 62.22° (204) and 46.09° (002), 55.01° (102) and 56.72° (200) respectively were observed. Most intense peaks for TiO_2 and Nb_2O_5 are observed at $2\theta = (27.33^\circ)$ and $2\theta = (54.94^\circ)$ respectively. As observed, titanium dioxide tends to have more intense peaks compared to niobium (V) oxide.

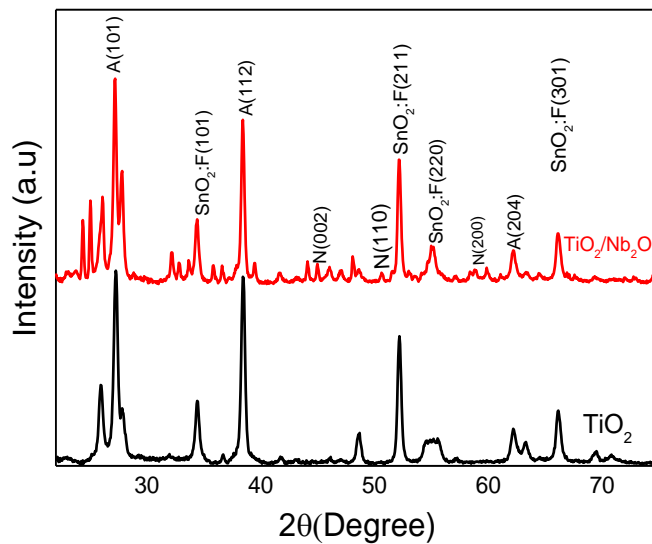


Figure 5. 4: XRD spectra for $\text{TiO}_2/\text{Nb}_2\text{O}_5$ composite layer and pure TiO_2 thin film deposited by screen-printing.

5.3 Energy Dispersive X-ray Fluorescence of TiO₂/Nb₂O₅ Composite Thin Films

Quantitative thin film analysis of the composite with varying ratios of Nb₂O₅ and TiO₂ was achieved using a continuous X-ray beam. Table 5.1 shows various composition in parts per million (PPM) of Nb and Ti contents in the composites as obtained from EDXRF analysis. As observed from the table, as the composition by mass of niobium is increased in the samples so does the parts per million as detected by EDXRF. This is true for concentration by mass of titanium, as the concentration is reduced in the samples so does the values of parts per million.

Table 5. 1: Occurrence of TiO₂ and Nb₂O₅ in parts per million for different ratios

Ratio (in gm) (TiO ₂ :Nb ₂ O ₅)	Ti (PPM)	Nb (PPM)
0.9:0.1	90800	13900
0.8:0.2	50800	29600
0.7:0.3	71000	12300
0.6:0.4	36400	43100
0.4:0.6	8200	29600
0.3:0.7	9920	51500
0.2:0.8	8540	67700
0.1:0.9	11800	123000

Shown in figure (5.5) is the EDXRF spectra for films with 20% Nb₂O₅ and 80% Nb₂O₅ concentration. All the peaks detected in the scan and their corresponding energy shells from different elements are shown. The analysis revealed higher Nb₂O₅ intensity for composite film made of 80% Nb₂O₅ in the composite and a higher TiO₂ intensity for 20% Nb₂O₅ composition in the composite.

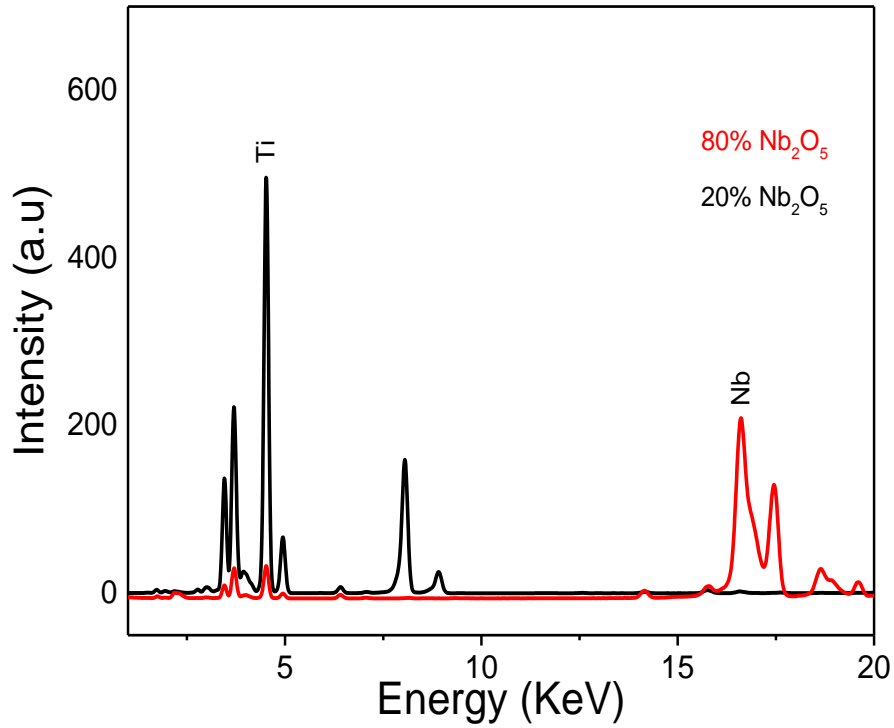


Figure 5. 5: EDXRF energy spectrum of $\text{TiO}_2/\text{Nb}_2\text{O}_5$ composite thin film with 20% and 80% Nb_2O_5 content.

5.4 Optical Characterization

The experimental data for transmittance was obtained directly from *UV – VIS* spectrophotometer (Perkin Elmer Lambda 25) and plotted using Origin Pro 9.1. The effect of annealing and thickness of compact layer on the optical transmittance (T), band gap energy (E_g), refractive index n_f and extinction coefficient k_λ is discussed. Thickness of the films was determined using scout software. Thickness of the films was mainly influenced by three factors, which are; nozzle-substrate distance, the deposition time and annealing as indicated in table 5.2

Table 5. 2: TiO₂ compact layers deposited with varying parameters. Annealing was done at 500 °C for one hour

nozzle-substrate distance	Deposition time	Treatment	Thickness (nm)
100 mm	60 sec	As-deposited	103 nm
100 mm	60 sec	Annealed	96 nm
100 mm	120 sec	As-deposited	125 nm
100 mm	120 sec	Annealed	120 nm
150 mm	60 sec	As-deposited	67 nm
150 mm	60 sec	Annealed	60 nm
150 mm	120 sec	As-deposited	84 nm
150 mm	120 sec	Annealed	78 nm

5.4.1 Effects of annealing and film thickness on optical properties of TiO₂ compact layer

Transmittance spectra for as-deposited and annealed TiO₂ thin layers of different thickness are presented in figure 5.6. A gradual increase in transmittance with increase in wavelength from 350 nm – 600 nm was observed for both as-deposited and annealed films. It was noted that annealed thin films generally exhibited lower transmittance compared to as-deposited thin films. This decrease in transmittance mainly results from light scattering effect which is due to the improved crystallinity of the films (Muaz *et al.*, 2016).

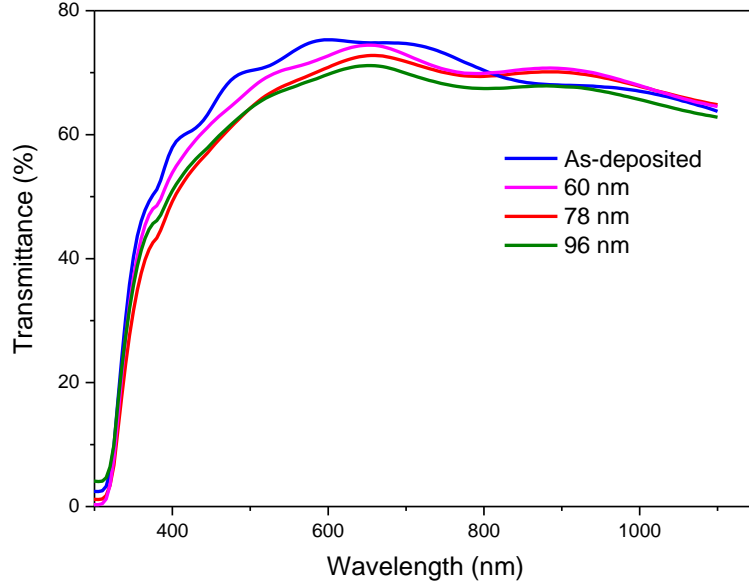


Figure 5. 6: Optical transmittance spectra for as-deposited (67 nm thick) and annealed TiO₂ compact layers of thickness 60 nm, 78 nm and 96 nm deposited by spray pyrolysis technique.

Transmittance (T) is seen to decrease with increase in film thickness. This observation is expected based on Beer-Lambert law equation as shown (Swinehart, 1962);

$$A = -\log_{10} \frac{I}{I_o} \quad (5.3)$$

Where A is the absorbance, I_o is the incident intensity and I the transmitted intensity.

Due to regular arrangement of the particles and the large surface area, TiO₂ compact layer might favor more interfacial contacts with the porous TiO₂/Nb₂O₅. These characteristics make TiO₂ compact layer deposited at substrate- nozzle distance of 150 mm with deposition duration of 60 seconds suitable for use as blocking layer. Longer deposition duration leads to more number of TiO₂ nanoparticles deposited on the substrate leading to increased film thickness, and as such, the optical transmittance decreases. The pores observed in films deposited with nozzle-substrate distance of 100 mm, figure (5.7) support optical and electrical behavior of these films. These

pores were responsible for the increased scattering in the thin films which is a factor responsible for the decrease in transmittance.

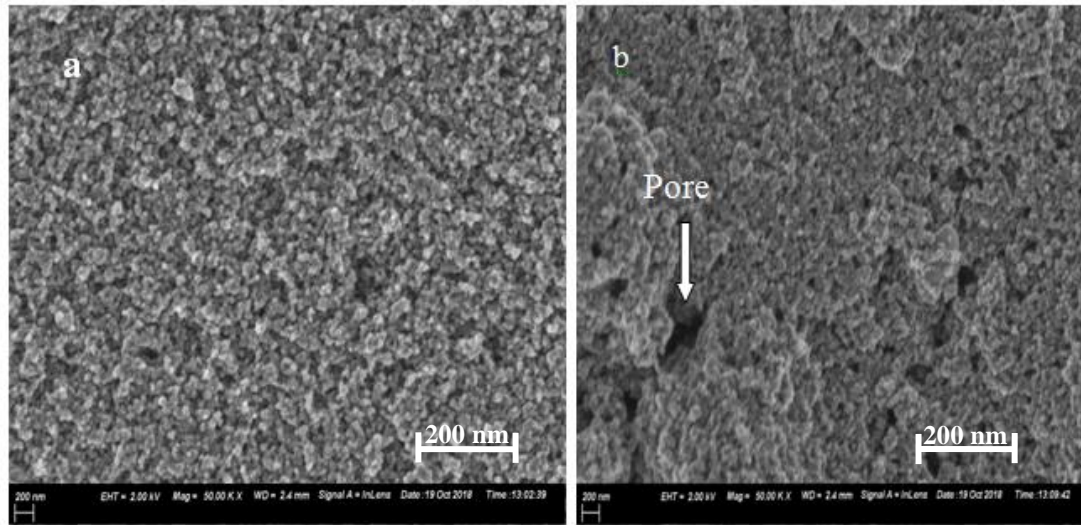


Figure 5. 7: SEM micrograph of annealed TiO₂ compact layer of thickness 60 nm and 96 nm deposited by spray pyrolysis with nozzle-substrate distance of (a) 150 mm and (b) 100 mm deposited for 60 seconds respectively.

5.5 SCOUT Modeling

Using Drude and OJL models described in section 3.2.1 and 3.2.2 respectively of chapter 3 and considering the configuration of the semiconductor/ substrate system, a best fit was obtained with ± 0.5 percent errors between the experimental point and the calculated transmittance. The successful fitting processes of the deposited films are in good agreement between the measured and calculated spectra as shown in figure 5.8.

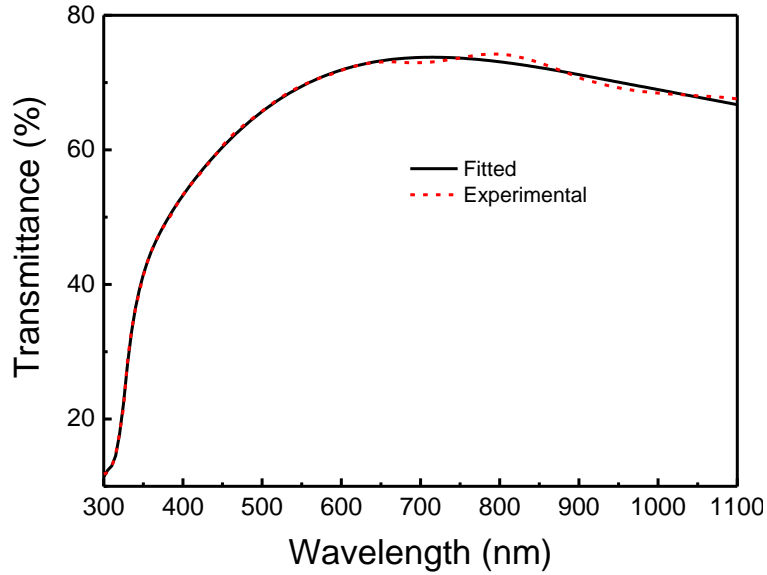


Figure 5. 8: Optical transmittance spectra for fitted and experimental data using SCOUT software based on Drude and OJL models

5.5.1 Effects of annealing on band gap energy of TiO₂ compact layer

The band gap energy (E_g) was obtained by plotting $(\alpha hv)^2$ against hv based on Tauc equation, equation (3.3) in Chapter 3. Band gap energy was obtained by extrapolation of the target to the linear part of $(\alpha hv)^2$ vs hv curve where the intercept to hv gives the band gap energy. In principle, the band gap value strongly depends on crystal structure, morphology, and chemical composition of a given material (Rabeh *et al.*, 2014).

Figure 5.9 shows the band gap energy for as-deposited and annealed TiO₂ compact layer. It is worth noticing that as-deposited films are characterized by high optical energy gap value of 3.7 eV. Annealing the thin films at 500 °C for one hour improves the crystallinity thereby decreasing the band gap energy to a value of 3.6 eV.

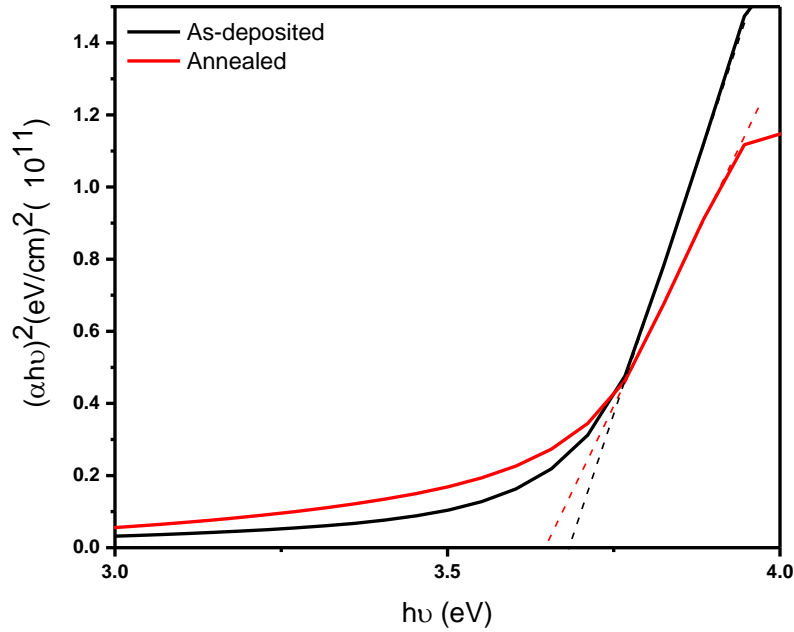


Figure 5. 9: Band gap energy for as-deposited (67 nm) and annealed TiO₂ thin film (60 nm) deposited at nozzle-substrate distance of 150 nm and for 60 seconds deposition time.

Annealing leads to improved crystallinity as supported by the XRD in figure 5.2. A change in optical band gap is given by the following equation (Agbo *et al.*, 2012);

$$\Delta E_g = \frac{\hbar^2 v^2}{2r_\delta^2} \left(\frac{1}{M_e} + \frac{1}{M_h} \right) - \frac{(1.76e^2)}{\epsilon_\chi r_\delta} \quad (5.4)$$

Where M_c , M_h are the effective masses of electrons in the conduction band and holes in the valence band respectively and ϵ_χ is the static dielectric constant of the material. The first term represents the particle in a box quantum localization energy and has an inverse square relation

$\frac{1}{r_\delta^2}$ dependence where r_δ is the grain size, while the second term represents the Coulomb

energy with $\frac{1}{r_\delta}$ dependence. Therefore as r_δ increases due to increase in grain growth due to annealing, the value of ΔE_g decrease (the crystallite size obtained was 18.59 nm and 19.76 nm for as-deposited and annealed thin films respectively). (Nandani *et al.*, 2018) reported similar observation.

5.5.2 Effect of film thickness on band gap energy E_g of TiO₂ compact layer

To understand the effect of film thickness of TiO₂ compact layer on the band gap energy, the deposition duration and nozzle-substrate distance were varied during the formation of compact layers. Figure 5.10 show the effect of film thickness on the band gap energy of annealed thin films. Decrease in the optical band gap with increase in film thickness is observed.

As the film thickness increases, the film begins to behave like a bulk material. In bulk materials, the crystallinity is enhanced, the defect states are decreased and the atoms become well packed as well as the crystallites get agglomerated. This indicates that the band gap value is influenced by the film thickness.

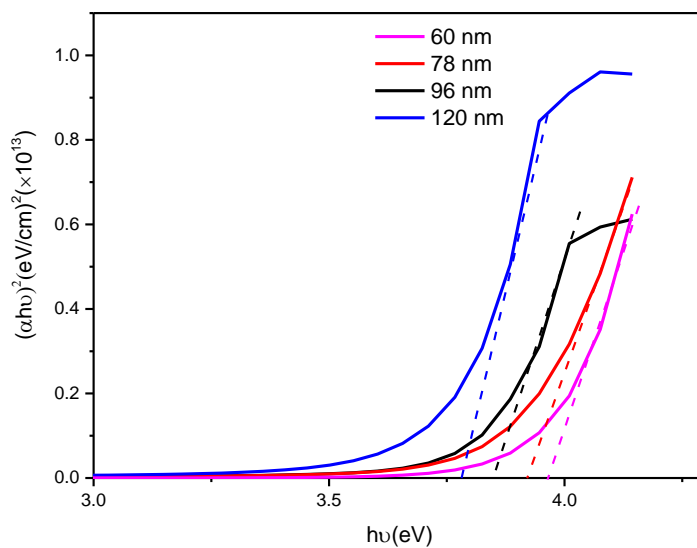


Figure 5.10: Band gap energy for annealed TiO₂ thin films with varying thickness.

These results suggest that the optical band gap of TiO₂ compact layer film could be controlled more precisely by controlling the thickness of the film. Thickness of the film causes a shift in the optical absorption edge. For bulk materials, the band gap energy (E_g) is constant. However, for thin crystalline films it varies with thickness due to the changes in barrier height at grain boundaries with increasing film thickness. This is due to increase in localized density of states near the edges and in turn decreases the value of E_g with increase in film thickness (Alya and Akla, 2015). Equation (5.5) was used to explain and verify the band gap reduction with increase in film thickness (Goh *et al.*, 2010).

$$\Delta E_g = \frac{\hbar^2}{2md^2} \quad (5.5)$$

where d is the thickness of the film and m is the effective carrier mass

5.5.3 Effects of annealing on Refractive index of TiO₂ compact layer

In the O'Leary-Johnson-Lim (OJL) model, refractive index n_f , as a function of energy is determined mainly by the parameter 'mass' which determines the shape of the conduction band (Solieman and Abu-Sehly, 2010). Figure 5.11 shows the variation of the refractive index with wavelength for as-deposited and annealed TiO₂ thin films. It is observed that the refractive index (n_f) is high for the annealed samples. This is because annealing causes decrease in porosity and structural transformation to crystalline anatase, which leads to increase in the refractive index of the film (Aksay and Altiookka, 2007).

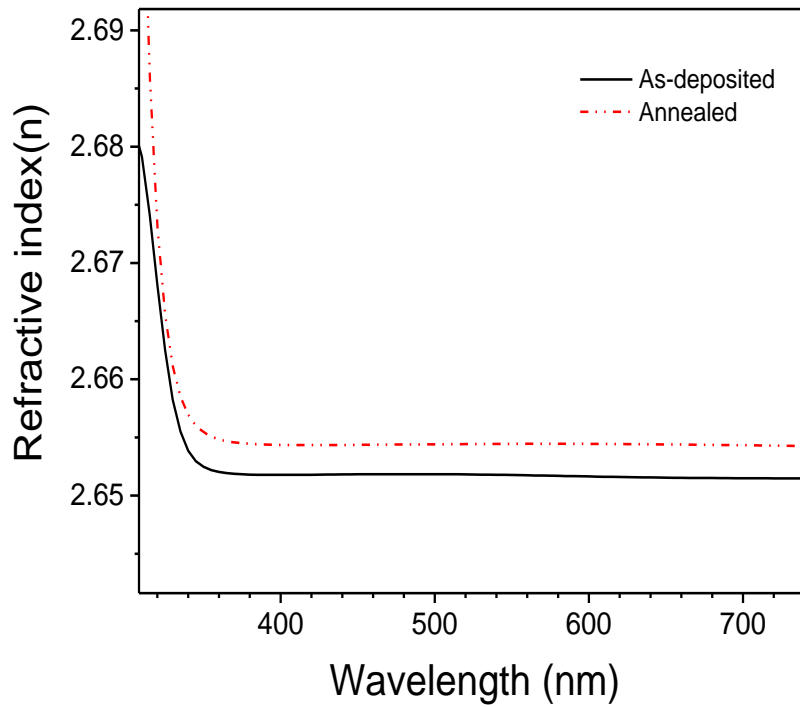


Figure 5.11: Refractive index n_f of as-deposited and annealed TiO₂ films of thickness 67 nm and 60 nm respectively.

5.6 Refractive Index n_f and Porosity P

The refractive index of a thin film often differs from that of bulk material where thin films show lower values whereas the refractive index of thicker films approaches the bulk value. Within the film, it is convenient to use the concept of the porosity (P) which is defined to be the ratio of the average film density (p_f) and the bulk density (p_m)

$$p = \frac{p_f}{p_m} \quad (5.6)$$

The dependence of refractive index on the film porosity could be easily explained by well-known Lorentz-Lorenz relation (Pulker, 1979)

$$P = \frac{\rho_f}{\rho_m} = \left(1 - \frac{n_f^2 - 1}{n_f^2 + 2} \cdot \frac{n_m^2 + 2}{n_m^2 - 1}\right) \quad (5.7)$$

Where n_m is the refractive index of pore-free anatase TiO₂ and n_f is the refractive index of TiO₂ compact layer film deposited by spray pyrolysis. The refractive index of dense anatase TiO₂ is 2.46 (Asahi *et al.*, 2000). Using equation (5.7) and the value of refractive index obtained for the films, the porosity of 60 nm thick layer was found to be 18.26 % while that of 96 nm thick TiO₂ layer was 12.89 % respectively.

5.6.1 Effects of annealing on extinction coefficient (k_λ) of TiO₂ compact layer

Figure 5.12 illustrates the extinction coefficient k_λ as a function of wavelength for as-deposited and annealed TiO₂ blocking layers. It is observed that the extinction coefficient k_λ was generally higher for the annealed samples. This increase in extinction coefficient is attributed to decrease in the band gap energy when the film is annealed (Eiamchai *et al.*, 2009).

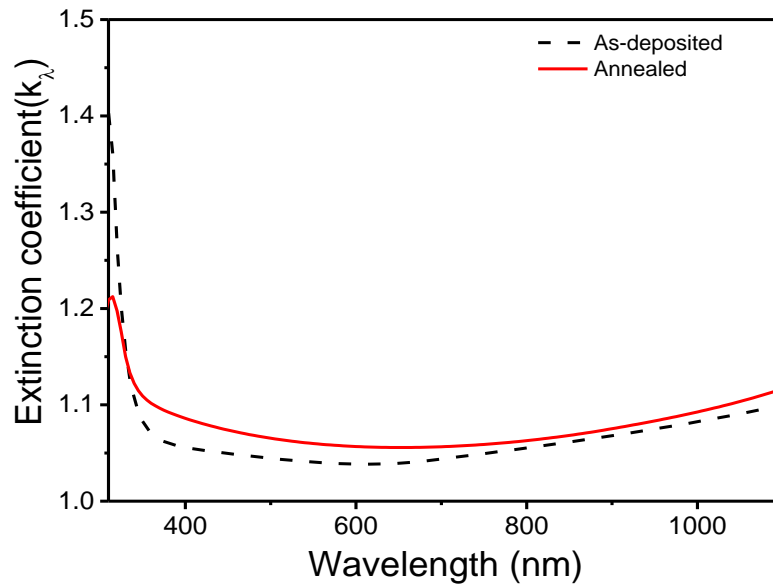


Figure 5.12: Extinction coefficient k_λ for as-deposited and annealed TiO₂ films of thickness 67 nm and 60 nm respectively.

5.6.2 Effects of film thickness on extinction coefficient k_λ of TiO₂ compact layer

Figure 5.13 shows extinction coefficient k_λ against wavelength curves for TiO₂ compact layer with varying thickness. A decrease in extinction coefficient with increase in film thickness is observed. This can be explained using the relationship shown in equation (5.8) (Ilican *et al.*, 2007)

$$k_\lambda = \frac{\alpha\lambda}{4\pi d} \quad (5.8)$$

Where d is the film thickness

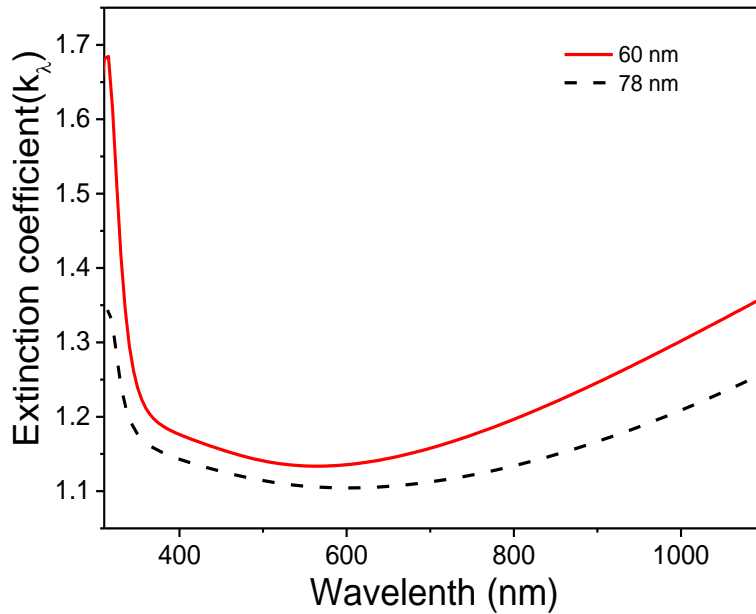


Figure 5.13: Extinction coefficient k_λ , for annealed TiO₂ films of thickness 60 nm and 78 nm.

5.7 Electrical Characterization of TiO₂ Compact Layer

5.7.1 Influence of annealing on electrical properties of TiO₂ compact layer

Table 5.3 shows the values for the obtained sheet resistance of the films, charge carrier concentration n_α for different samples. The results indicate that the sheet resistance of the

samples decreases on annealing. Since TiO₂ is an n-type semiconductor, the concentration of Ti⁴⁺ in the TiO₂ films form a donor level between the band gap of TiO₂ which results in the reduction of recombination of photogenerated electron and holes (Zhao *et al.*, 2008). Presence of O²⁻ ions results in an increase in the free electron concentration leading to decrease in film sheet resistance (Malati and Wong, 1984).

Table 5. 3: Influence of annealing on electrical properties of TiO₂ compact layer.

TiO ₂ compact Layer	Sheet resistance ($\times 10^2 \Omega\text{cm}$) (Experimental)	Sheet resistance ($\times 10^2 \Omega\text{cm}$) (Simulated)	Carrier concentration ($\times 10^{22} \text{cm}^{-3}$)
As-deposited	6.86	6.44	3.74
Annealed	4.86	4.55	3.5

Increase in conductivity upon annealing can as well be explained as follows; annealing results into reduction of surface energy which is a driving force for grain boundary enlargement facilitating electron mobility in the films and hence decrease in sheet resistivity (Biju and Jain, 2008). The carrier concentration is also seen to decrease on annealing of the thin films. Electrical carrier concentration n_a in the TiO₂ compact layers is seen to be very high and keeps within the order of magnitude of $10^{22}/\text{cm}^3$.

5.7.2 Effect of film thickness on electrical properties of TiO₂ compact layer

Table 5.4 shows the dependence of sheet resistivity and carrier concentration on the thickness of TiO₂ compact layer. It is observed that films with thickness 60 nm exhibited the lowest sheet resistivity of $1.33 \times 10^2 \Omega\text{cm}$. However, as the thickness increased, the sheet resistivity of the films increased since it is inversely proportional to carrier concentration (Myoung *et al.*, 2002).

The resistivity (ρ) of the thin films is proportional to the reciprocal of the product of free carrier concentration n and the mobility (μ) as shown in the following relation;

$$\rho = \frac{1}{en\mu} \quad (5.9)$$

Table 5. 4: Influence of film thickness on electrical properties of TiO₂ compact layer

TiO ₂ compact layer thickness	Sheet resistance ($\times 10^2 \Omega \text{cm}$) (Experimental)	Sheet resistance ($\times 10^2 \Omega \text{cm}$) (Simulated)	Carrier concentration ($\times 10^{22} \text{cm}^{-3}$)
60 nm	1.23	1.33	5.58
78 nm	3.14	3.83	4.15
96 nm	4.86	4.55	3.50
120 nm	5.41	5.00	2.63

5.8 Optical Characterization of TiO₂/Nb₂O₅ Composite Thin Films

Variation of peak transmittance with concentration of Nb₂O₅ nanoparticles is shown in figure 5.14. A uniform thickness of 127 nm was maintained for all the composite thin film layers. It was noted that for higher concentrations of Nb₂O₅ absorption of light was enhanced thereby lowering the transmittance of the film. This behavior is an indication of increased charge carrier concentration in the composite as explained by the Drude's theory (Pal *et al.*, 2017).

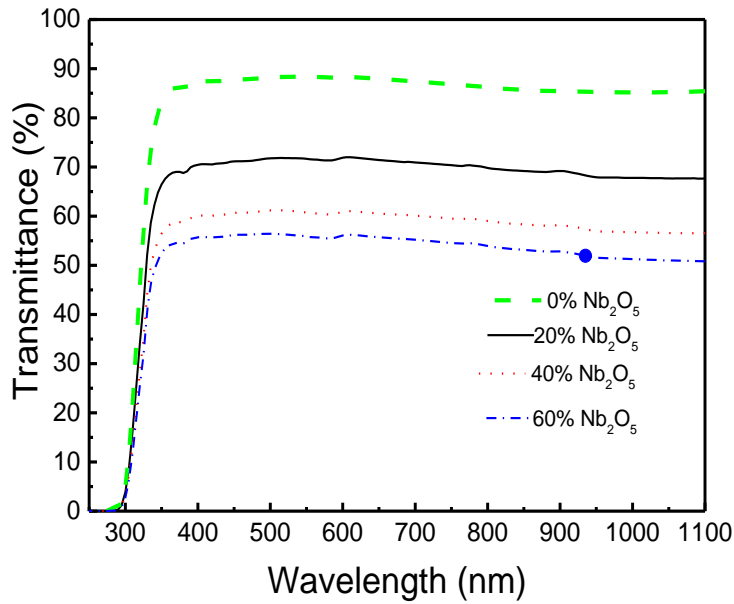


Figure 5.14: Optical transmittance spectra for different composition of Nb₂O₅ in the TiO₂/Nb₂O₅ composite.

The SEM image figure 5.15(a) shows a network of interconnected TiO₂ and Nb₂O₅ nanoparticles formed from the mixture of the powders for TiO₂/Nb₂O₅ composite layer while figure 5.15 (b) shows the SEM micrograph for TiO₂ thin film. From the SEM images, the composite film is porous having a morphology that is favorable for light scattering effect and increases the light optical path, thus enhancing light absorption which makes the film appropriate for solar cells application, thus decrease in transmittance could be due to increased absorption of light as it travelled through the thicker films.

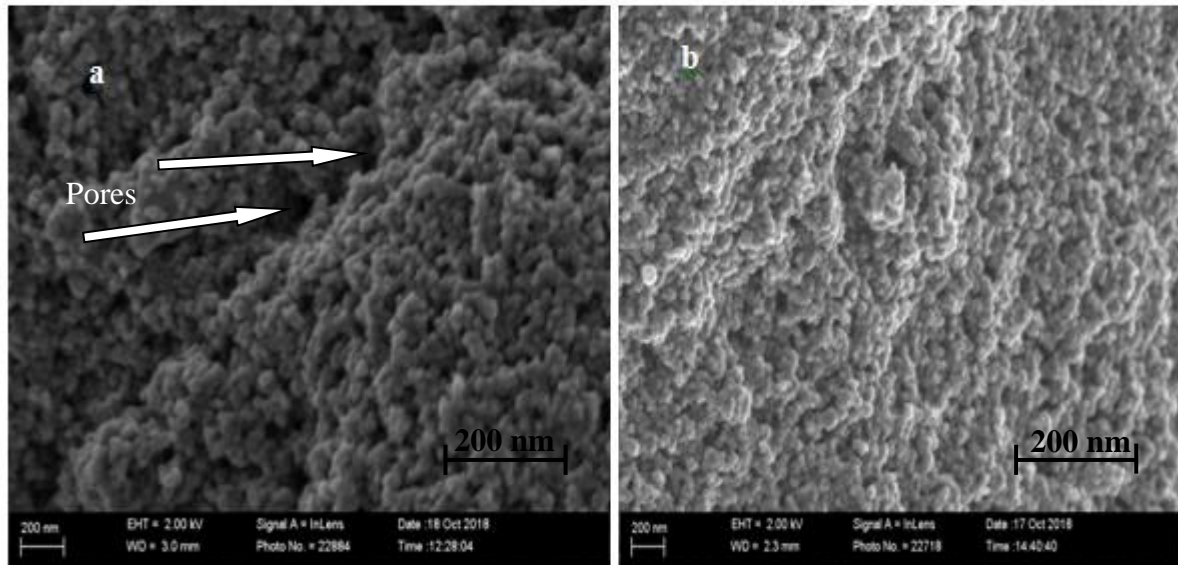


Figure 5.15: SEM micrograph of (a) $\text{TiO}_2/\text{Nb}_2\text{O}_5$ composite and (b) TiO_2 porous layer deposited by screen printing technique.

Figure 5.16 shows a plot of $(\alpha h\nu)^2$ versus $(h\nu)$ for determining the band gap energy. Direct band gap energies for pure TiO_2 , Pure Nb_2O_5 and $\text{TiO}_2/\text{Nb}_2\text{O}_5$ composite were estimated by dropping a tangent to the linear part of the curves and extrapolating it to the intercept the energy $(h\nu)$ -axis. The linear variation of $(\alpha h\nu)^2$ versus $(h\nu)$ at the absorption edge indicates direct transition took place across the band gap of the materials.

The obtained optical band gap energy for pure TiO_2 was found to be 3.90 eV, pure niobium was 3.95 eV and for $\text{TiO}_2/\text{Nb}_2\text{O}_5$ composite was 3.81 eV. These findings are in agreement with the findings of Nguu *et al.* (2014). It follows that the band gap energy obtained experimentally for the composite films was lower than those obtained for pure TiO_2 and pure Nb_2O_5 respectively. This observation could be as a result of development of sub-band states in the composite films (Nguu *et al.*, 2014).

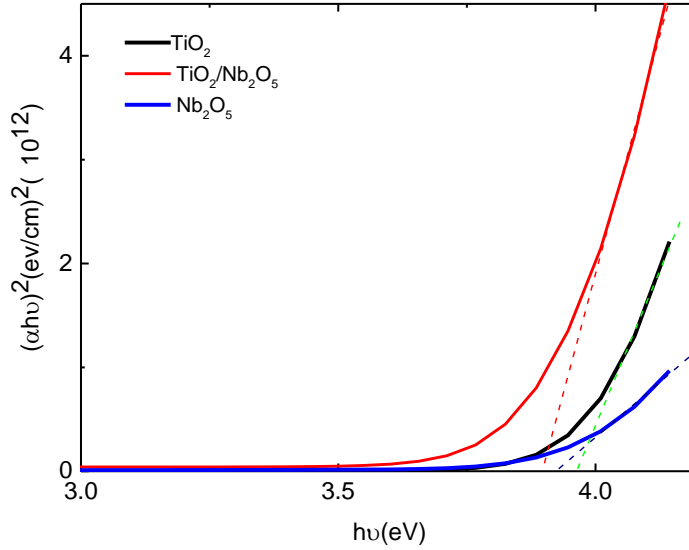


Figure 5.16: Variation of $(\alpha h\nu)^2$ versus photon energy ($h\nu$) for direct band gap transitions in pure TiO_2 , Pure Nb_2O_5 and $\text{TiO}_2/\text{Nb}_2\text{O}_5$ composite

5.9 Current-voltage (I-V) Characteristics

Figure 5.17 shows photocurrent against potential characteristics at 1 sun illumination for $\text{TiO}_2/\text{Nb}_2\text{O}_5$ dye sensitized solar cells with and without TiO_2 compact layer of varying thickness.

Introduction of compact layer had an effect on J_{sc} and V_{oc} hence the conversion efficiency η of the cells. Thin compact layer resulted in higher values of J_{sc} and V_{oc} with the highest value of J_{sc} of 8.16 mA/cm^2 and efficiency of 3.39 % obtained for compact layer of 60 nm. Thick compact layer of 96 nm reported a reduction of J_{sc} to 4.87 mA/cm^2 and 1.29 % efficiency. Comparatively, cells without compact layer had lower J_{sc} of 3.68 mA/cm^2 and efficiency 1.90 %.

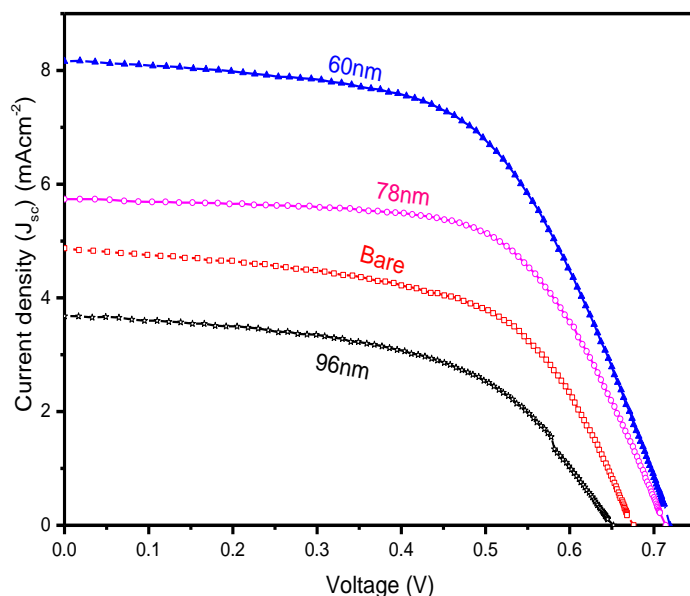


Figure 5.17: I-V characteristic curves for DSSCs with compact layer of different thickness

The improved J_{sc} and efficiency can be explained to be as a result of improved adherence and increased electron pathways and therefore less resistance to electron transfer to the FTO interface (Ito *et al.*, 2008). The compact layer favors the accumulation of electrons at the interface of FTO resulting in an upward shift of electron Fermi level by increasing the electron-carrier concentration (O'Regan *et al.*, 2005). As a result, higher V_{oc} is obtained compared to the bare cell, and the short-circuit current density J_{sc} is also increased. The experimental results we obtained for $\text{TiO}_2/\text{Nb}_2\text{O}_5$ composite layer without a compact layer are similar those obtained by Jose *et al.* (2009) and Nguu *et al.* (2014). Introduction of compact layer enhanced the photo-conversion efficiency of the cells.

Decrease in conversion efficiency was observed for thicker compact layer (96 nm). One possible reason is that more trap states exist in the thicker TiO_2 compact layer which tend to block the pathway of photo excited electrons from the nanoporous $\text{TiO}_2/\text{Nb}_2\text{O}_5$ layer to the FTO electrode

(Zhang *et al.*, 2005). Furthermore, the thicker TiO₂ compact layer lowers optical transmittance, thereby reducing both J_{sc} and V_{oc} .

The series resistance R_s and shunt resistance R_{sh} values of the device are presented in Table 5.5. As is well-known from the equivalent circuit model, R_{sh} relates to the interface recombination in the cells. Thus a higher R_{sh} corresponds to the suppression of charge recombination inside the cells, which in turn results in a higher V_{oc} . Series resistance in the cells is associated with charge transfer at Pt-counter electrode, FTO substrate resistance and the Nernst diffusion in the electrolyte (Yang *et al.*, 2012). With introduction of compact layer, decrease in series resistance was observed which to increase in fill factor. This was as a result of electron permeating into the compact layer which then blocks its recombination. However, for very thick compact layers, an increase in series resistance of the cells was noticed. This could be as a result of existence of more trap states in the thick layers hindering the electron transfer at the Pt counter electrode. Compact layers of thickness less than 50 nm could not be achieved experimentally due to the employed deposition technique and instruments limitations. It is important to note the conversion efficiency of the solar cells having 60 nm thick TiO₂ blocking layer displays a decent photovoltaic performance comparable to those reported in literature (Supasai *et al.*, 2016; Concina and Vomiero, 2015). It is worth noticing that there is deterioration in photovoltaic parameters with increase in compact layer thickness.

Table 5.5: I-V characteristics for DSSC with compact layers of varying thickness

TiO ₂ compact layer Thickness with 127 nm thick porous layer	J_{sc} (mA/cm ²)	V (V)	R_{sh} ($\times 10^3 \Omega$)	R_s (Ω)	FF	η (%)
60 nm	8.16	0.72	8.50	34.85	0.58	3.39
78 nm	5.74	0.71	4.81	40.57	0.63	2.58
96 nm	3.68	0.65	2.46	79.84	0.54	1.29
Bare	4.87	0.67	1.48	52.55	0.58	1.90

The photovoltaic parameters, open circuit voltage V_{oc} , short circuit current density J_{sc} , fill factor (FF) and the conversion efficiency (η) were obtained from the J - V characteristic curves together with the following equations.

$$FF = \frac{P_{max}}{P_{in}} = \frac{J_{max} \cdot V_{max}}{J_{sc} \cdot V_{oc}} \quad (5.11)$$

$$\eta = \frac{J_{sc} V_{oc} FF}{P_{in}} \quad (5.12)$$

Where V_{max} is the maximum voltage, J_{max} is the maximum current density (mA/cm²) and p_{in} incident light intensity (mW/cm²).

From figure 5.18 gives a summary of various cells parameter with varying thickness. It was observed that for DSSCs with thicker compact layers, the photovoltaic parameters deteriorate.

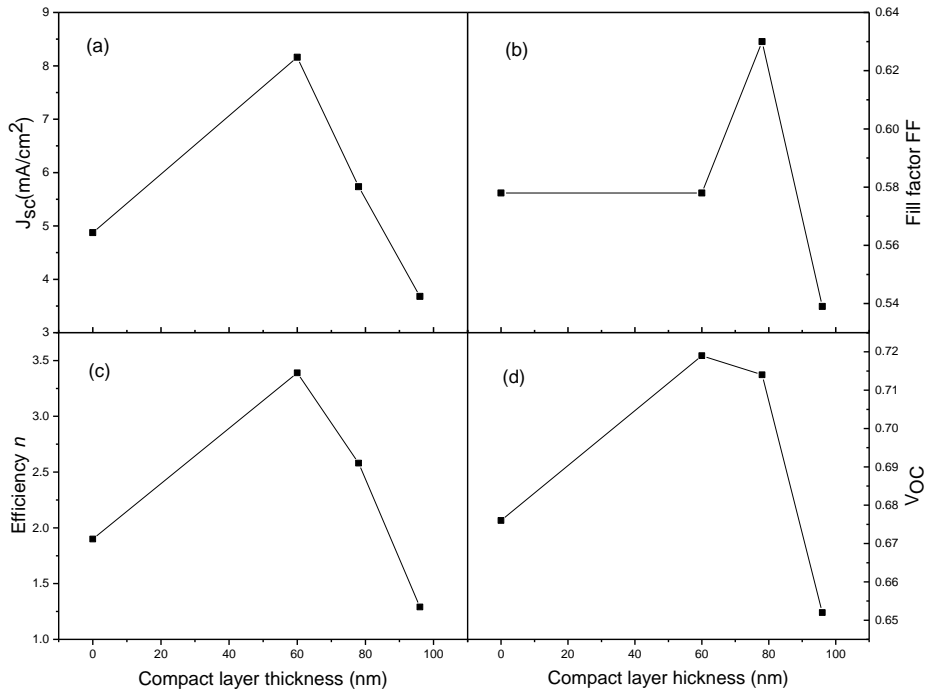


Figure 5.18: Variation of photovoltaic parameters of dye sensitized solar cells with varying TiO₂ compact layer thickness (a) current density J_{sc} (mA/cm²), (b) Fill factor FF, (c) Efficiency η and (d) Open circuit voltage V_{OC}.

5.10 Electrochemical impedance spectroscopy

To gain further insight into the interfacial charge transport in the fabricated DSSCs, electrochemical impedance spectroscopy was performed. Figure 5.19 shows the Nyquist plots of solar cells based on different TiO₂ compact layer thickness and zoom of Nyquist plots at high frequency region. The spectra obtained are characterized by major RC arc and some additional minor features in the high frequency region. The semicircles are almost perfect but at high frequency there is a small additional arc which is due to the internal resistance of the solar cells. The high frequency arc (Zoomed) is attributed to the redox reaction at the platinum counter

electrode while the larger arc is as a result of reactions at the metal oxide semiconductor/electrolyte interface (Basu *et al.*, 2016).

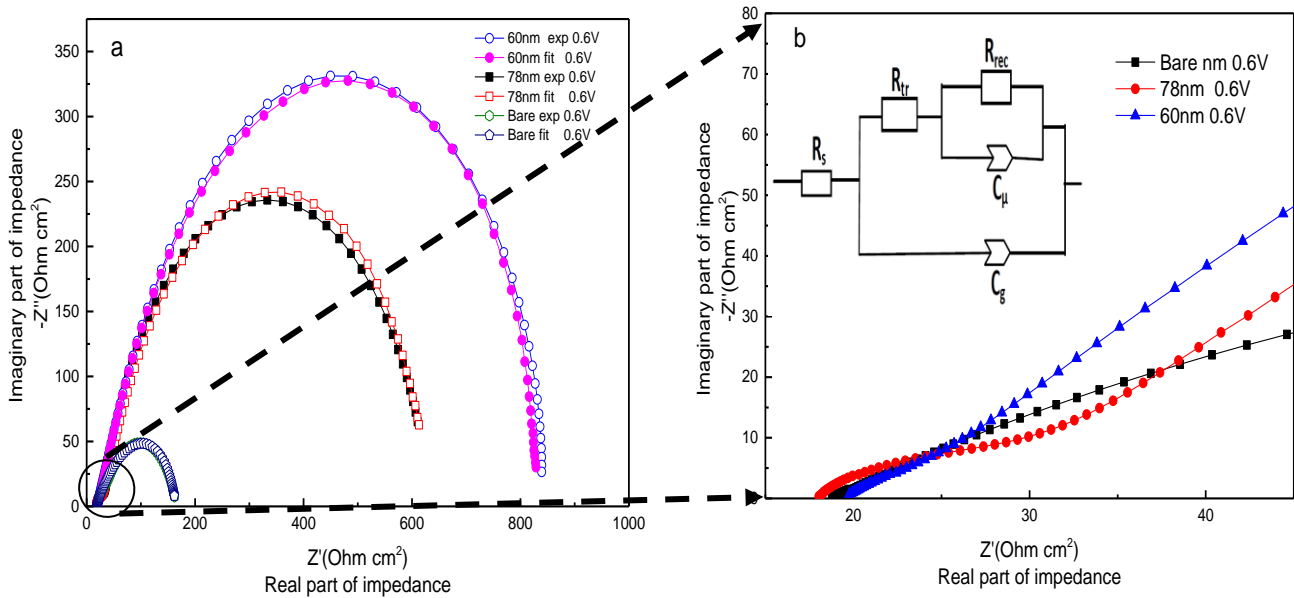


Figure 5.19: (a) Nyquist plot based on TiO₂ compact layer with varying thickness at bias potential 0.60 V, (b) Zoom of Nyquist plot in the high frequency region, (inset) Equivalent circuit used to fit EIS data.

The high frequency part contain information of transport and series resistance element as well as the dielectric contributions while the arc at low frequencies is attributed to recombination resistance (R_{rec}) and chemical capacitance (C_{μ}) of the device (Garcia-Belmonte *et al.*, 2008).

The arc observed at mid-frequency accounts for electron diffusion in the TiO₂ layer, and a RC element (R-resistor C-capacitor) where recombination resistance and chemical capacitance are expressed as

$$\begin{aligned}
R_{rec} &= R_o \exp\left(\beta \frac{eV}{k_B T}\right) \\
C_\mu &= C_o \exp\left(\alpha \frac{eV}{k_B T}\right)
\end{aligned}
\tag{5.13}$$

Where C_o and R_o are constants, e is the elementary charge, k_B is Boltzmann's constant, T is the absolute temperature, β and α are dimensionless parameters and V is the voltage.

The recombination resistance R_{rec} produces a rather direct view of the recombination process in the cells. It is attributed to the processes in the TiO_2 /electrolyte interface. The second arc is evidently large for the solar cells with TiO_2 compact layer indicating that the compact layer increases R_{rec} thus lowering the recombination processes at the oxide/electrode interface leading to a larger V_{oc} (Góes *et al.*, 2012). Introduction of blocking layer of desired thickness increases the electron lifetime τ by suppressing recombination at the FTO/electrolyte interface (Yoo *et al.*, 2010). The longest lifetime is obtained from DSSC with 60 nm thick TiO_2 compact layer. This is the optimum thickness at which the cells exhibit the highest conversion efficiency.

Chemical capacitance C_μ accounts for accumulation of electrons in the localized states located in the TiO_2 and Nb_2O_5 band gaps (Todinova *et al.*, 2015). It measures the capability of a system to accept or release additional electrons due to variation of its Fermi level.

Transport resistance R_r corresponds to electron diffusion through the $\text{TiO}_2/\text{Nb}_2\text{O}_5$. For thicker compact layer, increase in R_r is observed. This is because of existence of more trap states which block the movement of photo-generated electrons. The trend in series resistance R_s for DSSC with TiO_2 compact layer is smaller than that of bare DSSC which is consistent with the results

obtained from $J-V$ curves. In both cases DSSC fabricated using 60 nm thick compact layer showing the lowest series resistance while bare cells shows the highest series resistance. The measured values of recombination resistance R_{rec} , transport resistance R_{tr} , electron lifetime τ , geometrical capacitance C_g , chemical capacitance C_μ and series resistance R_s are shown in Table 5.7

Table 5.6: Values of recombination resistance R_{tr} , chemical capacitance C_μ , transport resistance R_{tr} , geometrical capacitance C_g , series resistance R_s and electron lifetime τ obtained from the fabricated solar cells.

TiO ₂ compact layer thickness with 127 nm thick TiO ₂ /Nb ₂ O ₅ porous layer	R_{rec} Ohm.cm ²	C_μ ($\times 10^{-6}$ F/cm ²)	R_{tr} Ohm.cm ²	C_g ($\times 10^6$ F/cm ²)	R_s Ohm.cm ²	τ ($\times 10^{-4}$ s)
60 nm	899.36	43.00	453	8.82	10	386.90
78 nm	333.20	27.50	27	62.10	16	91.50
Bare	54.91	4.60	12	81.20	21	2.50

Nyquist plots at different bias voltages varied between 0.5 - 0.70V were also analyzed. Figure 5.20 shows the Nyquist plot at different bias voltages. It was noted that the diameter of the semicircles reduce with increase in bias voltage due to the sinking recombination resistance which is dependent on recombination current.

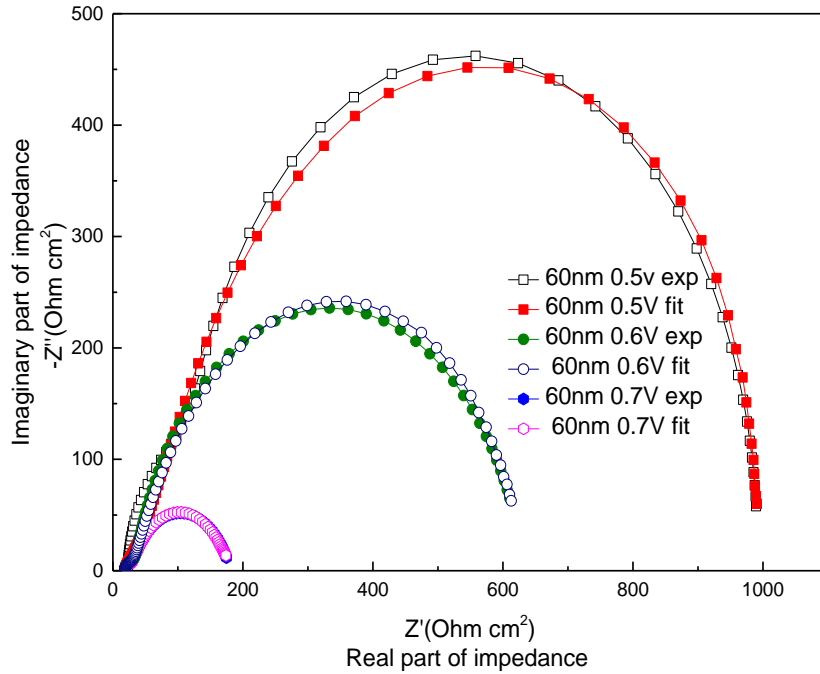


Figure 5.20: Impedance spectra for 60 nm TiO₂ compact layer solar cell at different bias voltages

Increase in bias voltage leads to decrease in resistance. This led to arc at high frequencies to become more pronounced and can be assigned to a fast diffusion of electrons through the TiO₂ compact layers. Recombination resistance decreases from 401 Ωcm^2 at 0.5 V to 85 Ωcm^2 at 0.7 V. R_{rec} is dependent on the voltage due to the increased charge carrier densities while the chemical capacitance rises exponentially with increase in bias voltage since it has a direct dependence on the charge carrier densities (Leever *et al.*, 2012). Figure 5.21 shows a plot of parameters in equivalent circuit against bias voltage for the best performing solar cell.

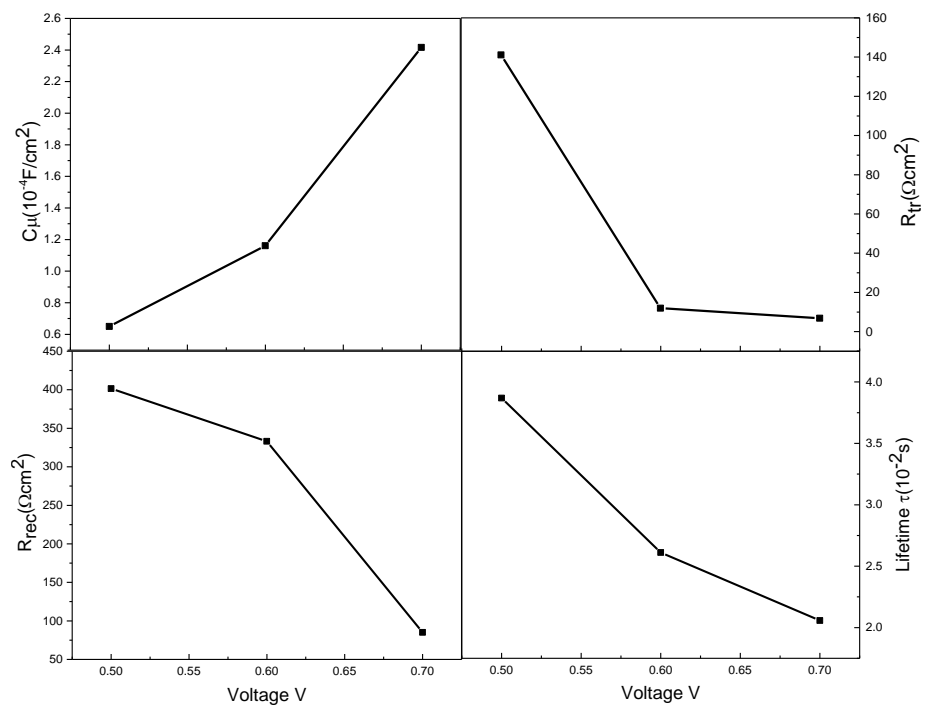


Figure 5.21: Impedance spectroscopy measurements of the best performing DSSCs with TiO_2 compact layer of 60 nm thickness.

CHAPTER SIX

CONCLUSION AND RECOMMENDATIONS

6.1 Conclusion

This project was aimed at developing blocking layer based on titanium dioxide and studying its effect on the photovoltaic characteristics of TiO₂/Nb₂O₅ composite dye sensitized solar cell. In this study, investigation on the deposition of TiO₂ blocking layer by spray pyrolysis technique was successfully performed to determine the correlation between the deposition conditions and the electrical properties of the grown thin films. We demonstrated that the thickness of the films is determined by deposition time and varying the deposition distance between the substrate and the spray nozzle. It was noted that the electrical resistivity of the deposited TiO₂ compact layers can be manipulated by annealing the films to 500 °C.

Optical, morphological and structural properties of films were performed by UV-VIS spectrophotometer, scanning electron microscope, Raman spectroscopy and X-ray diffraction respectively. Characterization of the optical properties of the films revealed the dependence of transmittance of the films to thickness. XRD results obtained in this work indicated that changes in electrical resistivity of the films are associated to the structural changes where annealed films showed to be highly crystalline thereby lowering the resistivity of the films.

From current density- voltage (J-V) characteristics of the assembled cells, it can be concluded that current-voltage characteristics of the cell are affected by introduction of a blocking layer where a cell incorporating 60 nm thick compact layer exhibiting the highest efficiency of 3.39 % with current density $J_{sc} = 8.16 \text{ mA/cm}^2$, open circuit voltage $V_{oc} = 0.719\text{V}$ and fill factor $FF = 0.578$.

In comparison, a cell without compact layer showed relatively low efficiency η of 1.90, short circuit current $J_{sc}=4.84$ mA/cm², open circuit voltage $V_{oc}=0.676$ V and fill factor FF equals to 0.578.

Electrochemical impedance spectroscopy analysis was performed to extract the parameters corresponding to fundamental electronic and ionic processes in the cells. Nyquist plots were obtained at bias voltage of 0.6 V and the spectra fitted to an appropriate equivalent circuit to extract key parameters; recombination resistance R_{rec} , series resistance R_s , Transport resistance R_{tr} , lifetime τ and chemical capacitance C_{μ} . The study revealed that introduction of TiO₂ compact layer increased recombination resistance in the cells leading to improved V_{oc} . For the best performing cell, recombination resistance R_{rec} was 899.36 Ohm.cm², chemical capacitance $C_{\mu}=4.3\times 10^{-5}$ Fcm⁻², transport resistance R_{tr} 4.53×10^2 Ohm.cm², geometrical capacitance $C_g=8.82\times 10^{-6}$ Fcm⁻² and recombination resistance $R_s=10$ ohm.cm². Charge carrier life time of the solar cells were also determined with the best performing solar cell having charge carrier lifetime of 3.86×10^{-2} s while charge carrier lifetime for solar cell showing lowest efficiency to be 2.50×10^{-4} s. From the study, was noted that TiO₂ compact layer improved the performance of dye sensitized solar cells due to improved open circuit voltage and fill factor while for very thick compact layer, the efficiency dropped.

6.2 Recommendations

The study of effects of TiO₂ compact layer on PV characteristics of Nb₂O₅ composite solar cells still remains at fundamental levels. For future research, there is need to study the effect of varying precursor concentration on the optical and electrical properties of TiO₂ compact layer. Further, it is recommended that effects of thickness of TiO₂/Nb₂O₅ composite layer on the conversion efficiency of solar cells be studied.

References

- Abdul, R., Zoolfakar, A. S., Subbiah, J., Ou, J. Z., and Kalantar-zadeh, K. (2014). Highly Ordered Anodized Nb₂O₅ Nanochannels for Dye-Sensitized Solar Cells. *Electrochem. Commun.* **40**, 20–23.
- Agbo, P. E., Nnabuchi, M. N., and Onogu, K. O. (2012). Effect of Annealing on the Thickness and Band Gap of Novel Core-Shell Crystalline Thin Film. *J. Ovonic Res.* **8**, 127–134.
- Aksay, S. and Altiokka, B. (2007). Effect of Substrate Temperature on Some of the Optical Parameters of CuInS₂ Films. *Phys. Status Solidi C* **4**, 585–588.
- Al-Juaid, F., Merazga, A., Abdel-Wahab, F., and Al-Amoudi, M. (2012). ZnO Spin-Coating of TiO₂ Photo-Electrodes to Enhance the Efficiency of Associated Dye-Sensitized Solar Cells. *World J. Condens. Matter Phys.* **02**, 192–196.
- Alya, S. A. and Akla, A. A. (2015). Influence of Film Thickness on Optical Absorption and Energy Gap of Thermally Evaporated CdS_{0.1}Se_{0.9} Thin Films. *Chalcogenide Lett.* **12**, 489–496.
- Andreani, L. C., Bozzola, A., Kowalczewski, P., Liscidini, M., and Redorici, L. (2019). Silicon Solar Cells: Toward the Efficiency Limits. *Adv. Phys. X* **4**, 1-24.
- Andualem, A. and Demiss, S. (2018). Review on Dye - Sensitized Solar Cells (DSSCs). *Sci Tech* **2**, 145–150.
- Aoyama, T., Aoki, M., Sumita, I., Yoshino, Y., and Ogura, A. (2017). Characterization of Glass Frit in Conductive Paste for N-Type Crystalline Silicon Solar Cells. *IEEE J. Photovolt.* **7**, 1313–1318.

- Arunachalam, A., Dhanapandian, S., Manoharan, C., and Sivakumar, G. (2015). Physical Properties of Zn Doped TiO₂ Thin Films with Spray Pyrolysis Technique and its Effects in Antibacterial Activity. *Spectrochim. Acta. A. Mol. Biomol. Spectrosc.* **138**, 105–112.
- Asahi, R., Taga, Y., Mannstadt, W., and Freeman, A. J. (2000). Electronic and Optical Properties of Anatase TiO₂. *Phys. Rev.* **61**, 7459–7465.
- Augustyniak, M. M. (2016). Preparation, Characterization and Optimization of Blocking Layers for Improving Efficiency of Dye-Sensitized Solar Cells. A thesis submitted to Cardiff University.
- Ayieko, O. C., O. Aduda, B., K. Jain, P., and R, J. M. (2012). Structural and Optical Characterization of Nitrogen-doped TiO₂ Thin Films Deposited by Spray Pyrolysis on Fluorine Doped Tin Oxide (FTO) Coated Glass Slides. *Int. J. Energy Eng.* **2**, 67–72.
- Bak, Y.-R., Kim, G.-O., Hwang, M.-J., Cho, K.-K., Kim, K.-W., and Ryu, K.-S. (2011). Fabrication and Performance of Nanoporous TiO₂/SnO₂ Electrodes with a Half Hollow Sphere Structure for Dye Sensitized Solar Cells. *J. Sol-Gel Sci. Technol.* **58**, 518–523.
- Barchiesi, D. and Grosjes, T. (2014). Fitting the Optical Constants of Gold, Silver, Chromium, Titanium, and Aluminum in the Visible Bandwidth. *J. Nanophotonics* **8**, 1–16.
- Basu, K., Benetti, D., Zhao, H., Jin, L., Vetrone, F., Vomiero, A., and Rosei, F. (2016). Enhanced Photovoltaic Properties in Dye Sensitized Solar Cells by Surface Treatment Of SnO₂ Photoanodes. *Sci. Rep.* **6**, 1–10.
- Beek, W. J. E. and Janssen, R. A. J. (2004). Spacer Length Dependence of Photoinduced Electron Transfer in Heterosupramolecular Assemblies of TiO₂ Nanoparticles and Terthiophene. *J. Mater. Chem.* **14**, 2795–2800.

Bhattacharyya, S. R., Gayen, R. N., Paul, R., and Pal, A. K. (2009). Determination of Optical Constants of Thin Films from Transmittance Trace. *Thin Solid Films* **517**, 5530–5536.

Biju, K. P. and Jain, M. K. (2008). Effect of Crystallization on Humidity Sensing Properties of Sol–Gel Derived Nanocrystalline TiO₂ Thin Films. *Thin Solid Films* **516**, 2175–2180.

Bisquert, J., Fabregat-Santiago, F., Mora-Seró, I., Garcia-Belmonte, G., and Giménez, S. (2009). Electron Lifetime in Dye-Sensitized Solar Cells: Theory and Interpretation of Measurements. *J. Phys. Chem. C* **113**, 17278–17290.

Bisquert, J. and Mora-Seró, I. (2010). Simulation of Steady-State Characteristics of Dye-Sensitized Solar Cells and the Interpretation of the Diffusion Length. *J. Phys. Chem. Lett.* **1**, 450–456.

Bouabellou, F. H. (2013). Structural, Optical and Electrical Properties of TiO₂ Thin Films Synthesized by Sol–Gel Technique. *IOSR J. Eng.* **3**, 21–28.

Cabestany, J. and Castañer, X. (1983). A Simple Solar Cell Series Resistance Measurement Method. *Rev. Phys. Appl.* **18**, 565–567.

Calogero, G., Calandra, P., Irrera, A., Sinopoli, A., Citro, I., and Di Marco, G. (2011). A New Type of Transparent and Low Cost Counter-Electrode Based on Platinum Nanoparticles for Dye-Sensitized Solar Cells. *Energy Environ. Sci.* **4**, 1838–1844.

Caramori, S., Ronconi, F., Argazzi, R., Carli, S., Boaretto, R., Busatto, E., and Bignozzi, C. A. (2016). Solar Energy Conversion in Photoelectrochemical Systems. In “Applied Photochemistry” (G. Bergamini, S. Silvi, Eds.), Springer International Publishing. **92**, 67–143.

Carella, A., Borbone, F., and Centore, R. (2018). Research Progress on Photosensitizers for DSSC. *Front. Chem.* **6**, 1–24.

Černá, M., Veselý, M., and Dzik, P. (2011). Physical and Chemical Properties of Titanium Dioxide Printed Layers. *Catal. Today* **161**, 97–104.

Chen, S. G., Chappel, S., Diamant, Y., and Zaban, A. (2001). Preparation of Nb₂O₅ Coated TiO₂ Nanoporous Electrodes and their Application in Dye-Sensitized Solar Cells. *Chem. Mater.* **13**, 4629–4634.

Cho, M. H., Seol, H., Yang, H., Yun, P. S., Bae, J. U., Park, K.-S., and Jeong, J. K. (2018). High-Performance Amorphous Indium Gallium Zinc Oxide Thin-Film Transistors Fabricated by Atomic Layer Deposition. *IEEE Electron Device Lett.* **39**, 688–691.

Choi, H., Nahm, C., Kim, J., Moon, J., Nam, S., Jung, D.-R., and Park, B. (2012). The Effect of TiCl₄-Treated TiO₂ Compact Layer on the Performance of Dye-Sensitized Solar Cell. *Curr. Appl. Phys.* **12**, 737–741.

Concina, I. and Vomiero, A. (2015). Metal Oxide Semiconductors for Dye- and Quantum-Dot-Sensitized Solar Cells. *Small* **11**, 1744–1774.

Diebold, U. (2003). The Surface Science of Titanium Dioxide. *Surf. Sci. Rep.* **48**, 53–229.

Eguchi, K., Koga, H., Sekizawa, K., and Sasaki, K. (2000). Nb₂O₅-Based Composite Electrodes for Dye-Sensitized Solar Cells. *J. Ceram. Soc. Jpn.* **108**, 1067–1071.

Eiamchai, P., Chindaudom, P., Pokaipisit, A., and Limsuwan, P. (2009). A Spectroscopic Ellipsometry Study of TiO_2 Thin Films Prepared by Ion-Assisted Electron-Beam Evaporation. *Curr. Appl. Phys.* **9**, 707–712.

El-Amin, A. A. and Solieman, A. (2015). Influence of Heat Treatment on the Optical Properties of Thermal Evaporated SnO_2 Thin Films. *Silicon* **8**, 517–523.

Fraas, L. M. (2014). Low Cost Solar Electric Power. Springer International Publishing Switzerland.

Gan, W. Y., Lam, S. W., Chiang, K., Amal, R., Zhao, H., and Brungs, M. P. (2007). Novel TiO_2 Thin Film with Non-UV Activated Superwetting and Antifogging Behaviors. *J. Mater. Chem.* **17**, 952–954.

Gao, C., Li, X., Lu, B., Chen, L., Wang, Y., Teng, F., Wang, J., Zhang, Z., Pan, X., and Xie, E. (2012). A Facile Method to Prepare SnO_2 Nanotubes for use in Efficient SnO_2 – TiO_2 Core–Shell Dye-Sensitized Solar Cells. *Nanoscale* **4**, 3475–3481.

Garcia-Belmonte, G., Boix, P. P., Bisquert, J., Sessolo, M., and Bolink, H. J. (2010). Simultaneous Determination of Carrier Lifetime and Electron Density-of-States in P3HT:PCBM Organic Solar Cells Under Illumination by Impedance Spectroscopy. *Sol. Energy Mater. Sol. Cells* **94**, 366–375.

Garcia-Belmonte, G., Munar, A., Barea, E. M., Bisquert, J., Ugarte, I., and Pacios, R. (2008). Charge Carrier Mobility and Lifetime of Organic Bulk Heterojunctions Analyzed by Impedance Spectroscopy. *Org. Electron.* **9**, 847–851.

Ghani, F. and Duke, M. (2011). Numerical Determination of Series and Shunt Resistances Using the Lambert W-Function. In “2011 37th IEEE Photovoltaic Specialists Conference (PVSC),” 2861–2865.

Góes, M. S., Joanni, E., Muniz, E. C., Savu, R., Habeck, T. R., Bueno, P. R., and Fabregat-Santiago, F. (2012). Impedance Spectroscopy Analysis of the Effect of TiO₂ Blocking Layers on the Efficiency of Dye Sensitized Solar Cells. *J. Phys. Chem. C* **116**, 12415–12421.

Goh, E. S. M., Chen, T. P., Sun, C. Q., and Liu, Y. C. (2010). Thickness Effect on the Band Gap and Optical Properties of Germanium Thin Films. *J. Appl. Phys.* **107**, 1–5.

Govindasamy, G., Murugasen, P., and Sagadevan, S. (2016). Investigations on the Synthesis, Optical and Electrical Properties of TiO₂ Thin Films by Chemical Bath Deposition (CBD) method. *Mater. Res.* **19**, 413–419.

Green, M. A., Hishikawa, Y., Dunlop, E. D., Levi, D. H., Hohl-Ebinger, J., and Ho-Baillie, A. W. Y. (2018). Solar Cell Efficiency Tables (Version 51). *Prog. Photovolt. Res. Appl.* **26**, 3–12.

Gu, P., Yang, D., Zhu, X., Sun, H., Wangyang, P., Li, J., and Tian, H. (2017). Influence of Electrolyte Proportion on the Performance of Dye-Sensitized Solar Cells. *AIP Adv.* **7**, 1-9.

Han, L., Koide, N., Chiba, Y., and Mitate, T. (2004). Modeling of an equivalent circuit for dye-sensitized solar cells. *Appl. Phys. Lett.* **84**, 2433–2435.

Hao, Q., Fu, X., Song, S., Gibson, D., Li, C., Chu, H., and Shi, Y. (2018). Investigation of TiO₂ Thin Film Deposited by Microwave Plasma Assisted Sputtering and its Application in 3D Glasses. *Coatings* **8**, 270.

Hao, S., Wu, J., Huang, Y., and Lin, J. (2006). Natural Dyes as Photosensitizers for Dye-Sensitized Solar Cell. *Sol. Energy* **80**, 209–214.

Hara, K. and Arakawa, H. (2005). Dye-Sensitized Solar Cells. In “Handbook of Photovoltaic Science and Engineering” (A. Luque, S. Hegedus, Eds.), John Wiley & Sons, Ltd, Chichester, UK. 663–700.

Haug, F.-J. and Ballif, C. (2015). Light Management in Thin Film Silicon Solar Cells. *Energy Environ. Sci.* **8**, 824–837.

Hong, S., Han, A., Lee, E. C., Ko, K.-W., Park, J.-H., Song, H.-J., Han, M.-H., and Han, C.-H. (2015). A Facile and Low-Cost Fabrication of TiO₂ Compact Layer for Efficient Perovskite Solar Cells. *Curr. Appl. Phys.* **15**, 574–579.

Ilican, S., Caglar, M., and Caglar, Y. (2007). Determination of the Thickness and Optical Constants of Transparent Indium-Doped ZnO Thin Films by the Envelope Method. *Mater. Sci.-Pol.* **25**, 709–718.

Ishibashi, S., Higuchi, Y., Ota, Y., and Nakamura, K. (1990). Low Resistivity Indium–Tin Oxide Transparent Conductive Films. *J. Vac. Sci. Technol.* **8**, 1403–1406.

Ito, S., Murakami, T. N., Comte, P., Liska, P., Grätzel, C., Nazeeruddin, M. K., and Grätzel, M. (2008). Fabrication of thin film dye sensitized solar cells with solar to electric power conversion efficiency over 10%. *Thin Solid Films* **516**, 4613–4619.

Jayasinghe, R. C., Lao, Y. F., Perera, A. G. U., Hammar, M., Cao, C. F., and Wu, H. Z. (2012). Plasma Frequency and Dielectric Function Dependence on Doping and Temperature for P-Type Indium Phosphide Epitaxial Films. *J. Phys. Condens. Matter* **24**, 1–9.

Jose, R., Thavasi, V., and Ramakrishna, S. (2009a). Metal Oxides for Dye-Sensitized Solar Cells. *J. Am. Ceram. Soc.* **92**, 289–301.

Jose, R., Thavasi, V., and Ramakrishna, S. (2009b). Metal Oxides for Dye-Sensitized Solar Cells. *J. Am. Ceram. Soc.* **92**, 289–301.

Kalyanasundaram, K. (2010). “Dye-sensitized Solar Cells.” EPFL Press.

Kamran, A. (2014). Spray pyrolysis, Titanium Butoxide, Raman spectroscopy, Photo-catalyst, Anatase, Rutile. *Int. J. Compos. Mater.* **5**, 213–218.

Karsten, F., Emma Norton, David Caffrey, and Igor Shvets (2017). Quantifying the Performance of P-Type Transparent Conducting Oxides by Experimental Methods. *Materials* **10**, 1–14.

Kaunda, C. S., Kimambo, C. Z., and Nielsen, T. K. (2012). Hydropower in the Context of Sustainable Energy Supply: A Review of Technologies and Challenges. *ISRN Renew. Energy* **2012**, 1–15.

Kaur, M. and Singh, H. (2016). A Review: Comparison of Silicon Solar Cells and Thin Film Solar Cells. **3**, 15–23.

Kim, D. H., Atanasov, S. E., Lemaire, P., Lee, K., and Parsons, G. N. (2015). Platinum-Free Cathode for Dye-Sensitized Solar Cells Using Poly(3,4-ethylenedioxythiophene) (PEDOT) Formed via Oxidative Molecular Layer Deposition. *ACS Appl. Mater. Interfaces* **7**, 3866–3870.

Kim, H.-J., Jeon, J.-D., Kim, D. Y., Lee, J.-J., and Kwak, S.-Y. (2012). Improved Performance of Dye-Sensitized Solar Cells with Compact TiO₂ Blocking Layer Prepared using Low-

Temperature Reactive ICP-Assisted DC Magnetron Sputtering. *J. Ind. Eng. Chem.* **18**, 1807–1812.

Kohle, O., Grätzel, M., Meyer, A. F., and Meyer, T. B. (1997). The Photovoltaic Stability of, bis(isothiocyanato)rlutheniurn(II)-bis-2, 2'bipyridine-4, 4'-dicarboxylic Acid and Related Sensitizers. *Adv. Mater.* **9**, 904–906.

Kose, S., Atay, F., Bilgin, V., and Akyuz, I. (2009). In Doped Cdo Films: Electrical, Optical, Structural and Surface Properties. *Int. J. Hydrog. Energy* **34**, 5260–5266.

Krasikov, D. N., Scherbinin, A. V., Knizhnik, A. A., Vasiliev, A. N., Potapkin, B. V., and Sommerer, T. J. (2016). Theoretical Analysis of Non-Radiative Multiphonon Recombination Activity of Intrinsic Defects in CdTe. *J. Appl. Phys.* **119**, 1–10.

Krogmeier, B. (2016). Discriminating Between Different Recombination Mechanisms in Solution Processable Solar Cells. *Master Thesis Submitted to Univ. Duisburg-Ess.*

Lasia, A. (1999). Electrochemical Impedance Spectroscopy and its Applications. *B E Conway J Bockris RE White Edts Kluwer Acad. Publ. N. Y.* **32**, 143–248.

Leever, B. J., Bailey, C. A., Marks, T. J., Hersam, M. C., and Durstock, M. F. (2012). In Situ Characterization of Lifetime and Morphology in Operating Bulk Heterojunction Organic Photovoltaic Devices by Impedance Spectroscopy. *Adv. Energy Mater.* **2**, 120–128.

León, A., Reuquen, P., Garín, C., Segura, R., Vargas, P., Zapata, P., and Orihuela, P. (2017). FTIR and Raman Characterization of TiO₂ Nanoparticles Coated with Polyethylene Glycol as Carrier for 2-Methoxyestradiol. *Appl. Sci.* **7**, 1-9.

- Look, D. C., Reynolds, D. C., Sizelove, J. R., Jones, R. L., Litton, C. W., Cantwell, G., and Harsch, W. C. (1998). Electrical Properties of Bulk ZnO. *Solid State Commun.* **105**, 399–401.
- Maghanga, C. M. and Mwamburi, M. M. (2018). Contribution of Drude and Brendel Model Terms to the Dielectric Function; A case of TiO₂:Nb Thin Films. *J. Model. Simul. Mater.* **1**, 3–7.
- Malati, M. A. and Wong, W. K. (1984). Doping TiO₂ for Solar Energy Applications. *Surf. Technol.* **22**, 305–322.
- Marinado, T., Nonomura, K., Nissfolk, J., Karlsson, Martin. K., Hagberg, D. P., Sun, L., Mori, S., and Hagfeldt, A. (2010). How the Nature of Triphenylamine-Polyene Dyes in Dye-Sensitized Solar Cells Affects the Open-Circuit Voltage and Electron Lifetimes. *Langmuir* **26**, 2592–2598.
- Mayer, A. C., Scully, S. R., Hardin, B. E., Rowell, M. W., and McGehee, M. D. (2007). Polymer-Based Solar Cells. *Mater. Today* **10**, 28–33.
- McIntosh, K. R. and Honsberg, C. B. (2000). The Influence of Edge Recombination on a Solar Cell's I-V Curve. *16th Eur. Photovolt. Sol. Energy Conf.*, 1–4.
- Mebrahtu, C., M. Tadesse, A., Goro, G., and Yohannes, T. (2017). Natural Pigment Sensitized Solar Cells Based on ZnO-TiO₂-Fe₂O₃ Nanocomposite in Quasi-Solid State Electrolyte System. *Bull. Chem. Soc. Ethiop.* **31**, 263–279.
- Mendoza, L. J. H., Arboleda, D. M., Schinca, D. C., and Scaffardi, L. B. (2014). Determination of Plasma Frequency, Damping Constant, and Size Distribution from the Complex Dielectric Function of Noble Metal Nanoparticles. *J. Appl. Phys.* **116**, 1–8.

Meng, L., Ren, T., and Li, C. (2010). The Control of the Diameter of the Nanorods Prepared by Dc Reactive Magnetron Sputtering and the Applications for DSSC. *Appl. Surf. Sci.* **256**, 3676–3682.

Muaz, A. K. M., Hashim, U., Arshad, M. K. Md., Ruslinda, A. R., Ayub, R. M., Gopinath, S. C. B., Voon, C. H., Liu, W.-W., and Foo, K. L. (2016). Study of Nanoparticles TiO₂ Thin Films on P-Type Silicon Substrate using Different Alcoholic Solvents. American Institute of Physics. **1733**, 1–5.

Murakami, T. N., Ito, S., Wang, Q., Nazeeruddin, Md. K., Bessho, T., Cesar, I., Liska, P., Humphry-Baker, R., Comte, P., Péchy, P., and Grätzel, M. (2006). Highly Efficient Dye-Sensitized Solar Cells Based on Carbon Black Counter Electrodes. *J. Electrochem. Soc.* **153**, 2255-2261.

Murugesan, M., Arjunraj, D., Mayandi, J., Venkatachalapathy, V., and Pearce, J. M. (2018). Properties Of Al-Doped Zinc Oxide And In-Doped Zinc Oxide Bilayer Transparent Conducting Oxides For Solar Cell Applications. *Mater. Lett.* **222**, 50–53.

Muthukumar, A., Rey, G., Giusti, G., Consonni, V., Appert, E., Roussel, H., Dakshnamoorthy, A., and Bellet, D. (2013). Fluorine Doped Tin Oxide (FTO) Thin Film as Transparent Conductive Oxide (TCO) for Photovoltaic Applications. American Institute of Physics. **1512**, 710–711.

Myoung, J.-M., Yoon, W.-H., Lee, D.-H., Yun, I., Bae, S.-H., and Lee, S.-Y. (2002). Effects of Thickness Variation on Properties of ZnO Thin Films Grown by Pulsed Laser Deposition. *Jpn. J. Appl. Phys.* **41**, 28–31.

Nandani, Supriyanto, A., Ramelan, A. H., and Nurosyid, F. (2018). Effect of Annealing Temperature on Optical Properties of TiO₂ 18 NR-T Type Thin Film. *J. Phys. Conf. Ser.* **1011**, 1–6.

Napi, M. L. M., Maarof, M. F., Soon, C. F., Nayan, N., Seng, N. K., Ahmad, M. K., Suriani, A. B., and Mohamed, A. (2016). Fabrication of Fluorine Doped Tin Oxide (FTO) Thin Films using Spray Pyrolysis Deposition Method for Transparent Conducting Oxide. *ARPN J. Eng. Appl. Sci.* **11**, 8800–8804.

Nazeeruddin, M. K., Péchy, P., Renouard, T., Zakeeruddin, S. M., Humphry-Baker, R., Comte, P., Liska, P., Cevey, L., Costa, E., Shklover, V., Spiccia, L., Deacon, G. B., Bignozzi, C. A., and Grätzel, M. (2001). Engineering of Efficient Panchromatic Sensitizers for Nanocrystalline TiO₂ - Based Solar Cells. *J. Am. Chem. Soc.* **123**, 1613–1624.

Nguu, J. N., Aduda, B. O., Nyongesa, F. W., and Musembi, R. J. (2014). Electrophoretic Deposition of TiO₂/Nb₂O₅ Composite Electrode Thin Films for Photovoltaic Application. *J. Energy Power Eng.* **8**, 757–764.

Nicholas, M., Munji, M., Justus, S., Eric, M., and Raphael, N. (2018). Effect of TiO₂ Compact Layer on DSSC Performance. *Path Sci.* **4**, 5001–5008.

Nikolay, T., Larina, L., Shevaleevskiy, O., and Ahn, B. T. (2011). Electronic Structure Study of Lightly Nb-Doped TiO₂ Electrode for Dye-Sensitized Solar Cells. *Energy Environ. Sci.* **4**, 1480–1486.

Ohsaka, T., Izumi, F., and Fujiki, Y. (1978). Raman Spectrum of Anatase, TiO₂. *J. Raman Spectrosc.* **7**, 321–324.

Oommen, R., Rajalakshmi, P. U., and Sudha, S. (2013). Optical Characteristics of TiO₂ Thin Films Sensitized with the Natural Dye of Clitoria Ternatea. *Int. J. Appl. Phys. Math.* **2**, 439–441.

O'Regan, B. C., Scully, S., Mayer, A. C., Palomares, E., and Durrant, J. (2005). The Effect of Al₂O₃ Barrier Layers in TiO₂ /Dye/CuSCN Photovoltaic Cells Explored by Recombination and DOS Characterization Using Transient Photovoltage Measurements. *J. Phys. Chem. B* **109**, 4616–4623.

O'Regan, B. and Grätzel, M. (1991). A Low-Cost, High-Efficiency Solar Cell Based on Dye-Sensitized Colloidal TiO₂ Films. *Nature* **353**, 737–740.

Ortega, A., Rosales, J. J., Martínez, L., and Carreño, C. A. (2018). Fractional Optical Properties of Drude Model. *Optik* **161**, 244–249.

Pal, U., Morales-Flores, N., and Rubio-Rosas, E. (2017). Effect of Nb Doping on Morphology, Optical and Magnetic Behaviors of Ultrasonically Grown ZnO Nanostructures. *Mater. Sci. Res. India* **14**, 79–88.

Park, N., Sun, K., Sun, Z., Jing, Y., and Wang, D. (2013). High Efficiency NiO/ZnO Heterojunction UV Photodiode by Sol–Gel Processing. *J. Mater. Chem. C* **1**, 7333–7338.

Peng, B., Jungmann, G., Jäger, C., Haarer, D., Schmidt, H.-W., and Thelakkat, M. (2004). Systematic Investigation of the Role of Compact TiO₂ Layer in Solid State Dye-Sensitized TiO₂ Solar Cells. *Coord. Chem. Rev.* **248**, 1479–1489.

Pulker, H. K. (1979). Characterization of Optical Thin Films. *Appl. Opt.* **18**, 1969–1977.

- Qin, Y. and Peng, Q. (2012). Ruthenium Sensitizers and their Applications in Dye-Sensitized Solar Cells. *Int. J. Photoenergy* **2012**, 1–21.
- Rabeh, M. B., Khedmi, N., Fodha, M. A., and Kanzari, M. (2014). The Effect of Thickness on Optical Band Gap and N-type Conductivity of CuInS₂ Thin Films Annealed in Air Atmosphere. *Energy Procedia* **44**, 52–60.
- Raut, N. C., Mathews, T., Sundari, S. T., Sairam, T. N., Dash, S., and Tyagi, A. K. (2009). Structural and Morphological Characterization of TiO₂ Thin Films Synthesized by Spray Pyrolysis Technique. *J. Nanosci. Nanotechnol.* **9**, 5298–5302.
- Rawal, N., Vaishaly, A. G., Sharma, H., and Mathew, B. B. (2015). Dye Sensitized Solar Cells: The Emerging Technology. *Energy Power Eng. Sci.* **2**, 46–52.
- Ren, Y., Li, Y., Chen, S., Liu, J., Zhang, J., and Wang, P. (2016). Improving the Performance of Dye-Sensitized Solar Cells with Electron-Donor and Electron-Acceptor Characteristic of Planar Electronic Skeletons. *Energy Environ. Sci.* **9**, 1390–1399.
- Roh, S.-J., Mane, R. S., Min, S.-K., Lee, W.-J., Lokhande, C. D., and Han, S.-H. (2006). Achievement of 4.51% Conversion Efficiency Using ZnO Recombination Barrier Layer in TiO₂ Based Dye-Sensitized Solar Cells. *Appl. Phys. Lett.* **89**, 1–4.
- Rouhi, J., Mamat, M. H., Ooi, C. H. R., Mahmud, S., and Mahmood, M. R. (2015). High-Performance Dye-Sensitized Solar Cells Based on Morphology-Controllable Synthesis of ZnO–ZnS Heterostructure Nanocone Photoanodes. *Plos One* **10**, 1–14.
- Roy-Mayhew, J. D., Bozym, D. J., Punckt, C., and Aksay, I. A. (2010). Functionalized Graphene as a Catalytic Counter Electrode in Dye-Sensitized Solar Cells. *ACS Nano* **4**, 6203–6211.

- Saleh, M. H., Jafar, M. M. A.-G., Bulos, B. N., and Al-Daraghme, T. M. F. (2014). Determination of Optical Properties of Undoped Amorphous Selenium (A-Se) Films by Dielectric Modeling of their Normal-Incidence Transmittance Spectra. *Appl. Phys. Res.* **6**, 1–26.
- Sarker, S., Ahammad, A. J. S., Seo, H. W., and Kim, D. M. (2014). Electrochemical Impedance Spectra of Dye-Sensitized Solar Cells: Fundamentals and Spreadsheet Calculation. *Int. J. Photoenergy* **2014**, 1–17.
- Shah, S. A. A., Sayyad, M. H., Wahab, F., Khan, K. A., Munawar, M. A., Elbohy, H., and Qiao, Q. (2016). Synthesis, Modeling and Photovoltaic Properties of a Benzothiadiazole Based Molecule for Dye-Sensitized Solar Cells. *J. Mater. Sci. Mater. Electron.* **27**, 4501–4507.
- Sharma, S., Shrivastava, S., Kumar, S., Bhatt, K., and Tripathi, C. C. (2018). Alternative Transparent Conducting Electrode Materials for Flexible Optoelectronic Devices. *Opto-Electron. Rev.* **26**, 223–235.
- Shiratori, S. and Muraguchi, K. (2012). Nanoscale Roughness Control of Electron Transport Layer in Organic Solar Cells Fabricated by Sol–Gel Method. *Jpn. J. Appl. Phys.* **51**, 1-6.
- Siddique, H. A. B., Xu, P., and De Doncker, R. W. (2013). Parameter Extraction Algorithm for One-Diode Model of PV Panels Based on Datasheet Values. In “2013 International Conference on Clean Electrical Power (ICCEP),” IEEE, Alghero, Italy. 7–13.
- Singh, P. and Ravindra, N. M. (2012). Analysis of Series and Shunt Resistance in Silicon Solar Cells Using Single and Double Exponential Models. *Emerg. Mater. Res.* **1**, 33–38.

- Solieman, A. and Abu-sehly, A. A. (2011). Determination of the Optical Constants of Amorphous As₁₀₀-X Films Using Effective-Medium Approximation and OJL Model. *Mater. Chem. Phys.* **129**, 1000–1005.
- Solieman, A. and Abu-Sehly, A. A. (2010). Modelling of Optical Properties of Amorphous Selenium Thin Films. *Phys. B Condens. Matter* **405**, 1101–1107.
- Solieman, A. S., Hafiz, M. M., Abu-Sehly, A. A., and Alfaqeer, A. A. (2014). Dependence of Optical Properties on the Thickness of Amorphous Ge₃₀Se₇₀ Thin Films. *J. Taibah Univ. Sci.* **8**, 282–288.
- Song, X., Ji, X., Li, M., Lin, W., Luo, X., and Zhang, H. (2014). A Review on Development Prospect of CZTS Based Thin Film Solar Cells. *Int. J. Photoenergy* **2014**, 1–11.
- Sönmezoğlu, S., Çankaya, G., and Serin, N. (2012). Influence of Annealing Temperature on Structural, Morphological and Optical Properties of Nanostructured TiO₂ Thin Films. *Mater. Technol.* **27**, 251–256.
- Su'ait, M. S., Rahman, M. Y. A., and Ahmad, A. (2015). Review on Polymer Electrolyte in Dye-Sensitized Solar Cells (DSSCs). *Sol. Energy* **115**, 452–470.
- Supasai, T., Henjongchom, N., Tang, I.-M., Deng, F., and Rujisamphan, N. (2016). Compact Nanostructured TiO₂ Deposited by Aerosol Spray Pyrolysis for the Hole-Blocking Layer in A CH₃NH₃PbI₃ Perovskite Solar Cell. *Sol. Energy* **136**, 515–524.
- Swinehart, D. F. (1962). The Beer-Lambert Law. *J. Chem. Educ.* **39**, 333–335.

- Ting, C.-C., Chen, S.-Y., and Liu, D.-M. (2000). Structural Evolution and Optical Properties of TiO₂ Thin Films Prepared by Thermal Oxidation of Sputtered Ti Films. *J. Appl. Phys.* **88**, 4628–4633.
- Todinova, A., Idígoras, J., Salado, M., Kazim, S., and Anta, J. A. (2015). Universal Features of Electron Dynamics in Solar Cells with TiO₂ Contact: From Dye Solar Cells to Perovskite Solar Cells. *J. Phys. Chem. Lett.* **6**, 3923–3930.
- Tributsch, H. (1971). Reaction of Excited Chlorophyll Molecules at Electrodes and in Photosynthesis. *Photochem. Photobiol.* **16**, 261–269.
- Tseng, L.-C., Kuo, M., and Lee, R.-H. (2016). An Imidazolium Iodide-Containing Hyperbranched Polymer Ionic Liquid That Improves the Performance of Dye-Sensitized Solar Cells. *J. Polym. Res.* **23**, 157.
- Tverberg, G. E. (2012). Oil Supply Limits and the Continuing Financial Crisis. *Energy* **37**, 27–34.
- Waita, S. M., Aduda, B. O., Mwabora, J. M., Niklasson, G. A., Granqvist, C. G., and Boschloo, G. (2009). Electrochemical Characterization of TiO₂ Blocking Layers Prepared by Reactive DC Magnetron Sputtering. *J. Electroanal. Chem.* **637**, 79–83.
- Wang, D. H., Kyaw, A. K. K., Gupta, V., Bazan, G. C., and Heeger, A. J. (2013). Enhanced Efficiency Parameters of Solution-Processable Small-Molecule Solar Cells Depending on ITO Sheet Resistance. *Adv. Energy Mater.* **3**, 1161–1165.

Wang, J., Jin, E., Park, J.-Y., Wang, W., Zhao, X., and Gu, H.-B. (2012). Increases in Solar Conversion Efficiencies of the ZrO₂ Nanofiber-Doped TiO₂ Photoelectrode for Dye-Sensitized Solar Cells. *Nanoscale Res. Lett.* **7**, 1–4.

Wang, Q., Ito, S., Grätzel, M., Fabregat-Santiago, F., Mora-Seró, I., Bisquert, J., Bessho, T., and Imai, H. (2006). Characteristics of High Efficiency Dye-Sensitized Solar Cells. *J. Phys. Chem. B* **110**, 25210–25221.

Wang, Z.-S., Cui, Y., Dan-oh, Y., Kasada, C., Shinpo, A., and Hara, K. (2008). Molecular Design of Coumarin Dyes for Stable and Efficient Organic Dye-Sensitized Solar Cells. *J. Phys. Chem. C* **112**, 17011–17017.

Wei, M., Qi, Z., Ichihara, M., and Zhou, H. (2008). Synthesis of Single-Crystal Niobium Pentoxide Nanobelts. *Acta Mater.* **56**, 2488–2494.

Widiyandari, H., Purwanto, A., Diharjo, K., Suyitno, and Hidayanto, E. (2013). Fluorine Doped-Tin Oxide Prepared Using Spray Method for Dye Sensitized Solar Cell Application. *In* “Padjadjaran International Physics Symposium 2013 (Pips-2013),” 147–149.

Williamson, G. K. and Smallman, R. E. (1956). Dislocation Densities in Some Annealed and Cold-Worked Metals from Measurements on the X-Ray Debye-Scherrer Spectrum. *Philos. Mag.* **1**, 34–46.

Wongcharee, K., Meeyoo, V., and Chavadej, S. (2007). Dye-Sensitized Solar Cell Using Natural Dyes Extracted from Rosella and Blue Pea Flowers. *Sol. Energy Mater. Sol. Cells* **91**, 566–571.

Wu, J., Lan, Z., Lin, J., Huang, M., Huang, Y., Fan, L., Luo, G., Lin, Y., Xie, Y., and Wei, Y. (2017b). Counter Electrodes in Dye-Sensitized Solar Cells. *Chem. Soc. Rev.* **46**, 5975–6023.

Wu, S., Han, H., Tai, Q., Zhang, J., Xu, S., Zhou, C., Yang, Y., Hu, H., Chen, B., Sebo, B., and Zhao, X.-Z. (2008). Enhancement in Dye-Sensitized Solar Cells Based on MgO-Coated TiO₂ Electrodes by Reactive DC Magnetron Sputtering. *Nanotechnology* **19**, 1–6.

Wu, W.-Y., Hsu, C.-F., Wu, M.-J., Chen, C.-N., and Huang, J.-J. (2017a). Ag–TiO₂ Composite Photoelectrode for Dye-Sensitized Solar Cell. *Appl. Phys. A* **123**, 1–8.

Xia, J., Masaki, N., Jiang, K., and Yanagida, S. (2007). Sputtered Nb₂O₅ as an Effective Blocking Layer at Conducting Glass And TiO₂ Interfaces in Ionic Liquid-Based Dye-Sensitized Solar Cells. *Chem Commun* **14**, 138–140.

Xia, J., Masaki, N., Jiang, K., and Yanagida, S. (2006). Deposition of a Thin Film of TiO_x from a Titanium Metal Target as Novel Blocking Layers at Conducting Glass/TiO₂ Interfaces in Ionic Liquid Mesoscopic TiO₂ Dye-Sensitized Solar Cells[†]. *J. Phys. Chem. B* **110**, 25222–25228.

Yang, R.-Y., Chen, H.-Y., and Lai, F.-D. (2012). Performance Degradation of Dye-Sensitized Solar Cells Induced by Electrolytes. *Adv. Mater. Sci. Eng.* **2012**, 1–4.

Yang, Z., Chen, T., He, R., Li, H., Lin, H., Li, L., Zou, G., Jia, Q., and Peng, H. (2013). A Novel Carbon Nanotube/Polymer Composite Film for Counter Electrodes of Dye-Sensitized Solar Cells. *Polym. Chem.* **4**, 1680–1684.

Yodyingyong, S., Zhang, Q., Park, K., Dandeneau, C. S., Zhou, X., Triampo, D., and Cao, G. (2010). ZnO Nanoparticles and Nanowire Array Hybrid Photoanodes for Dye-Sensitized Solar Cells. *Appl. Phys. Lett.* **96**, 1–3.

Yoo, B., Kim, K.-J., Bang, S.-Y., Ko, M. J., Kim, K., and Park, N.-G. (2010). Chemically Deposited Blocking Layers on FTO Substrates: Effect of Precursor Concentration on Photovoltaic Performance of Dye-Sensitized Solar Cells. *J. Electroanal. Chem.* **638**, 161–166.

Zaidi, B., Saouane, I., and Shekhar, C. (2018). Simulation of Single-Diode Equivalent Model of Polycrystalline Silicon Solar Cells. **7**, 8–10.

Zhang, Z., Zakeeruddin, S. M., O'Regan, B. C., Humphry-Baker, R., and Grätzel, M. (2005). Influence of 4-Guanidinobutyric Acid as Coadsorbent in Reducing Recombination in Dye-Sensitized Solar Cells. *J. Phys. Chem. B* **109**, 21818–21824.

Zhao, X., Zhao, Q., Yu, J., and Liu, B. (2008). Development of multifunctional photoactive self-cleaning glasses. *J. Non-Cryst. Solids* **354**, 1424–1430.

Zheng, X., Bai, Y., Xiao, S., Meng, X., Zhang, T., and Yang, S. (2017). Strategies for Improving Efficiency and Stability of Perovskite Solar Cells. *MRS Adv.* **2**, 3051–3060.

Dellis, J.-L. (2018). ZfitGUI - File Exchange - MATLAB Central. *In*

“<https://ww2.mathworks.cn/matlabcentral/fileexchange/69811>.”

International Energy Outlook (2017). U.S Energy Information Administration. [https://www.eia.gov/outlooks/archive/ieo17/pdf/0484\(2017\).pdf](https://www.eia.gov/outlooks/archive/ieo17/pdf/0484(2017).pdf)

National Renewable Energy Laboratory (2018). Photovoltaic Efficiency Chart.20181221.Pdf. <https://www.nrel.gov/pv/assets/pdfs/pv-efficiency-chart.20181221.pdf>

Renewable Energy Policy Network, for the 21st century (2018). Renewable 2018 Global Status Report. http://www.ren21.net/wp-content/uploads/2018/06/17-8652_GSR2018_FullReport_web_final_.pdf

Theiss. M (2000). W. Theiss Hardware and software.

In https://wtheiss.com/wordpress/?page_id=926

https://commons.wikimedia.org/wiki/File:Solar_spectrum_ita.svg, 2008